

Applications of Satellite Geodesy in Environmental and Climate Change

by

Qian Yang

A dissertation submitted in partial fulfillment
of the requirements for the degree of
Doctor of Philosophy
School of Geosciences
College of Arts and Sciences
University of South Florida

Major Professor: Timothy H. Dixon, Ph.D.
Rocco Malservisi, Ph.D.
Don Chambers, Ph.D.
Ping Wang, Ph.D.

Date of Approval:
March 8, 2016

Keywords: Global Positioning System, Gravity Recovery and Climate Experiment,
Interferometric Synthetic Aperture Radar, Greenland ice mass loss, Labrador Sea,
AMOC, carbon sequestration

Copyright © 2016, Qian Yang

Acknowledgements

This dissertation would not have been possible without the help of so many individuals. First and foremost, I cannot thank my advisor, Timothy H. Dixon, enough for guiding and supporting me over the years. I'm grateful to have such an inspiring and encouraging advisor and I truly admire his enthusiasm for sciences. I would like to thank my committee. To Rocco Malservisi, thank you for helping me with GPS processing and numerical modeling. To Don Chambers, thank you for your vital contribution to Chapter Four. To Ping Wang, thank you for your support throughout the stages of this dissertation.

Thanks to my scientific collaborators Shimon Wdwinski, Paul G. Myers, Jennifer Bonin, M.R. van den Broeke, Weon Shik Han, Wenliang Zhao, Falk Amelung who contributed greatly to this dissertation. To Denis Voydenko, thank you for helping me to solve many technical issues. To Fanghui Deng, thank you for answering my questions on the InSAR technique. To Laura Connor, thank you for maintaining the computer systems at the geodesy lab. To every member in the geodesy lab, thank you for creating such a positive work environment.

I would like to thank my friends. To Amanda Piggot, thank you for helping me to improve my English and driving me to school the first semester when I was in the US. To Meng Wang and Wen Zhao, thank you for having me in your home when I visited Tampa, and I really enjoy the time staying with you two, my loving sisters.

Last, but certainty not least, I would like to thank my families. To my parents and my grandma, thank you for your endless love and support. To my beloved husband Peng Li, thank you for being so loving and making me complete.

Table of Contents

List of Tables	iv
List of Figures	v
Abstract	viii
1 Introduction	1
1.1 Overview	1
1.2 References	4
2 Technical Background	9
2.1 Introduction	9
2.2 Global Positioning System	11
2.2.1 Structure	11
2.2.2 GPS signal	12
2.2.3 GPS basic observations	12
2.2.4 GPS error sources	13
2.3 Interferometric Synthetic Aperture Radar	15
2.3.1 Basic concept	16
2.3.2 Monitoring surface deformation	17
2.4 Gravity Recovery and Climate Experiment	19
2.4.1 Basic concept	19
2.4.2 Data Products	20
2.4.3 Measuring the Earth's surface mass change	21
2.5 References	23
3 Annual Variation of Coastal Uplift in Greenland as an Indicator of Variable and Accelerating Ice Mass Loss	37
3.1 Abstract	37
3.2 Introduction	37
3.3 Methods	39
3.3.1 GPS Data and Processing	39
3.3.2 Seasonal Uplift Analysis	40
3.3.3 Surface Air Temperature Data and Analysis	41
3.3.4 SMB	42
3.3.5 Sub-surface Ocean Temperature Data and Analysis	42
3.4 Results	43
3.4.1 Seasonal Uplift/Subsidence Pattern	43
3.4.2 Air Temperature Analysis	45
3.4.3 Comparison to SMB	45

3.4.4	Sub-surface Ocean Temperature Analysis	46
3.4.5	Correlation Analysis	46
3.4.5.1	Uplift and Atmospheric Factors	47
3.4.5.2	Uplift and Ocean Warming	47
3.4.6	Uplift Acceleration	48
3.4.7	Comparison to GRACE	49
3.5	Discussion	50
3.6	Conclusions	53
3.7	Acknowledgements	54
3.8	References	55
4	Recent increases in Arctic freshwater flux affects Labrador Sea convection and Atlantic overturning circulation	82
4.1	Abstract	82
4.2	Introduction	82
4.3	Results	84
4.3.1	Recent accelerated melting of the Greenland ice sheet	84
4.3.2	Irminger Water heat and salt fluxes	84
4.3.3	Estimates of freshwater flux into the Labrador Sea	85
4.3.4	Impact of increased freshwater flux on deep water formation	89
4.4	Discussion	90
4.5	Methods	92
4.5.1	GRACE data	92
4.5.2	Irminger Water heat and salt flux analysis	93
4.5.3	Freshwater flux	94
4.6	Acknowledgements	95
4.7	References	96
5	InSAR Monitoring of Ground Deformation Due to CO ₂ injection at an Enhanced Oil Recovery Site, West Texas	109
5.1	Abstract	109
5.2	Introduction	109
5.3	Study area description	111
5.4	Observed ground deformation	112
5.5	Simulation	113
5.5.1	Analytical solution for ground displacement	113
5.5.2	Input parameters of the analytical simulations	116
5.5.3	Injection and production data during 2004 - 2011	117
5.6	Simulation results	118
5.7	Discussion	120
5.8	Conclusions	121
5.9	Acknowledgements	122
5.10	References	122
6	Conclusions and Future Work	141
6.1	Conclusions	141
6.2	Future Work	142
6.3	References	143

Appendices	145
Appendix A: Supplementary information for Chapter 3	146
Appendix B: Supplementary information for Chapter 4	149
Appendix C: Copyright permission	157
Appendix D: References	164

List of Tables

Table 2.1	GPS satellite signals (bps = bits per second) (Seeber, 2003)	29
Table 3.1	Parameters describing seasonal uplift and atmospheric/oceanic condition at KELY, KULU, QAQ1 and THU3.	62
Table 3.2	Recent uplift history and glacier proximity for all GPS sites considered in this study.	63
Table 3.3	GPS uplift data fit to a model of constant acceleration.	64
Table 5.1	Reservoir homogeneous properties used for pressure change calculation.	126
Table 5.2	Fluid properties at depth (16MPa,41.5 °C).	127
Table 5.3	Highest pressure buildup and best-fit Young's modulus at three levels of porosity and permeability.	128
Table A1	Comparison of seasonal uplift patterns parameters estimated from fitting GPS vertical time series with and without atmospheric loading correction to a cubic spline model.	169
Table A2	List of meteorological stations	170
Table A3	Five parameters of seasonal uplift patterns estimated from fitting GPS vertical data to a cubic spline model and parameters describing both atmospheric and oceanic condition at each GPS site.	171

List of Figures

Figure 2.1	Basic relations for satellite observations.	30
Figure 2.2	Carrier phase ranging.	31
Figure 2.3	GPS satellite constellation.	32
Figure 2.4	Composition of the signals from GPS satellites.	33
Figure 2.5	Acquisition geometry of repeat-track interferometry.	34
Figure 2.6	Basic mission concept of GRACE.	35
Figure 2.7	GRACE-derived maps of monthly anomaly of water storage.	36
Figure 3.1	Map of Greenland showing location of GPS sites, meteorological stations, and other data used in this study.	65
Figure 3.2	Hypothetical 2 year time series showing four parameters (start time, end time, duration, and uplift) defined for a melt season.	66
Figure 3.3	Annual variations of the five parameters defining seasonal uplift calculated for the four sites with longest observation record (red circles in Figure 3.1).	67
Figure 3.4	Uplift versus duration for the four sites with longest observation record.	68
Figure 3.5	Seasonal uplift patterns for 2008–2010.	69
Figure 3.6	(a) AMSAT (Annual mean surface air temperature). (b) CAPDD (Cumulative annual positive degree days) for the four GPS stations with longest observation record.	70
Figure 3.7	Difference of Surface Mass Balance (SMB model from RACMO2) in summertime (June to August) between 2010 and 20XX (XX=00–09) for the Greenland region.	71
Figure 3.8	Difference of AMSSWT (Annual mean, sub-surface water temperature, depth range 5 m – 447 m) between 2010 and 20XX (XX = 00–09) for the Greenland region.	72

Figure 3.9	AMSSWT (Figure 3.8) for “voxels” (model volume elements) nearest a given GPS station.	73
Figure 3.10	Uplift duration versus CAPDD (Figure 3.6).	74
Figure 3.11	Spatial variation of seasonal uplift for four stations with longest time span related to (a) AMSAT (Figure 3.6); (b) CAPDD (Figure 3.6); and (c) AMSSWT (Figure 3.8).	75
Figure 3.12	Comparison between seasonal uplift patterns and atmospheric parameters (AMSAT and CAPDD, Figure 3.6) as well as the ocean temperature parameter (AMSSWT, Figure 3.8) for 2008–2010.	77
Figure 3.13	Temporal variation of seasonal uplift for all stations for 2008–2010 as a function of AMSAT (Figure 3.6), CAPDD (Figure 3.6), and AMSSWT(Figure 3.8).	78
Figure 3.14	Spatial variation of uplift accelerations as a function of (a) AMSAT (Figure 3.6), (b) CAPDD (Figure 3.6), and (c) AMSSWT (Figure 3.8) of 2010.	79
Figure 3.15	Site map of relative difference between uplift in 2010 and uplift in 2008 and 2009.	80
Figure 3.16	Relation between ocean currents, coastal uplift, and ice mass balance of coastal Greenland.	81
Figure 4.1	Study region showing oceanographic sections and major currents around Greenland.	104
Figure 4.2	Mass change of Greenland estimated from GRACE for the period 2002 - 2014.	105
Figure 4.3	Heat and salt fluxes of Irminger Water for the period 1949 – 2013.	106
Figure 4.4	Freshwater flux from Greenland and CAA and Arctic sea ice for the period 1979 – 2013.	107
Figure 4.5	Thickness of LSW and total freshwater flux and salt flux of Irminger Water.	108
Figure 5.1	(a) Total LOS (line of sight) displacement from from January. 08, 2007 to March. 06, 2011. (b) A SAR intensity image of the study area.	130
Figure 5.2	Injection and production history of the study site.	131
Figure 5.3	DEM of our study area.	132

Figure 5.4	(a) Comparison between Line of Sight (LOS) displacement at Snyder (red star marked in Figure 5.1) and cumulative volumes of stored (injection minus production) CO ₂ and water in the field from January 2007 to March 2011. (b) The total volumes of injected/produced/stored CO ₂ , water, oil and HC gas in the field from January 2007 – March 2011.	133
Figure 5.5	Map of study area, showing total LOS displacement from January 08, 2007 to March. 06, 2011, (a) wells injecting CO ₂ (green circle) and water (blue circle), and (b) well producing CO ₂ , water, Oil and HC gas (red triangle).	134
Figure 5.6	Location of virtual wells for each type fluid and the average monthly injection/production rate for each virtual well.	135
Figure 5.7	Calculated pressure change due to fluid injection and production at three levels of porosity and permeability.	136
Figure 5.8	Calculated pressure change due to all injection and production activities at three levels of porosity and permeability.	137
Figure 5.9	Goodness of fit versus Young's modulus at three levels of pressure change conditions.	138
Figure 5.10	Simulated LOS displacement at three levels of pressure change conditions versus InSAR observation along the profile shown in Figure 5.1.	139
Figure 5.11	Comparison between simulated LOS displacements and InSAR observation for the entire study area.	140
Figure A1	GPS time series from site SENU before (pink) and after (black) atmospheric pressure loading correction.	178
Figure A2	Example GPS time series for site SENU, de-trended and fit with annual model shown in Figure 3.2.	179
Figure A3	Snow depth recorded at a meteorological station (WMO-ID 04272, Table A2) in southern Greenland coastal area.	180
Figure A4	Histogram showing statistical result for five seasonal uplift variables at GPS station SENU.	181
Figure A5	Time series of GPS vertical component position.	183
Figure A6	Time series of GPS vertical component position after removing long-term trend by low pass filter.	185
Figure A7	Time series of surface air temperature at meteorological stations near 4 GPS site.	186

Figure A8	Simplified sketch illustrating 3-D structure of the Labrador Sea and major currents and water masses.	187
Figure A9	Comparison of Irminger Water heat flux and North Atlantic SST anomaly over the period 1949 – 2013	188
Figure A10	Freshwater flux from Greenland estimated from mass balance and accumulation. (a) Greenland mass balance.	189
Figure A11	Comparison between estimates of freshwater flux from Greenland.	190
Figure A12	Three estimates of the annual minimum Arctic sea ice volume time series.	191
Figure A13	Long term melting rate of Arctic sea ice from three data sets.	192
Figure A14	Similar to Figure 4.5 except salt flux of Irminger Water is expressed in terms of freshwater flux.	193
Figure A15	Similar to Figure 4.5 except grey solid line represents the mass of Labrador Sea Water.	194
Figure A16	Seasonal variation of freshwater flux from Greenland and the Canadian Arctic Archipelago.	195
Figure A17	Predefined regions used in this paper to localize the GRACE mass change signal.	196
Figure A18	Freshwater flux from Greenland and its two components.	197
Figure A19	Freshwater flux from the Canadian Arctic Archipelago and its two components.	198

Abstract

Space geodesy plays an important role in earth observation. This dissertation presents three applications of satellite geodesy in environmental and climate change. Three satellite geodesy techniques are used: high-precision Global Positioning System (GPS), the Gravity Recovery and Climate Experiment (GRACE) and Interferometric Synthetic Aperture Radar (InSAR). In the first study, I use coastal uplift observed by GPS to study the annual changes in mass loss of the Greenland ice sheet. The data show both spatial and temporal variations of coastal ice mass loss and suggest that a combination of warm atmospheric and oceanic condition drove these variations. In the second study, I use GRACE monthly gravity change estimates to constrain recent freshwater flux from Greenland. The data show that Arctic freshwater flux started to increase rapidly in the mid-late 1990s, coincident with a decrease in the formation of dense Labrador Sea Water, a key component of the deep southward return flow od the Atlantic Meridional Overturning Circulation (AMOC). Recent freshening of the polar oceans may be reducing formation of Labrador Sea Water and hence may be weakening the AMOC. In the third study, I use InSAR to monitor ground deformation caused by CO₂ injection at an enhanced oil recovery site in west Texas. Carbon capture and storage can reduce CO₂ emitted from power plants, and is a promising way to mitigate anthropogenic warming. From 2007 to 2011, ~24 million tons of CO₂ were sequestered in this field, causing up to 10 MPa pressure buildup in a reservoir at depth, and surface uplift up to 10 cm. This study suggests that surface displacement observed by InSAR is a cost-effective way to estimate reservoir pressure change and monitor the fate of injected fluids at waste disposal and CO₂ injection sites.

1. Introduction

1.1 Overview

Satellite geodesy is the measurement of the size and shape of the earth as well as its gravity field by means of artificial satellites. Satellite geodesy is a powerful tool to monitor time variations in the Earth related to plate tectonics, post-glacial rebounds, ocean circulation, ground water extraction, and a host of other natural and anthropogenic processes. This dissertation focuses on the application of satellite geodesy to studies of environmental and global change. Data from three techniques are used: high precision Global Positioning System (GPS), Interferometric Synthetic Aperture Radar (InSAR) and the Gravity Recovery and Climate Experiment (GRACE).

The dissertation has six chapters. Chapter One (this chapter) is an introduction and summary of the work. Chapter two describes the essentials of three satellite geodesy techniques. The next three chapters (Chapter Three, Four and Five) are each based on a published, open literature paper.

Chapter Three focuses on using coastal vertical displacement observed by high precision GPS to study recent mass loss of the Greenland ice sheet. High precision GPS has been used to study a number of Earth processes, including plate motion, fault-related crustal deformation, and coastal subsidence. Many of these applications involve looking at secular (long-term) rates of surface deformation, where the displacement rate can be assumed constant over the measurement period, typically several years or longer. In a number of Earth processes, however, it is also useful to consider short-term fluctuations. Many of these applications involve changes in Earth's fluid envelope, for example annual loading and unloading of the crust associated with the hydrologic cycle. Accelerating uplift of the coastal regions of Greenland, where most of the current mass loss is concentrated (e.g., Zwally et al., 2005; Thomas et al., 2006; Luthcke et al., 2006; Rignot

and Kanagaratnam, 2006; Wouters et al., 2008), is well recorded by a network of GPS stations emplaced on the rocky margins (Bevis et al., 2012). The previous study of Jiang et al. (2010) focused on decadal scale trends and demonstrated that decadal time series of the vertical position component were well fit by a simple model of constant acceleration. Jiang et al. (2010) assumed constant amplitude of annual uplift each year, a common assumption in GPS time series analysis. However, the data show significant annual variation. More recent measurements suggest that accelerating melting of Greenland ice sheet is continuing, with some melting seasons (for example 2010, 2012) experiencing significant ice mass loss (Bevis et al., 2012; Nghiem et al., 2012). Thus, the short-term annual variation of coastal uplift measured by GPS can be useful in studying variable and accelerating ice mass loss.

One important aspect of the current retreat phase in Greenland is the role of climate forcing on melting coastal areas of Greenland. In Greenland, ice mass change is regulated by two climate factors, atmospheric forcing (Zwally et al., 2002; Hall et al., 2008) and oceanic forcing (Van de Wal et al., 2008; Holland et al., 2008; Hanna et al., 2009; Straneo et al., 2010, 2012; Straneo and Heimbach, 2013; Seale et al., 2011). Atmospheric forcing can affect surface mass balance (SMB) by changing either or both the snow accumulation rate and the ablation rate. Also, melt water can influence the basal sliding rate. Oceanic forcing can increase submarine melting of marine-terminating outlet glaciers, resulting in rapid changes in calving rate, and inducing dynamic changes upstream, including glacier acceleration and thinning (Straneo and Heimbach, 2013). GRACE satellite data documents mass loss in Greenland over the last decade, and for West Greenland, clearly shows that loss is concentrated along the coast (e.g., Wouters et al., 2008). Unfortunately these data lack the spatial resolution to investigate melting at the scale of individual drainage basins. However, coastal uplift as measured by GPS is sensitive to ice loss at this scale, which allows assessment of the influence of local climate conditions on melting. In my dissertation, both short-term and long-term surface deformation processes measured by GPS is utilized to understand the climatic forcing on mass loss. What are the main driving forces for recent accelerated mass loss of Greenland

Ice Sheet? What is the relative contribution of oceanic versus atmospheric forcing on coastal melting? Those questions will be discussed in my dissertation by using GPS data combined with other oceanographic and meteorological data.

Chapter Four uses GRACE data to estimate the recent freshwater flux from Greenland and investigates its impact on the Atlantic Meridional Overturning Circulation (AMOC). The AMOC is a major mode of ocean thermo-haline circulation. It is driven by density differences in the Atlantic Ocean, and is a key component of the global climate system. Both theoretical and numerical studies show that the AMOC is sensitive to freshwater balance because of the strong influence on sea water density (Stommel, 1961; Rooth, 1982; Rahmstorf, 1995; Stouffer et al., 2006). Past abrupt climate changes have been linked with changes in the AMOC in response to changes in the freshwater budget (Manabe and Stouffer, 1993, 1995; Clark et al., 2002). Recent anthropogenic warming and accelerated melting of the Greenland ice sheet is leading to a general freshening of the North Atlantic, raising concerns that the AMOC may soon be disrupted.

In this dissertation, I estimate Arctic freshwater flux from three sources that are undergoing rapid increases and can be estimated from remote observations: the Greenland ice sheet, CAA glaciers and Arctic sea ice. Among these, freshwater flux from Greenland is the largest component, and estimated with GRACE data and RACMO2.3 model (Ettema et al., 2009; Noël et al., 2015). The pattern of coastal currents around Greenland tends to focus coastal waters towards the Labrador Sea, an important “incubator” for dense, North Atlantic Deep Water (NADW). Southward return flow of NADW is an important component of the AMOC, hence any disruption of density balance in the Labrador Sea may be a leading indicator of changes to the AMOC. In this dissertation, I compare freshwater flux estimates to properties of Labrador Sea Water and suggest that increased freshwater flux here is starting to impact the AMOC.

Chapter Five focuses on using surface deformation observed by InSAR to study reservoir pressure change caused by fluid injection and production at an enhanced oil recovery field. Similar to GPS, InSAR has been used to study a number of Earth processes. Particularly, it has been used to monitor ground subsidence associated with oil and gas

extraction (Tomás et al., 2005). As oil reservoirs have been drawn down in the last few decades, producers have increasingly applied enhanced oil recovery (EOR) techniques to increase the amount of oil that can be extracted from a given oil field. This usually involves pumping of CO₂ or saline water into the reservoir, and raising the reservoir pressure. Similar techniques are used in “fracking” (hydraulic fracturing) to stimulate natural gas production, and later, to get rid of water. In some regions, there is concern that rapid pumping of water fluids into deep reservoirs can stimulate induced seismicity (e.g., Keranen et al., 2013; McGarr et al., 2015). Here, there is a need for research into the rock mechanical and fluid mechanical processes involved in such fluid pumping. There is also interest in pumping CO₂ from industrial plants into deep geological formations for large-scale Carbon Capture and Storage (CSS), thereby reducing CO₂ emissions to the atmosphere. Research is underway to study the geomechanical impact of CCS, including microseismicity, fault reactivation, fracturing and ground deformation (e.g., Streit and Hillis, 2004; Zhou et al., 2010; Mazzoldi et al., 2012; Rinaldi and Rutqvist, 2013; Vasco et al., 2010). Here, ground deformation associated with fluid injection and production is studied to better understand the links between surface deformation and pressure changes at depth. A numerical model incorporating rock and fluid properties is constructed to relate surface deformation to pressure changes at depth. My method offers an inexpensive way to monitor deep reservoir pressure change based on low cost commercial satellite imagery.

Chapter Six summarizes the main conclusions from the previous chapters, and makes suggestions for future research.

1.2 References

Bevis, M., Wahr, J., Khan, S. A., Madsen, F. B., Brown, A., Willis, M., Kendrick, E., Knudsen, P., Box, J. E., van Dam, T., et al. (2012). Bedrock displacements in greenland manifest ice mass variations, climate cycles and climate change. *Proceedings of the National Academy of Sciences*, 109(30):11944–11948.

- Clark, P. U., Pisias, N. G., Stocker, T. F., and Weaver, A. J. (2002). The role of the thermohaline circulation in abrupt climate change. *Nature*, 415(6874):863–869.
- Ettema, J., van den Broeke, M. R., van Meijgaard, E., van de Berg, W. J., Bamber, J. L., Box, J. E., and Bales, R. C. (2009). Higher surface mass balance of the greenland ice sheet revealed by high-resolution climate modeling. *Geophysical Research Letters*, 36(12).
- Hall, D. K., Williams, R. S., Luthcke, S. B., and Digirolamo, N. E. (2008). Greenland ice sheet surface temperature, melt and mass loss: 2000–06. *Journal of Glaciology*, 54(184):81–93.
- Hanna, E., Cappelen, J., Fettweis, X., Huybrechts, P., Luckman, A., and Ribergaard, M. (2009). Hydrologic response of the greenland ice sheet: the role of oceanographic warming. *Hydrological Processes*, 23(1):7–30.
- Holland, D. M., Thomas, R. H., De Young, B., Ribergaard, M. H., and Lyberth, B. (2008). Acceleration of jakobshavn isbrae triggered by warm subsurface ocean waters. *Nature Geoscience*, 1(10):659–664.
- Jiang, Y., Dixon, T. H., and Wdowinski, S. (2010). Accelerating uplift in the north atlantic region as an indicator of ice loss. *Nature Geoscience*, 3(6):404–407.
- Keranen, K. M., Savage, H. M., Abers, G. A., and Cochran, E. S. (2013). Potentially induced earthquakes in oklahoma, usa: Links between wastewater injection and the 2011 mw 5.7 earthquake sequence. *Geology*, 41(6):699–702.
- Luthcke, S. B., Zwally, H., Abdalati, W., Rowlands, D., Ray, R., Nerem, R., Lemoine, F., McCarthy, J., and Chinn, D. (2006). Recent greenland ice mass loss by drainage system from satellite gravity observations. *Science*, 314(5803):1286–1289.
- Manabe, S. and Stouffer, R. J. (1993). Century-scale effects of increased atmospheric co 2 on the ocean-atmosphere system. *Nature*, 364(6434):215–218.

Manabe, S. and Stouffer, R. J. (1995). Simulation of abrupt climate change induced by freshwater input to the north atlantic ocean. *Nature*, 378(6553):165–167.

Mazzoldi, A., Rinaldi, A. P., Borgia, A., and Rutqvist, J. (2012). Induced seismicity within geological carbon sequestration projects: maximum earthquake magnitude and leakage potential from undetected faults. *International Journal of Greenhouse Gas Control*, 10:434–442.

McGarr, A., Bekins, B., Burkardt, N., Dewey, J., Earle, P., Ellsworth, W., Ge, S., Hickman, S., Holland, A., Majer, E., et al. (2015). Coping with earthquakes induced by fluid injection. *Science*, 347(6224):830–831.

Nghiem, S., Hall, D., Mote, T., Tedesco, M., Albert, M., Keegan, K., Shuman, C., DiGirolamo, N., and Neumann, G. (2012). The extreme melt across the greenland ice sheet in 2012. *Geophysical Research Letters*, 39(20).

Noël, B., van de Berg, W., Meijgaard, E. v., Kuipers Munneke, P., van de Wal, R., and van den Broeke, M. (2015). Summer snowfall on the greenland ice sheet: a study with the updated regional climate model racmo2. 3. *The Cryosphere Discussions*, 9(1):1177–1208.

Rahmstorf, S. (1995). Bifurcations of the atlantic thermohaline circulation in response to changes in the hydrological cycle. *Nature*, 378(6553):145–149.

Rignot, E. and Kanagaratnam, P. (2006). Changes in the velocity structure of the greenland ice sheet. *Science*, 311(5763):986–990.

Rinaldi, A. P. and Rutqvist, J. (2013). Modeling of deep fracture zone opening and transient ground surface uplift at kb-502 co 2 injection well, in salah, algeria. *International Journal of Greenhouse Gas Control*, 12:155–167.

Rooth, C. (1982). Hydrology and ocean circulation. *Progress in Oceanography*, 11(2):131–149.

- Seale, A., Christoffersen, P., Mugford, R. I., and O’Leary, M. (2011). Ocean forcing of the greenland ice sheet: Calving fronts and patterns of retreat identified by automatic satellite monitoring of eastern outlet glaciers. *Journal of Geophysical Research: Earth Surface (2003–2012)*, 116(F3).
- Stommel, H. (1961). Thermohaline convection with two stable regimes of flow. *Tellus*, 13(2):224–230.
- Stouffer, R. J., Yin, J., Gregory, J., Dixon, K., Spelman, M., Hurlin, W., Weaver, A., Eby, M., Flato, G., Hasumi, H., et al. (2006). Investigating the causes of the response of the thermohaline circulation to past and future climate changes. *Journal of Climate*, 19(8):1365–1387.
- Straneo, F., Hamilton, G. S., Sutherland, D. A., Stearns, L. A., Davidson, F., Hammill, M. O., Stenson, G. B., and Rosing-Asvid, A. (2010). Rapid circulation of warm subtropical waters in a major glacial fjord in east greenland. *Nature Geoscience*, 3(3):182–186.
- Straneo, F. and Heimbach, P. (2013). North atlantic warming and the retreat of greenland’s outlet glaciers. *Nature*, 504(7478):36–43.
- Straneo, F., Sutherland, D. A., Holland, D., Gladish, C., Hamilton, G. S., Johnson, H. L., Rignot, E., Xu, Y., and Koppes, M. (2012). Characteristics of ocean waters reaching greenland’s glaciers. *Annals of Glaciology*, 53(60):202–210.
- Streit, J. E. and Hillis, R. R. (2004). Estimating fault stability and sustainable fluid pressures for underground storage of co 2 in porous rock. *Energy*, 29(9):1445–1456.
- Thomas, R., Frederick, E., Krabill, W., Manizade, S., and Martin, C. (2006). Progressive increase in ice loss from greenland. *Geophysical Research Letters*, 33(10).
- Tomás, R., Márquez, Y., Lopez-Sánchez, J. M., Delgado, J., Blanco, P., Mallorquí, J. J., Martínez, M., Herrera, G., and Mulas, J. (2005). Mapping ground subsidence induced by aquifer overexploitation using advanced differential sar interferometry: Vega media of the segura river (se spain) case study. *Remote Sensing of Environment*, 98(2):269–283.

- Van de Wal, R., Boot, W., Van den Broeke, M., Smeets, C., Reijmer, C., Donker, J., and Oerlemans, J. (2008). Large and rapid melt-induced velocity changes in the ablation zone of the greenland ice sheet. *science*, 321(5885):111–113.
- Vasco, D., Rucci, A., Ferretti, A., Novali, F., Bissell, R., Ringrose, P., Mathieson, A., and Wright, I. (2010). Satellite-based measurements of surface deformation reveal fluid flow associated with the geological storage of carbon dioxide. *Geophysical Research Letters*, 37(3).
- Wouters, B., Chambers, D., and Schrama, E. (2008). Grace observes small-scale mass loss in greenland. *Geophysical Research Letters*, 35(20).
- Zhou, R., Huang, L., and Rutledge, J. (2010). Microseismic event location for monitoring co₂ injection using double-difference tomography. *The Leading Edge*, 29(2):208–214.
- Zwally, H. J., Abdalati, W., Herring, T., Larson, K., Saba, J., and Steffen, K. (2002). Surface melt-induced acceleration of greenland ice-sheet flow. *Science*, 297(5579):218–222.
- Zwally, H. J., Giovinetto, M. B., Li, J., Cornejo, H. G., Beckley, M. A., Brenner, A. C., Saba, J. L., and Yi, D. (2005). Mass changes of the greenland and antarctic ice sheets and shelves and contributions to sea-level rise: 1992–2002. *Journal of Glaciology*, 51(175):509–527.

2. Technical Background

2.1 Introduction

Satellite geodesy can be considered a multi-parameter estimation problem involving range (distance) or range rate (Seeber, 2003). The fundamental equation of satellite geodesy can be expressed as (Figure 2.1).

$$\mathbf{r}_j(t) = \mathbf{r}_i(t) + \Delta\mathbf{r}_{ij}(t) \quad (2.1)$$

where $\mathbf{r}_j(t)$ is the satellite position at time t , $\mathbf{r}_i(t)$ is the receiver position at time t , and $\Delta\mathbf{r}_{ij}(t)$ is the time-varying range between receiver and satellite. Range is both the observable (sometimes called pseudorange since it is biased by a number of error sources) and a parameter to be estimated. For Global Positioning System (GPS), receiver position is determined using satellite position and range estimates. For Interferometric Synthetic Aperture Radar (InSAR), range change (surface displacement) between two time periods is determined using two or more satellite passes. For the Gravity Recovery and Climate Experiment (GRACE), range and range rate between two GPS satellites is observed and used to compute changes in the Earth's gravity field. All three techniques rely on precise ranging measurements using the microwave portion of the electromagnetic spectrum, with wavelengths between 0.1 cm and 100 cm and are affected by some common error sources.

It is useful to distinguish two types of range measurements, one based on signal propagation time and knowledge of the speed of light (sometimes called pseudorange) and carrier phase. Due to the satellite-receive motion (satellite moves towards or away from receiver during a transmission cycle), carrier phase is sometimes considered equivalent to range rate, also known as accumulated Doppler range. Carrier phase is more precise, but suffers from phase ambiguity, which must be solved with additional information. In GPS, both measurements are used: pseudorange for a “first cut” estimate and then carrier

phase for a refined estimate. In the case of carrier phase ranging, the range between two points can be expressed in terms of the number of whole wavelength and the partial signal wavelength between the transmitter and receiver (2.2):

$$|\Delta \mathbf{r}_{ij}| = N \cdot \lambda + \frac{\phi}{2\pi} \lambda \quad (2.2)$$

where $|\Delta \mathbf{r}_{ij}|$ is the range between transmitter and receiver, λ is the wavelength of the carrier signal, N is the integer number of signal wavelength, ϕ is the phase measurement which is obtained by comparing the original outgoing wave and received incoming wave. The number of wavelength is unknown or ambiguous. Resolving the ambiguity of the carrier phase measurement is required for precise ranging. In GPS, this is known as ambiguity resolution, while in InSAR it is referred to as phase unwrapping.

Note that carrier phase and pseudorange measurements can be performed in a one-way mode or two-way mode. One-way ranging is used by GPS and GRACE, while two-way ranging is used for InSAR.

As shown in Figure 2.1, precise time-dependent satellite position, $r_j(t)$, are required in satellite geodesy. The accuracy of final results of satellite geodesy depends on the accuracy of satellite orbits. To compute the coordinates of the receiver, it is necessary to know the exact position of each satellite observed. To a first approximation, knowledge of GPS satellite orbits at the 1 m accuracy level is required to determine the position of a ground receiver at the 1 cm accuracy level. For InSAR, even tighter constraints on satellite orbits are required. For GRACE satellites, the satellite orbits are required to relate range and range rate measurement to a global reference frame.

The microwave signals, when propagating from transmitter to receiver, are subject to atmospheric effect. For GRACE, this is restricted to ionospheric effects. For GPS and InSAR, it includes ionospheric effect as well as tropospheric propagation delay. The ionosphere is the upper layer of the Earth's atmosphere, from about 60 km to 1000 km altitude. It contains charged particles due to high energy interactions between atmospheric molecules and radiation from the Sun and cosmic rays. The influence of ionosphere on

the propagation of microwave signal is dispersive. The ionospheric propagation delay depends on the electron density along the signal path as well as the signal frequency.

The troposphere is the lower layer of the Earth's atmosphere, from the Earth surface to approximately 15 km altitude. It contains approximately 75% of the atmosphere's total mass and 99% of its water vapor. The troposphere is an electrically neutral and its influence on the propagation of microwave signal is non-dispersive. The tropospheric propagation delay depends on the meteorological status, namely air pressure, partial pressure of water vapor, pressure of dry gas and temperature. For all three techniques, atmospheric effects have to be determined and corrected in order to obtain high precision results.

2.2 Global Positioning System

The Global Positioning System (GPS) was developed by the U.S Department of Defense (DoD) to provide civilian and military users with worldwide positioning, navigation and timing services. The position measurements can be used to study the movements of the Earth surface (deformation) associated with different Earth processes. Here, a brief introduction about the principles of GPS and errors sources of the GPS position measurement is presented. For detailed studies, the reader is referred to Dixon (1991), Mao et al. (1999) and Hofmann et al. (2001).

2.2.1 Structure

The GPS system consists of three segments: the space segment, the control segment, and the user segment. The space segment consists of the GPS satellites that transmit radio signals to users. The nominal GPS constellation consists 24 satellites that are equally spaced in 6 orbital planes with 4 satellites in each plane (Figure 2.3). Orbital planes are 60 degree separated and inclined at about 55 degrees with respect to the equatorial plane. Each satellite flies in high Earth orbit at an altitude of about 20200 km, circling the Earth twice per day. This constellation ensures that users can view at least 4 satellites from any point on the Earth at any time. The control segment on the ground consists of a system of facilities that receive signals from the satellites, perform

analysis to compute satellite orbital data (ephemerides) and clock corrections, and send ephemerides back to each satellite for re-broadcast to users. The user segment consists of the GPS receivers that receive the signals from the GPS satellite and convert them into three-dimensional position, time and other parameters.

2.2.2 GPS signal

Each GPS satellite transmits microwave signals on two carrier frequencies: L1 (1575.42 MHz) and L2 (1227.60 MHz). Two pseudorandom noise (PRN) codes and broadcast message (data signal) are modulated onto the carrier frequencies. The PRN codes are a sequence of binary values which look like random electrical noise to users without code knowledge. Maximum autocorrelation can be achieved when two code sequences coincide exactly, allowing determination of signal travel time. Two types of PRN codes are used: the Precision (P) code and the Coarse/Acquisition (C/A) code. The main features of carrier, code and data signals are shown in Table 2.1.

The C/A code is modulated onto the L1 carrier. The P code is modulated onto the L1 and L2 carriers. The P-code is encrypted into Y-code in the Anti-Spoofing (AS) mode, which denies access by unauthorized users (Figure 2.4). Note that as a major focus of the GPS modernization program, a new military (M) signal and three new civil (L1C, L2C, L5) have been added to the L1 and L2 carriers.

2.2.3 GPS basic observations

To determine three-dimensional position of a user, the GPS receiver should compute the range to at least four satellites, combined with knowledge of satellites positions at the time of signal transmission. However, due to lack of synchronicity between satellite clock and receiver clock, plus other factors, the GPS receiver can only provide pseudorange measurements rather than the true geometric range. GPS receivers provide two types of pseudorange observations: code pseudorange and carrier phase pseudorange. The code pseudorange is obtained by multiplying the speed of light by the travel time, where the travel time is determined by correlating the received code (C/A or P(Y)) from the satellite with the replicas generated by the receiver. The carrier phase pseudorange

is obtained by multiplying the wavelength by difference between carrier phase from the satellite and the carrier phase generated by the receiver. Carrier phase pseudorange is about two orders of magnitude more precise than the code pseudorange, but the carrier phase observation is ambiguous by an integer number of cycles (Remondi, 1985). In order to achieve millimeter-precision, the ambiguity problem must be fixed. Carrier phase ambiguity resolution has been studied by Lichten and Border (1987) and Blewitt (1989, 2008).

2.2.4 GPS error sources

There are many sources of error contaminating the GPS position measurements. Major GPS error sources are briefly discussed below. For a detailed description, the reader is referred to Hofmann et al. (2001).

(i) Satellite clock and orbit errors

GPS satellite clock time should be synchronous with GPS time (the time scale used by the GPS system). Errors in the satellite clock estimate have a major impact on the computed code pseudorange. Similarly, errors in the satellite orbit estimate can corrupt the ground position estimate. In this dissertation, I use the precise final orbits and adjusted clock products provided by the Jet Propulsion Laboratory to mitigate satellite clock and orbit errors. Another source of precise satellite orbits and adjusted clock products is the International GNSS Service (IGS).

(ii) Atmospheric effects

The GPS signals are refracted by ionosphere and troposphere, causing ray bending and changing the propagation time. The first-order effects of the ionosphere can be corrected using the dual-frequency approach and a linear combination of carrier phase measurements. The remaining high-order ionospheric effects are less than 1 mm (Hernandez-Pajares et al., 2007; Petrie et al., 2010). The tropospheric effects can be reduced by using an elevation mask to avoid receiving signals from satellites lower than a certain elevation. The tropospheric delay must be modeled. The tropospheric model consists of mean tropospheric parameters or measurements data (temperature, air pressure, water vapor) and a mapping function (Niell, 1996; Boehm et al., 2006, 2007).

(iii) Multipath effects

The following section is summarized from the work of Larson et al. (2007). The receiver antenna gets a direct signal through a straight-line path, plus reflected signals through multiple paths. The path length of the reflected signal is longer than the direct signal, causing errors to both code and carrier-phase observations, which then propagate into position solutions. Multipath effects on code observation are much larger than on the carrier-phase observation. Two types of multipath exist: diffuse multipath and specular multipath. Diffuse multipath occurs when the GPS signal reaches a rough surface and the reflected signal is scattered in multiple directions. Diffuse multipath causes unbiased and time-uncorrelated errors which can be easily removed through real-time signal filtering in the receiver. Specular multipath occurs when the GPS signal reaches a smooth surface and then is reflected into a single direction. In contrast to errors caused by diffuse multipath, errors caused by specular multipath are systematic and time-correlated which cannot be removed by traditional filtering methods. To date there is no widely used model for multipath effect correction since the multipath-generating environment is dynamic and it is unique for each GPS site. Various approaches have been developed to for multipath effect reduction and correction. For example, one can estimate the multipath corrections from SNR data (e.g., Axelrad et al., 1996) or mitigate the multipath errors using the sidereal filtering technique, relying upon the repeating orbital characteristics of the GPS satellites (e.g., Genrich and Bock, 1992; Choi et al., 2004). The aspect repeat time adjustment (ARTA) technique has also been suggested to maximize the effectiveness of techniques relying upon the geometric repeatability of GPS satellite orbits (Larson et al., 2007). In our processing routine, we estimate observations every 24 hours to minimize the multipath error (Sella et al., 2002).

(iv) Antenna phase center offset and variation

The electrical antenna phase center (APC) is the point in space where radio signal is received. However, the position of the APC varies depending on the intensity and direction of the incoming signal. Thus, antenna phase center variation (PCV) is defined as the difference between the APC of each measurement and the mean position of the

electrical antenna phase center (MPC). The antenna phase center offset (PCO) is defined as the difference between MPC and antenna reference point (ARP) given by the manufacturer. Steigenberger et al. (2006) reprocessed years of GPS data and estimated the antenna phase center offsets for a variety of GPS receivers. An absolute phase center correction model estimated by Schmid et al. (2007) can be used to calibrate both GPS satellite and receiver antennas.

Note that only the major error sources are discussed here. Other factors such as receiver clock error, monument movement and software accuracy (e.g., mis-modeling of key physical processes) also cause errors in the GPS position measurement. Last but not least, deformations due to ocean tidal and atmospheric loading need to be modeled and removed so that the geophysical process of interest (e.g., ice mass loss) can be separated from other geophysical processes. The specific models used are described below.

In this dissertation, GPS analysis is conducted with the Precise Point Positioning software developed by JPL GIPSY/OASIS (Zumberge et al., 1997). JPL's precise orbits and clock products are used to generate daily point position solutions. The dual-frequency approach and a linear combination of carrier phase measurements are used for correcting the first-order effects of the ionospheric effect. Tropospheric effects are modeled using the Global Mapping Function (Boehm et al., 2006). The elevation cut-off angle is chosen to 7 ° in order to better constrain tropospheric effects meanwhile to minimize multipath errors. The ocean loading effects are corrected using the FES2004 model (Lyard et al., 2006). The non-tidal atmospheric loading effects are corrected using a global 2.5×2.5 degree displacement field computed from a model provided by the National Center for Environmental Protection (Petrov and Boy, 2004). The Ambizap algorithm (Blewitt, 2008) is adopted to solve integer ambiguities for each station. The non-fiducial daily solutions are then aligned to the IGS05 reference frame (Altamimi et al., 2007) using JPL's X-files, a 7-parameter transformation.

2.3 Interferometric Synthetic Aperture Radar

Interferometric Synthetic Aperture Radar (InSAR) is a radar technique for mapping the Earth topography and/or Earth surface deformation using an interferogram

formed by two Synthetic Aperture Radar (SAR) images. Using InSAR to study Earth surface deformation is briefly summarized here. The reader is referred to Curlander and McDonough (1991), Massonnet and Feigl (1998), Rosen et al. (2000) and Hanssen (2001) for more detailed reviews.

2.3.1 Basic concept

A satellite borne Synthetic Aperture Radar (SAR) transmits a pulse of microwave signals to illuminate a target area on the Earth and then receives the returned signal scattered by the Earth's surface. The returned signal contains two kinds of information: amplitude and phase, which are recorded in a two-dimensional radar image. The amplitude is a measure of target reflectivity, which reflects the physical properties of ground target. The phase corresponds to the fractional part of the round trip range between satellite antenna and ground target. Current satellite borne SARs typically work in three microwave bands: X-band (wavelength of ~ 3 cm), C-band (wavelength of ~ 6 cm) and L-band (wavelength of ~ 24 cm). With a high bandwidth microwave signal and the synthetic aperture technique (transmit and receive signals using a radar antenna installed on a moving platform), satellite borne SAR image can achieve high spatial resolution.

InSAR uses two SAR images to produce an interferogram which contains the phase difference (also called interferometric phase, ϕ) between every pair of corresponding pixels in two SAR images. The range change ($R_2 - R_1$) between two image acquisitions is then measured in terms of the interferometric phase (ϕ):

$$\phi = \frac{4\pi}{\lambda} (R_2 - R_1) \quad (2.3)$$

where λ is the carrier wavelength, $R_{1,2}$ is the range from satellite antenna $A_{1,2}$ to the ground target (Figure 2.5). As with GPS, the phase of SAR image is ambiguous because it is only the fractional part of the change in phase. Therefore, the interferometric phase needs to be unwrapped. Phase unwrapping is a critical step for using InSAR to monitor topography or surface deformation and various approaches have been developed to solve the problem (e.g., Zebker and Lu, 1998).

2.3.2 Monitoring surface deformation

If the two SAR images are acquired from slightly different viewing points at different times, any movement of the ground target with a component projected onto the line of sight (LOS) of the radar beam gives the deformation phase:

$$\phi_{def} = \frac{4\pi}{\lambda}(\delta R) \quad (2.4)$$

where ϕ_{def} is the interferometric phase caused by surface deformation; λ is the carrier wavelength; δR is the range change, which is the surface displacement projected onto the LOS of the radar beam. Theoretically, if ϕ_{def} is known, the surface displacement can be determined at millimeter-precision. However, besides deformation phase, other phase terms also contribute to the interferometric phase measurement (ϕ):

$$\phi = \phi_{def} + \phi_{topo} + \phi_{atm} + \phi_{orb} \quad (2.5)$$

where ϕ_{topo}, ϕ_{atm} and ϕ_{orb} are the phase due to range changes associated with topography, atmospheric effects and orbit errors. In order to monitor surface deformation, ϕ_{topo}, ϕ_{atm} and ϕ_{orb} should be removed from ϕ .

(i) Topography

In most cases, two SAR images are taken from slightly different viewing points ($A_{1,2}$) so that the interferometric phase contains the topographic component (Figure 2.5). A Digital Elevation Model (DEM) is used to represent the topography. Thus, if an accurate DEM is available, the topographic phase can be estimated and then subtracted from the interferometric phase. Note that errors in the DEM cause tropospheric phase residuals in the deformation phase. In place of a DEM, the differential InSAR technique can be used to separate topographic phase from deformation phase. Two or more interferograms with different baselines are differenced to produce differential interferograms. In practice, along with topographic phase the reference phase induced by acquisition geometry is estimated and subtracted from the interferometric phase.

(ii) Atmospheric effects

As with GPS, it is important to consider atmospheric effects on monitoring surface deformation using InSAR (Goldstein, 1995; Zebker et al., 1997). The state of atmosphere changes if the two images are acquired at different times. Atmospheric heterogeneity leads to differences in atmospheric delay and hence the phase difference. Temporal and spatial variations of atmospheric pressure, temperature and water vapor all leads to errors in deformation. Particularly large errors (~ 10 cm) in deformation measurements can result from variations (20%) of atmospheric water vapor (Zebker et al., 1997). Producing robust estimates of atmospheric delay remains to be one of the challenges in improving the accuracy of surface deformation with the InSAR technique. A variety of methods have been proposed to reduce the effects of atmospheric delay, including averaging multiple interferograms to cancel out uncorrelated atmospheric delay (e.g., Zebker et al., 1997), spatial-temporal filtering (e.g., Berardino et al., 2002), and using complementary data such as GPS data and meteorological models to estimate atmospheric delay (e.g., Williams et al., 1998; Foster et al., 2006; Jolivet et al., 2014).

(iii) Orbital errors Errors in the satellite orbits are a limitation for InSAR in measuring surface deformation accurately. To remove both tropographic phase and reference phase (together called geometric phase), precise satellite orbits are required to determine the interferometric baseline to millimeter precision. However, orbits of most remote sensing satellites are much less precise, e.g., 10 cm – 1m (Yoon et al., 2009; Eineder et al., 2011; Rudenko et al., 2012), hence the interferometric baseline cannot be precisely determined directly. Therefore, orbital errors contributes to phase difference in the interterograms. Several methods have been proposed to reduce the effects of orbital errors. A simple but widely used method is to estimate a planar phase ramp that fits to interferometric phases (Massonnet and Feigl, 1998).

Besides the factors discussed above, phase noise induced by the radar system (e.g., thermal noise), changes in the scattering behavior of the ground target (e.g., changes in dielectric constant), and data processing (e.g., phase unwrapping) errors also contribute to the interferometric phase, all inducing errors in the InSAR measurements.

2.4 Gravity Recovery and Climate Experiment

Launched in March 2002, the Grace Recovery and Climate Experiment (GRACE) mission makes detailed measurements of the time varying gravity field of the Earth with a spatial resolution of ~ 300 km (Tapley et al., 2004; Wahr et al., 2004). GRACE measures gravity variations that are related to the redistributions of mass in the solid Earth and its fluid envelope. Currently, many studies focus on mass redistribution processes occurring in the hydrosphere, cryosphere and the ocean, which are within a thin layer at the Earth's surface. Here, the principle of GRACE measurement and its application in measuring the Earth's surface mass change are briefly summarized. The reader is referred to Wouters et al. (2014) for more a detailed review.

2.4.1 Basic concept

GRACE consists of two identical satellites at altitude of about 500 km, one following the other in a low, near-circular, near-polar orbit with an inclination of 89° , ~ 220 km apart along-track (Figure 2.6). A highly accurate inter-satellite, K-Band microwave range (KBR) system, continuously measures the range between two satellites. Each satellite transmits carrier phase to the other at dual-frequency (24 and 32 GHz), allowing for ionospheric correction during data processing. Each satellite receives the carrier phase and compares it with the on-board generated phase in order to obtain the range between two satellites. Changes in range contains gravitational information: the leading satellite accelerates when passing an area of stronger gravity (anomaly), resulting in range increase between the two satellite; the leading satellite then decelerates when past the anomaly and the trailing satellite accelerates, resulting in a range decrease. In addition to the KBR system, each satellite is equipped with a GPS receiver, a high precision accelerometer and star cameras. The GPS receiver provides the position of two GRACE satellites and the time-tags of KBR measurements. The accelerometer is used to measure the surface force acceleration so that the effects of non-gravitational forces, such as air drag and solar radiation pressure, can be removed from the range-rate measurement. The star cameras are used to measure the orientation of satellites in space so that the K-Band antennas are pointing towards each other precisely.

2.4.2 Data Products

The GRACE gravity data products are developed, processed and archived by three centers within a shared Science Data System (SDS): Jet Propulsion Laboratory (JPL), the Center for Space Research at the University of Texas (UTCSR), and the Geoforschungszentrum in Potsdam (GFZ). The GRACE gravity data product is divided into three levels: Level-0, Level-1, Level-2.

Level-0 data is the raw data from GRACE satellite. It is the result of telemetry data reception, collection and documentation by the Raw Data Center (RDC) of the Mission Operation System (MOS) in Germany. Level-0 data product is not available to the public.

Level-1 data product is divided into two levels: Level-1A and Level-1B. Level-1A data product is the result of reversible processing applied to the Level 0 data. The data is calibrated, time-tagged to the respective satellite receiver clock time and reformatted for further processing. Level-1B data product is the result of extensive and irreversible processing applied to Level-0 and Level-1A data products. The data is correctly time-tagged and the data sample rate is reduced from 10 Hz to 0.1 Hz. Level-1B data product includes inter-satellite range, range-rate, range-acceleration, the non-gravitational acceleration for each satellite, etc. Level-1B data product is available to the public.

Level-2 data are processed by JPL, GFZ and UTCSR independently and are released to the public through two portals: the Physical Oceanography Distributed Active Archive Center (PO.DAAC) at JPL and the Information System & Data Center (ISDC) at GFZ. Level-2 data products include the orbit of the GRACE satellites, monthly and mean estimates of spherical harmonic (Stokes) coefficients (C_{lm} , S_{lm}) of the Earth gravity field. Note that the degree (l) and order (m) of the Stokes coefficients are up to 60 for CSR and 120 for JPL and GFZ. Most scientific studies based on GRACE measurements utilize Level-2 data products. The latest version of the gravity field coefficients is Release-05, which is more accurate than the previous versions based on better knowledge of on-board instruments (star cameras, accelerometer and the KBR system) and updated

mean gravity field and other background force models (e.g., ocean tide model, pole tide model, etc) for Level-2 processing (Chambers and Bonin, 2012).

2.4.3 Measuring the Earth's surface mass change

How do we use GRACE gravity data to measure the surface mass change? Here, we consider surface mass change as a thin layer of water on the Earth's surface with varying thickness. According to Wahr et al. (1998), the surface mass density $\Delta\sigma$ [kg m⁻²] can be expressed as:

$$\Delta\sigma(\phi, \lambda) = \frac{a_e \rho_e}{3} \sum_{l=0}^{\infty} \sum_{m=0}^l \frac{2l+1}{1+k_l} P_{lm}(\cos\phi) [\Delta C_{lm} \cos(m\lambda) + \Delta S_{lm} \sin(m\lambda)] \quad (2.6)$$

where ϕ, λ are the colatitude and longitude of a point above the Earth's surface, a_e is the mean equatorial radius of the Earth, ρ_e is the mean density of the Earth, l and m are the degree and order of the spherical harmonic coefficients, k_l is the Love number of degree l , P_{lm} is the Legendre Polynomials of degree l and order m , and ΔC_{lm} and ΔS_{lm} are the coefficients for some month of l degree and m order released by GRACE. Many studies report mass change using changes in height of water by dividing $\Delta\sigma$ [kg m⁻²] by the density of water ρ_w [kg m⁻³].

Several processing procedures need to be applied to the GRACE gravity field solutions in order to estimate surface mass change correctly.

(i) Striping effect Spatially correlated errors in the Stokes coefficients cause the north-south oriented stripes in maps of surface mass change, which is called the striping effect (Figure 2.7a). Such errors are prominent in the high degree Stokes coefficients. Several techniques have been developed to reduce the striping effect in the gravity field solution. One common technique is Gaussian smoothing (Figure 2.7c), which uses a bell-shaped Gaussian kernel to ‘blur’ images and remove detail and noise. The Gaussian kernel is isotropic, meaning that the behavior of the function is the same in any direction. However, the striping effect in GRACE data is non-isotropic, orienting in North-South direction. Therefore, some non-isotropic kernels are developed to reduce the striping

effects (e.g., Chen et al., 2006b; Kusche et al., 2009). Swenson and Wahr (2006) developed a correlated-error filter which further reduce the noise in GRACE data (Figure 2.7).

(ii) Leakage effects

The limited spatial resolution of the GRACE gravity field solution and spatial smoothing causes leakage, where signals do not concentrated solely over the region of mass variation but spread out into nearby regions artificially (e.g., Chen et al., 2006a). Thus, the surface mass variation over a region of interest could be contaminated by signals leaking from nearby regions, or by signals leaking out to nearby regions. It is important to identify and correct leakage effects in order to obtain correct estimates of surface mass change using GRACE gravity data. Using an averaging function is a simple method to minimize the combined measurement error and leakage error, and the result is then scaled to avoid signal attenuation (Velicogna and Wahr, 2006). The mascon technique is utilized to better localize the mass variation over a relatively small region (Rowlands et al., 2005). The original KBR range rate data and the analytical skills are required to produce the Gravity field solution using the mascon technique, making this technique less doable for most GRACE users. Schrama and Wouters (2011) proposed an inversion modeling technique based on a least squares approximation method to estimate the optimized uniform mass variation in each block. The inversion modeling technique is useful to estimate surface mass changes in high spatial resolution and is easy to use.

(iii) Glacial Isostatic Adjustment

Glacial isostatic adjustment (GIA) is the ongoing movement of the lands that were depressed by ice sheets during the last glacial period. The redistribution of lithospheric masses, adjusting from the ice sheet loading state back to the equilibrium state, causes long-term trends in the Earth's gravity field. To study the current surface mass changes, it is important to quantify and separate the long-term trend caused by GIA from the current signal of interest. The GIA model is composed of an ice model and the Earth rheology model. The ice model describes the loading and unloading history of ice sheets. The Earth rheology model describes the redistribution of lithospheric masses forced by the surface loading and unloading events. The present-day crustal uplift data are used

to calibrate GIA models. Although it is possible to model the GIA effect and subtract it from the GRACE data, it is challenging to predict the GIA effect accurately (Thomas et al., 2011). Thus, GIA effect remains one of the error sources of surface mass change using GRACE gravity data.

2.5 References

- Altamimi, Z., Collilieux, X., Legrand, J., Garayt, B., and Boucher, C. (2007). Itrf2005: A new release of the international terrestrial reference frame based on time series of station positions and earth orientation parameters. *Journal of Geophysical Research: Solid Earth*, 112(B9).
- Axelrad, P., Comp, C. J., and Macdoran, P. F. (1996). Snr-based multipath error correction for gps differential phase. *Aerospace and Electronic Systems, IEEE Transactions on*, 32(2):650–660.
- Berardino, P., Fornaro, G., Lanari, R., and Sansosti, E. (2002). A new algorithm for surface deformation monitoring based on small baseline differential sar interferograms. *Geoscience and Remote Sensing, IEEE Transactions on*, 40(11):2375–2383.
- Blewitt, G. (1989). Carrier phase ambiguity resolution for the global positioning system applied to geodetic baselines up to 2000 km. *Journal of Geophysical Research*, 94(B8):10187–10203.
- Blewitt, G. (2008). Fixed point theorems of gps carrier phase ambiguity resolution and their application to massive network processing: Ambizap. *Journal of Geophysical Research: Solid Earth (1978–2012)*, 113(B12).
- Boehm, J., Heinkelmann, R., and Schuh, H. (2007). Short note: a global model of pressure and temperature for geodetic applications. *Journal of Geodesy*, 81(10):679–683.
- Boehm, J., Niell, A., Tregoning, P., and Schuh, H. (2006). Global mapping function (gmf): A new empirical mapping function based on numerical weather model data. *Geophysical Research Letters*, 33(7).

- Chambers, D. P. and Bonin, J. (2012). Evaluation of release-05 grace time-variable gravity coefficients over the ocean. *Ocean Science*, 8(5):859–868.
- Chen, J., Wilson, C., Blankenship, D., and Tapley, B. (2006a). Antarctic mass rates from grace. *Geophysical Research Letters*, 33(11).
- Chen, J., Wilson, C., and Seo, K.-W. (2006b). Optimized smoothing of gravity recovery and climate experiment (grace) time-variable gravity observations. *Journal of Geophysical Research: Solid Earth*, 111(B6).
- Choi, K., Bilich, A., Larson, K. M., and Axelrad, P. (2004). Modified sidereal filtering: Implications for high-rate gps positioning. *Geophysical research letters*, 31(22).
- Curlander, J. C. and McDonough, R. N. (1991). *Synthetic aperture radar*. John Wiley & Sons New York, NY, USA.
- Dixon, T. H. (1991). An introduction to the global positioning system and some geological applications. *Reviews of Geophysics*, 29(2):249–276.
- Eineder, M., Minet, C., Steigenberger, P., Cong, X., and Fritz, T. (2011). Imaging geodesy—toward centimeter-level ranging accuracy with terrasar-x. *Geoscience and Remote Sensing, IEEE Transactions on*, 49(2):661–671.
- Foster, J., Brooks, B., Cherubini, T., Shacat, C., Businger, S., and Werner, C. (2006). Mitigating atmospheric noise for insar using a high resolution weather model. *Geophysical Research Letters*, 33(16).
- Genrich, J. F. and Bock, Y. (1992). Rapid resolution of crustal motion at short ranges with the global positioning system. *Journal of Geophysical Research: Solid Earth*, 97(B3):3261–3269.
- Goldstein, R. (1995). Atmospheric limitations to repeat-track radar interferometry. *Geophysical research letters*, 22:2517–2517.
- Hanssen, R. F. (2001). *Radar interferometry: data interpretation and error analysis*, volume 2. Springer Science & Business Media.

Hernandez-Pajares, M., Juan, J., Sanz, J., and Orús, R. (2007). Second-order ionospheric term in gps: Implementation and impact on geodetic estimates. *Journal of Geophysical Research: Solid Earth*, 112(B8).

Hofmann, B., Lichtenegger, H., and Collins, J. (2001). Gps theory and practice. *Wien: Springer-Verlag*, 5.

Jolivet, R., Agram, P. S., Lin, N. Y., Simons, M., Doin, M.-P., Peltzer, G., and Li, Z. (2014). Improving insar geodesy using global atmospheric models. *Journal of Geophysical Research: Solid Earth*, 119(3):2324–2341.

Kusche, J., Schmidt, R., Petrovic, S., and Rietbroek, R. (2009). Decorrelated grace time-variable gravity solutions by gfz, and their validation using a hydrological model. *Journal of geodesy*, 83(10):903–913.

Larson, K. M., Bilich, A., and Axelrad, P. (2007). Improving the precision of high-rate gps. *Journal of Geophysical Research: Solid Earth*, 112(B5).

Lichten, S. M. and Border, J. S. (1987). Strategies for high-precision global positioning system orbit determination. *Journal of Geophysical Research: Solid Earth (1978–2012)*, 92(B12):12751–12762.

Lyard, F., Lefevre, F., Letellier, T., and Francis, O. (2006). Modelling the global ocean tides: modern insights from fes2004. *Ocean Dynamics*, 56(5-6):394–415.

Mao, A., Harrison, C. G., and Dixon, T. H. (1999). Noise in gps coordinate time series. *Journal of Geophysical Research: Solid Earth (1978–2012)*, 104(B2):2797–2816.

Massonnet, D. and Feigl, K. L. (1998). Radar interferometry and its application to changes in the earth’s surface. *Reviews of geophysics*, 36(4):441–500.

Niell, A. (1996). Global mapping functions for the atmosphere delay at radio wavelengths. *Journal of Geophysical Research: Solid Earth*, 101(B2):3227–3246.

- Petrie, E. J., King, M. A., Moore, P., and Lavallée, D. A. (2010). Higher-order ionospheric effects on the gps reference frame and velocities. *Journal of Geophysical Research: Solid Earth*, 115(B3).
- Petrov, L. and Boy, J.-P. (2004). Study of the atmospheric pressure loading signal in very long baseline interferometry observations. *Journal of Geophysical Research: Solid Earth*, 109(B3).
- Remondi, B. W. (1985). Global positioning system carrier phase: description and use. *Bulletin géodésique*, 59(4):361–377.
- Rosen, P. A., Hensley, S., Joughin, I. R., Li, F. K., Madsen, S. N., Rodriguez, E., and Goldstein, R. M. (2000). Synthetic aperture radar interferometry. *Proceedings of the IEEE*, 88(3):333–382.
- Rowlands, D., Luthcke, S., Klosko, S., Lemoine, F., Chinn, D., McCarthy, J., Cox, C., and Anderson, O. (2005). Resolving mass flux at high spatial and temporal resolution using grace intersatellite measurements. *Geophysical Research Letters*, 32(4).
- Rudenko, S., Otten, M., Visser, P., Scharroo, R., Schöne, T., and Esselborn, S. (2012). New improved orbit solutions for the ers-1 and ers-2 satellites. *Advances in Space Research*, 49(8):1229–1244.
- Schmid, R., Steigenberger, P., Gendt, G., Ge, M., and Rothacher, M. (2007). Generation of a consistent absolute phase-center correction model for gps receiver and satellite antennas. *Journal of Geodesy*, 81(12):781–798.
- Schrama, E. J. and Wouters, B. (2011). Revisiting greenland ice sheet mass loss observed by grace. *Journal of Geophysical Research: Solid Earth*, 116(B2).
- Seeber, G. (2003). *Satellite geodesy: foundations, methods, and applications*. Walter de Gruyter.

- Sella, G. F., Dixon, T. H., and Mao, A. (2002). Revel: A model for recent plate velocities from space geodesy. *Journal of Geophysical Research: Solid Earth (1978–2012)*, 107(B4):ETG–11.
- Steigenberger, P., Rothacher, M., Dietrich, R., Fritsche, M., Rülke, A., and Vey, S. (2006). Reprocessing of a global gps network. *Journal of Geophysical Research: Solid Earth*, 111(B5).
- Swenson, S. and Wahr, J. (2006). Post-processing removal of correlated errors in grace data. *Geophysical Research Letters*, 33(8).
- Tapley, B. D., Bettadpur, S., Ries, J. C., Thompson, P. F., and Watkins, M. M. (2004). Grace measurements of mass variability in the earth system. *Science*, 305(5683):503–505.
- Thomas, I. D., King, M. A., Bentley, M. J., Whitehouse, P. L., Penna, N. T., Williams, S. D., Riva, R. E., Lavallee, D. A., Clarke, P. J., King, E. C., et al. (2011). Widespread low rates of antarctic glacial isostatic adjustment revealed by gps observations. *Geophysical Research Letters*, 38(22).
- Velicogna, I. and Wahr, J. (2006). Acceleration of greenland ice mass loss in spring 2004. *Nature*, 443(7109):329–331.
- Wahr, J., Molenaar, M., and Bryan, F. (1998). Time variability of the earth’s gravity field: Hydrological and oceanic effects and their possible detection using grace. *Journal of Geophysical Research: Solid Earth (1978–2012)*, 103(B12):30205–30229.
- Wahr, J., Swenson, S., Zlotnicki, V., and Velicogna, I. (2004). Time-variable gravity from grace: First results. *Geophysical Research Letters*, 31(11).
- Williams, S., Bock, Y., and Fang, P. (1998). Integrated satellite interferometry: Tropospheric noise, gps estimates and implications for interferometric synthetic aperture radar products. *Journal of Geophysical Research: Solid Earth (1978–2012)*, 103(B11):27051–27067.

Wouters, B., Bonin, J., Chambers, D., Riva, R., Sasgen, I., and Wahr, J. (2014). Grace, time-varying gravity, earth system dynamics and climate change. *Reports on Progress in Physics*, 77(11):116801.

Yoon, Y. T., Eineder, M., Yague-Martinez, N., and Montenbruck, O. (2009). Terrasar-x precise trajectory estimation and quality assessment. *Geoscience and Remote Sensing, IEEE Transactions on*, 47(6):1859–1868.

Zebker, H. A. and Lu, Y. (1998). Phase unwrapping algorithms for radar interferometry: residue-cut, least-squares, and synthesis algorithms. *JOSA A*, 15(3):586–598.

Zebker, H. A., Rosen, P. A., and Hensley, S. (1997). Atmospheric effects in interferometric synthetic aperture radar surface deformation and topographic maps. *Journal of Geophysical Research: Solid Earth*, 102(B4):7547–7563.

Zumberge, J., Heflin, M., Jefferson, D., Watkins, M., and Webb, F. H. (1997). Precise point positioning for the efficient and robust analysis of gps data from large networks. *Journal of Geophysical Research: Solid Earth*, 102(B3):5005–5017.

Table 2.1: GPS satellite signals (bps = bits per second) (Seeber, 2003)

Atomic clock fundamental frequency	10.23 MHz
L1 frequency	1575.42 MHz
L1 wavelength	19.0 cm
L2 frequency	1227.60 MHz
L2 wavelength	24.4 cm
P-code frequency	10.23 MHz
P-code wavelength	29.31 m
P-code period	266 days
C/A-code frequency	1.023 MHz
C/A-code wavelength	293.1 m
C/A-code period	1 millisecond
data signal frequency	50 bps
data signal cycle length	30 seconds

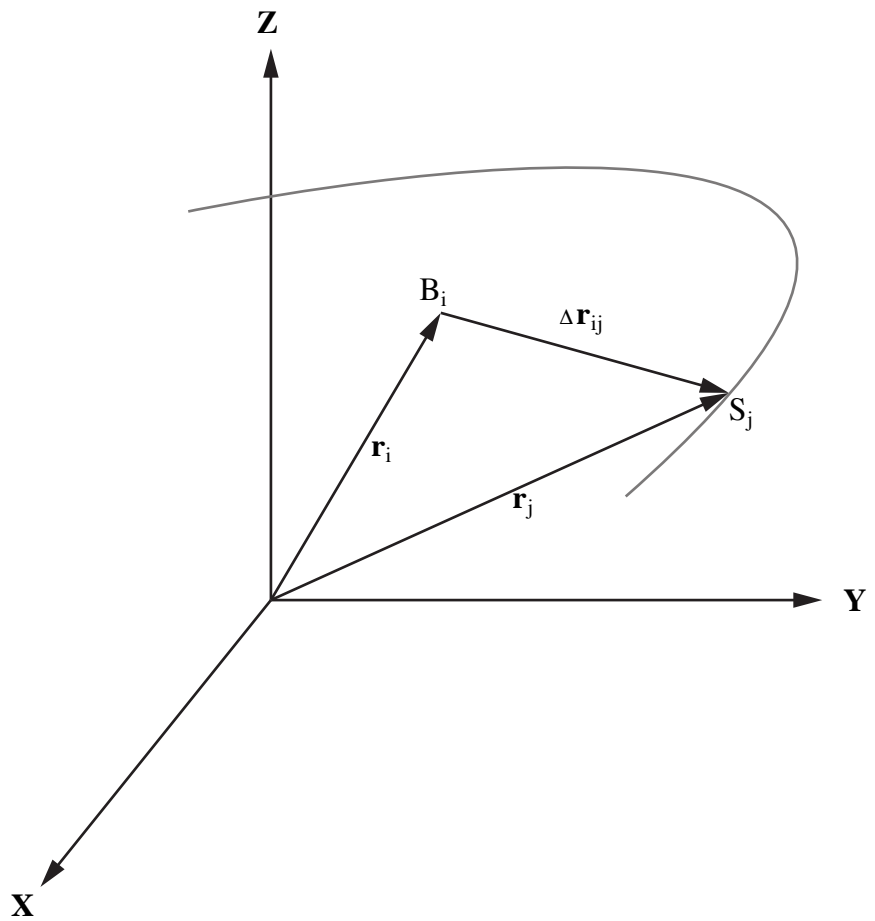


Figure 2.1: Basic relations for satellite observations (Figure 4.1 in Seeber (2003)). B represents the receiver and S represents the satellite.

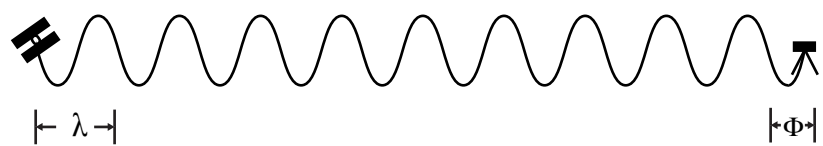


Figure 2.2: Carrier phase ranging.

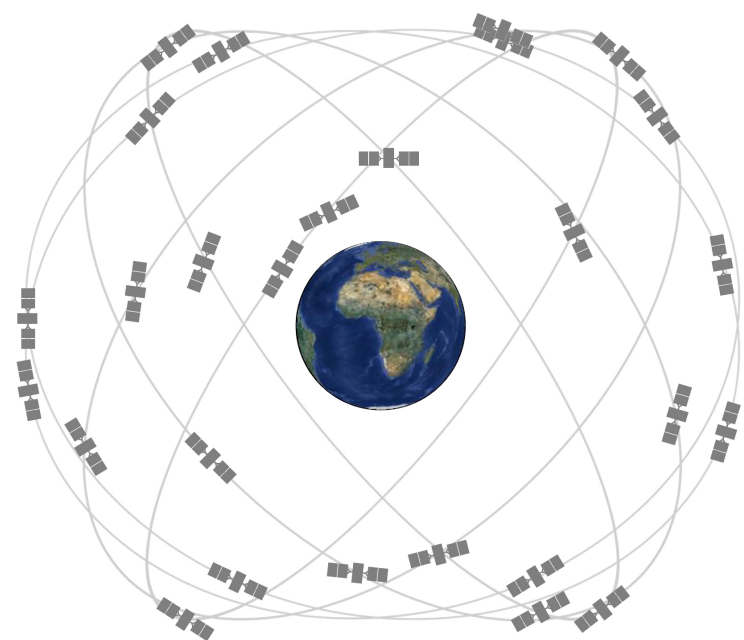


Figure 2.3: GPS satellite constellation (source: <http://www.gps.gov/systems/gps/space/>).

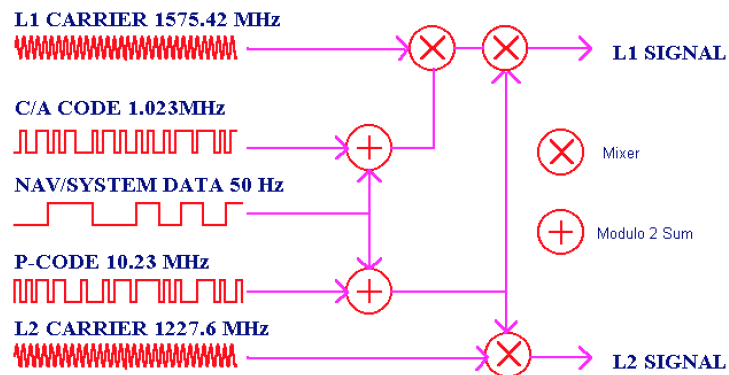


Figure 2.4: Composition of the signals from GPS satellites (source: <http://www.colorado.edu/geography/gcraft/notes/gps/gps.html>).

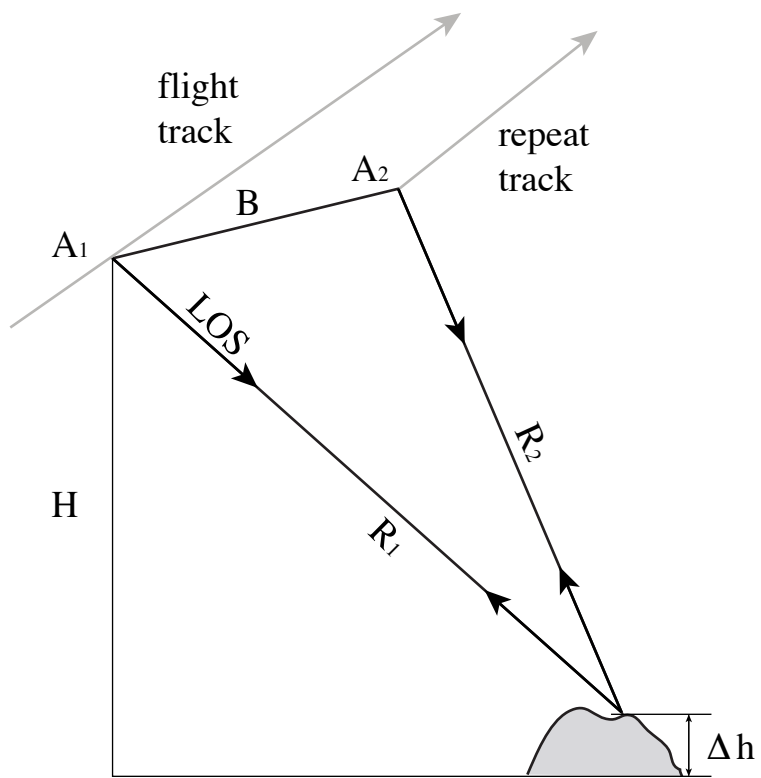


Figure 2.5: Acquisition geometry of repeat-track interferometry. A_1 and A_2 are the antenna positions at the initial acquisition and second acquisition; R_1 and R_2 are the ranges from antenna A_1 and A_2 to the ground target; H is the flight height; B is the baseline; LOS is the line of sight of the radar beam; Δh is the elevation of the ground target.

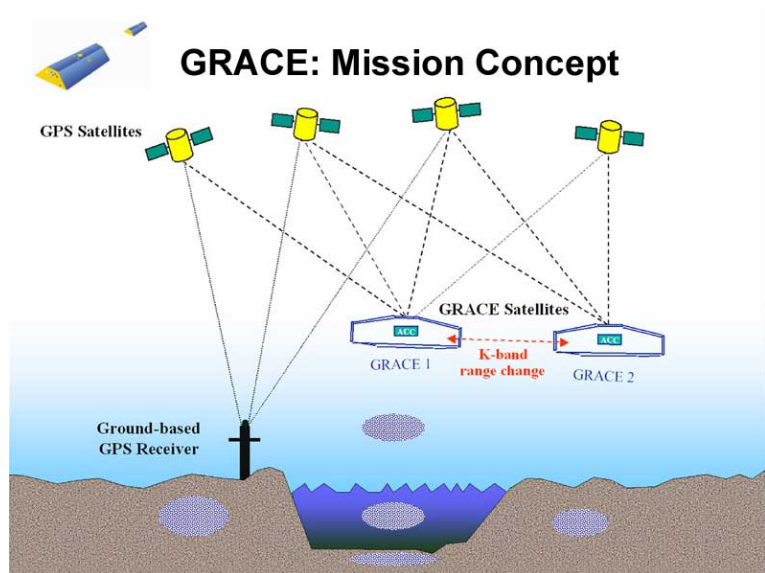


Figure 2.6: Basic mission concept of GRACE (source: <http://www.csr.utexas.edu/grace/publications/presentations/HPC2001.html>).

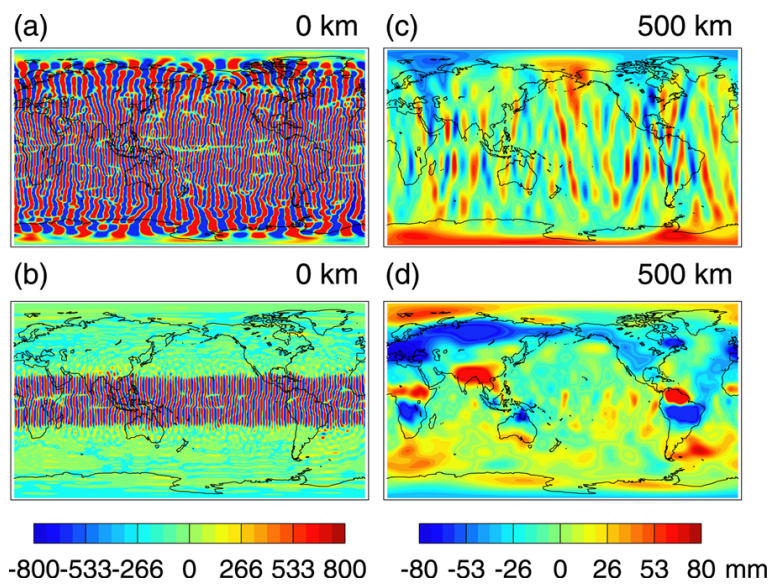


Figure 2.7: GRACE-derived maps of monthly anomaly of water storage. (a) Unsmoothed, no smoothing (b) filtered with correlated-error filter, no smoothing; (c) unfiltered and smoothed with 500 km Gaussian; (d) filtered with correlated-error filter and smoothed with 500 km Gaussian (Figure 3 in Swenson and Wahr (2006)).

3. Annual Variation of Coastal Uplift in Greenland as an Indicator of Variable and Accelerating Ice Mass Loss¹

3.1 Abstract

Seasonal melting of the coastal part of the Greenland ice sheet is investigated using GPS vertical displacement data from coastal stations, combined with data on atmospheric and ocean temperatures. Using a high pass filter and cubic spline models, we estimate five variables describing seasonal uplift, a proxy for proximal mass loss, including duration of the melt season and the amount of summer uplift. Our analysis shows both temporal and spatial variations of uplift. Southern coastal Greenland experienced anomalously large uplift in summer 2010, implying significant melting that year. However, the northwest coast did not experience significant change in uplift at that time. Our data suggest that a combination of warm summer air temperature and warm sub-surface ocean water temperature drove the large mass losses in 2010. Using the uplift pattern of 2008–2010, and comparing to atmospheric data and ocean water temperature data, we show that warm Irminger Water (IW) exerted significant influence on coastal melting in southeastern, southern and southwestern Greenland, reaching about 69 °N in 2010. North of this, IW did not exert significant influence, in effect defining the northward limit of the sub-polar gyre for that year. Thus, short-term variability in the coastal GPS uplift signal can be used to infer an oceanographic parameter that has a critical influence on Greenland ice sheet health.

3.2 Introduction

Significant mass loss of the Greenland ice sheet has been revealed in the last decade by the GRACE gravity mission (Velicogna and Wahr, 2006; Velicogna, 2009;

¹This chapter has been reprinted from *Geochemistry Geophysics Geosystems* with permission as: Yang, Q., Wdowinski S., Dixon, T. H., (2013), Annual variation of coastal uplift in Greenland as an indicator of variable and accelerating ice mass loss, *Geochem. Geophys. Geosyst.*, 14, 1569–1589. Copyright 2013 by Wiley. doi:10.1002/ggge.20089.

Chen et al., 2006; Luthcke et al., 2006; van den Broeke et al., 2009; Jacob et al., 2012), satellite altimetry (Krabill et al., 2004; Zwally et al., 2005; Thomas et al., 2006), mass accumulation/loss estimates (Hanna et al., 2005; Rignot and Kanagaratnam, 2006; Rignot et al., 2008), and GPS observations of coastal uplift (Jiang et al., 2010; Khan et al., 2010; Bevis et al., 2012). Recent studies detect considerable spatial and temporal variability of ice sheet mass change: prior to the 2010 melt season, mass loss appeared to be accelerating along the northwest coast, but slowing down in southeast Greenland since 2007 (Khan et al., 2010; Murray et al., 2010; Chen et al., 2011). Subsequently, Box et al. (2010) reported anomalously high air temperatures and melting in summer 2010 for much of coastal Greenland.

Coastal uplift is a useful proxy for coastal mass loss and perhaps overall Greenland ice mass balance. Previous studies have demonstrated that accumulation and loss in the interior of Greenland are in approximate balance, while recent net losses are focused in marginal coastal areas (e.g., Zwally et al., 2005; Thomas et al., 2006; Luthcke et al., 2006; Rignot and Kanagaratnam, 2006; Wouters et al., 2008). These coastal losses result in significant coastal uplift, reflecting the short-term, elastic response of the crust to mass unloading, and are readily measured by high precision GPS (Jiang et al., 2010; Khan et al., 2010; Bevis et al., 2012). Our previous study focused on decadal scale trends and demonstrated that decadal time series of the vertical position component were surprisingly well fit by a simple model of constant acceleration, with values for some Greenland stations, up to the end of the 2008 melt season, approaching 1mm yr^{-2} (Jiang et al., 2010). More recent measurements suggest that this trend of accelerating melting and uplift is continuing, at least at some locations, with the 2010 melt season recording the largest uplift since measurements began at many localities (Bevis et al., 2012).

Jiang et al. (2010) also suggested that there was useful information in the annual variation of coastal uplift. In Greenland, ice mass change is regulated by two climate factors, atmospheric forcing (Zwally et al., 2002; Hall et al., 2008) and oceanic forcing (Van de Wal et al., 2008; Holland et al., 2008; Hanna et al., 2009; Straneo et al., 2010, 2012; Seale et al., 2011). Atmospheric forcing can affect surface mass balance (SMB)

by changing either or both the snow accumulation rate and the ablation rate. Also, melt water can influence the basal sliding rate. Oceanic forcing can increase submarine melting of marine-terminating outlet glaciers, resulting in rapid changes in calving rate, and inducing dynamic changes upstream, including glacier acceleration and thinning. For both atmospheric and oceanic forcing, most melting occurs during the warm summer months and at low elevations near the coast. Nevertheless, it may be possible to use the summer uplift signal to separate the various effects and elucidate controls on mass loss. In this paper, we focus on seasonal uplift patterns in GPS data by using a high pass filter and cubic spline fit to the vertical position time series. We investigate regional and temporal changes in annual uplift and, by implication, coastal melting, and attempt to separate the relative roles of oceanic versus atmospheric forcing.

3.3 Methods

3.3.1 GPS Data and Processing

We analyzed all publicly available GPS data up to May 2011. Data from 18 continuous or semicontinuous GPS sites in the coastal region of Greenland are now available with at least 3 years of data, through the establishment of a remarkable network of reliable, high precision instruments (Bevis et al., 2012) (Figure 3.1). We use the GIPSY-OASIS 5.0 software (Zumberge et al., 1997) to process these data. Orbit parameters and clock products are provided by Jet Propulsion Laboratory (<ftp://sideshow.jpl.nasa.gov/>). We use the Global Mapping Function (Böhm et al., 2006) to relate the atmospheric wet delay to elevation angle. An ocean tidal loading correction is applied to all sites by using model FES2004 (Letellier, 2005). We first generate daily precise point position solutions for each station. We then adopt the Ambizap algorithm (Blewitt, 2008) to solve integer ambiguities for each station. The final ambiguity fixed daily solutions are then aligned to the IGS05 reference frame (Altamimi et al., 2007). Errors associated with GPS reference frame instability are probably negligible for the short-term (2008–2010) comparisons that are the main focus of our study, although they could affect longer-term (decadal) time series.

To isolate the effect of ice load variation from seasonal atmosphere loading, we apply an air pressure loading correction. We subtract precomputed Atmospheric Loading Displacements (<http://gemini.gsfc.nasa.gov/aplo/>) (Petrov and Boy, 2004) from the GPS vertical displacement time series. Details of this procedure are described in the supporting information section.

We also considered the possibility of local snow loading as a source of annual uplift variability. Calculations suggest that the deformation caused by local snow load is less than 1mm at most of our study sites (supporting information), so we have ignored this effect.

3.3.2 Seasonal Uplift Analysis

Jiang et al. (2010) assumed constant amplitude of annual uplift each year, a common assumption in GPS time series analysis. However, the data show significant annual variation, and it is this variation that we seek to quantify. Variable amplitude in the seasonal signal has been addressed in several ways (Murray and Segall, 2005; Davis et al., 2006; Bennett, 2008; Davis et al., 2012). In this paper, we first use a high pass filter to isolate the seasonal signal by removing the secular component from the GPS time series. We then fit the residual GPS time series with a smoothing cubic spline. Based on the spline model estimate (red solid line in Figure 3.2), we derive five variables that relate to mass loss: the timing (start and end time) and duration of summer melt season, the total amount of seasonal uplift (which relates to the total mass loss, including surface and sub-surface melting, runoff, calving, and dynamic thinning) for the local basin, and the rate of summer uplift (Figure 3.2). We chose a cubic spline model because it is straightforward to apply and can identify the minima and maxima for each year without any assumptions concerning specific periodicity, which may vary from year to year.

A key parameter in the cubic spline model is the smoothing, S . As the value of S increases, misfit decreases, but the “roughness” (complexity) of the model increases; at some point, more than one maxima and minima per year can result, which is generally unrealistic. Thus, there is a trade-off between goodness of fit and smoothing. A sensitivity study using various values of S allows us to define an optimum value by requiring a

single crest and a single trough per year. The optimum smoothing parameter differs somewhat for each site because of variations in data quality and length of time series. We chose a compromise value ($S=0.91$) and applied it to all sites to ensure that relative variations in estimated parameters can be compared across all the time series and regions in a consistent way. This value generates single minima and single maxima per year for 16 out of 18 sites. For sites THU3 and QAQ1, the analysis yields double peaks in 2007 and 2008, respectively, although one is smaller than the other. For these two sites, we remove the smaller crest and trough, using the larger one to estimate the five parameters of interest. These sites are marked with an asterisk in Table 3.1. Note that the seasonal uplift estimated in this way is somewhat conservative, especially for years with significantly different uplift compared to earlier years. This reflects the fact that our technique tends to damps extreme excursions, with the effect increasing as the degree of smoothing increases. All time series and their spline model fits are shown in the supporting information.

Uncertainties for the parameter estimates are determined with a Monte Carlo approach. We report the mean value of a large number of estimates as the best estimate, with uncertainty defined at the one-sigma confidence level based on the bounds containing 68% of the estimated values. Details of this procedure are described in the supporting information section.

3.3.3 Surface Air Temperature Data and Analysis

We obtained daily surface air temperature data from 11 meteorological stations in coastal Greenland provided by the Danish Meteorological Institute (Carstensen and Jørgensen, 2011). All the stations are synoptic and observe surface air temperature and other weather parameters at 3 h intervals. We select the meteorological sites that have a similar time span to the GPS data and are closest to the GPS site of interest (Figure 3.1). Information describing these meteorological stations and respective nearby GPS stations are listed in Table A2. The time span for available meteorological records near KULU and KELY is 2000–2010; for QAQ1 and THU3, it is 2003 – 2010; for other GPS stations, it is 2008–2010. In order to compare air temperature with annual uplift variability, we

calculate the Annual Mean Surface Air Temperature (AMSAT) and Cumulative Annual Positive Degree Days (CAPDD) per year for each meteorological station. CAPDD may be a better indicator of seasonal, atmospheric-forced melting than AMSAT; on the other hand, AMSAT is a simple indicator of overall climate warming. It is also useful to compare AMSAT with annual mean ocean temperature, discussed later.

3.3.4 SMB

SMB is the difference between net snow accumulation and net runoff of surface meltwater. Since coastal uplift recorded by GPS is caused by both nearby SMB changes and ice dynamic changes (mainly calving and associated thinning), comparison of the GPS results to SMB changes provides an alternate way to assess atmospheric versus oceanic forcing. We use SMB derived from Regional Atmospheric Climate Model v.2 (RACMO2) (Ettema et al., 2009, 2010a,b; Kuipers Munneke et al., 2011; Van Angelen et al., 2012) and calculate SMB in the summertime (June to August) in each year during 2000–2010.

3.3.5 Sub-surface Ocean Temperature Data and Analysis

Sub-surface water temperature is obtained from the Hadley Center EN3 model output (<http://www.metoffice.gov.uk/hadobs/en3/>). The EN3 model consists of two products: (1) in-situ sub-surface ocean temperature and salinity profiles with data quality information; and (2) objective analyses using optimal interpolation of the in-situ data profiles with a quality control system (Ingleby and Huddlestone, 2007). In this paper, we use the objective analyses product, which contains monthly temperature estimates from 1950 to the present with a spatial resolution of $1^\circ \times 1^\circ$ (about 111 km (N-S) by 38 km (E-W) at 70° north, neat central Greenland) and 42 depth intervals (5m to 5350 m). Due to the presence of a broad continental shelf, water depth along most of Greenland’s coast is limited, which in turn limits the influence of deep water. We looked at data in the EN3 model from 5m to 447m depth (depth levels 1 to 22), selecting 14 “voxels” (model volume elements) that are close to our GPS stations (Figure 3.1). To compare sub-surface water temperature with annual uplift and atmospheric mean temperature, we calculate

the Annual Mean Sub-Surface Water Temperature (AMSSWT) averaged over this upper 442m of ocean depth range. The deeper parts of this water volume will not necessarily interact with all outlet glaciers due to topographic barriers near a given fjord entrance (usually endmoraines from the Last Glacial Maximum at about 22 ka) and circulation complexities. We have not accounted for such local effects in our analysis.

3.4 Results

3.4.1 Seasonal Uplift/Subsidence Pattern

Figure 3.3 and Table 3.1 show the five parameters estimated from the GPS time series for the four time series that exceed 5 years (QAQ1, KULU, KELY, and THU3). For KULU, data in the early part of 2008 is missing; thus, the estimate of start time in 2008, end time in 2007, and duration and uplift both in 2007 and 2008 are less reliable.

The distance between a given GPS site and the locus of nearby mass loss will affect the magnitude of observed uplift. For example, site HEL2 is located very close (less than 5 km) to the terminal region of Helheim, a large outlet glacier in southeast Greenland, and experienced 19mm uplift in the summer of 2010, one of the largest values observed in our study. We estimated distance to the nearest glacier front for the various stations (Table 3.2) but note that in some cases, the distance is ambiguous, since more than one nearby outlet glacier may be influencing measured uplift. For this reason, direct comparison of uplift magnitude may not be useful. However, a comparison of year-to-year changes for a given site will be useful because over short (several year) time scales, because the distance change effects are small. For longer (decadal scale and longer) periods, this could become an issue at locations with rapidly retreating ice margins unless sites can be periodically relocated.

In 2010, the beginning of the uplift season for QAQ1, KULU, and KELY was much earlier than previous years (QAQ1: 25 days earlier than the 2003–2009 average; KELY: 34 days earlier than the 1997 – 2009 average; KULU: 59 days earlier than the 2000 – 2009 average). Note that when calculating these average values, we do not include parameter estimates with significant uncertainties. For example, the anomalous negative duration with large uncertainty for KULU at 2007 is ignored in KULU’s average.

In contrast to QAQ1, KULU, and KELY, site THU3 began uplifting 23 days later than the 2003 – 2009 average. For KELY, the end of the uplift season was 14 days later in 2010 (KULU: 13 days later than the 2003–2009 average; KELY: 14 days later than the 1997 – 2009 average). For QAQ1, uplift ended in 2010 about the same day as the previous mean value. However, for KULU and THU3, uplift ended earlier in 2010 (KULU: 13 days earlier; THU3: 49 days earlier). Hence, for QAQ, KULU, and KELY, the duration of summer uplift (and presumably melting) was somewhat longer in 2010 (QAQ1: 23 days; KULU: 46 days; KELY: 48 days) than the average of previous years. For THU3, the duration is about 46 days shorter than the average.

The amount of uplift in 2010 for three sites (QAQ1, KULU, and KELY) in south Greenland exceeded 10mm and was larger than in the previous years, implying an increase of ice mass loss in 2010 at these locations, which agrees well with the positive 2010 uplift anomaly in south Greenland observed by Bevis et al. (2012). No significant change in uplift occurred at northwest site THU3 in 2010. Our analysis differs slightly from that of Bevis et al. (2012) who report a negative 2010 uplift anomaly in northwest Greenland; our data suggest 2010 uplift at site THU3 is about the same level as the previous year (Figures 3 and 5). In agreement with recent GRACE results (Schrama and Wouters, 2011; Chen et al., 2011; Khan et al., 2010), our data show decreased uplift for sites KULU and QAQ1 in south Greenland in 2007 and increased uplift for site THU3 in northwest Greenland from 2007 to 2009. Uplift correlated strongly ($R \geq 0.5$, where R is the correlation coefficient) and significantly ($P \leq 0.05$, where P is the significance probability) with duration for sites in southern coastal Greenland, indicating that the length of summer melting influences the amount of summer melting in that area (Figure 3.4). In addition, the speed of summer uplift in 2010 for most sites was significantly faster than previous years, implying more intense summer melting. From these observations, we can infer that for most of southern coastal Greenland, the anomalously high melting in 2010 reflected both a longer duration melting season and more intense melting.

We also analyzed data from 14 sites with shorter time spans, May 2008 to May 2011, covering the 2008, 2009, and 2010 melt seasons (Figure 3.5). For most sites in

southern Greenland, the largest uplift occurred in 2010, followed by 2008, with 2009 having the smallest uplift. However, sites in northern Greenland (KULL, DKSG, THU3, and MARG) did not experience significant uplift variation from 2008 to 2010, perhaps indicating less sensitivity to short-term variations in forcing. Uplift in 2009 was somewhat higher than the other 2 years for most sites in northern Greenland. On average, the annual uplift in southern Greenland is higher than that in northern Greenland, especially in 2010.

3.4.2 Air Temperature Analysis

Figure 6 shows time series of the two atmospheric parameters for the four meteorological stations closest to QAQ1, KULU, KELY, and THU3, the sites with the longest GPS time series. 2010 AMSAT at KELY was nearly 4 °C above the 2000 – 2009 mean. For QAQ1, THU3, and KULU, the differences between the 2010 AMSAT and the means of their base periods are 2.8 °C, 2.0 °C, and 1.0 °C, respectively (Table 3.1 and Figure 3.6a). CAPDD provides an index of surface melting duration, for comparison with the duration of uplift. In 2010, all four sites experienced a longer CAPDD compared to previous years, although the difference was small at THU3 in northwest Greenland (Table 3.1 and Figure 3.6b). For QAQ1, there was a dramatic increase in CAPDD for 2010 compared to earlier years. We also observe the expected latitudinal pattern in both atmospheric indices, with southern sites experiencing higher AMSAT and longer CAPDD compared to northern sites.

3.4.3 Comparison to SMB

We compare our GPS observation to SMB derived from RACMO2 (Ettema et al., 2009, 2010a,b). Figure 3.8 shows the difference between Greenland ice sheet SMB in the summertime (June to August) of 2010 and individual years of the previous decade. SMB in summer 2010 was more negative than previous years in Greenland’s southern coastal areas, indicating significant surface mass loss at that time. However, the pattern in northwest Greenland is somewhat different. While coastal SMB was negative in both 2009 and 2010 (significant summer melting), it was somewhat less negative in 2010, so that the difference (2010–2009) is slightly positive (Figure 3.7). GRACE data actually

suggests slight mass gains in the interior (Bevis et al., 2012). We see seasonal uplift at all northwest Greenland sites (Figure 3.5) while at site THU3, summer 2010 uplift is both high (Figure 3.3c) and intense (i.e., high rate, Figure 3.3d), which does not reconcile with the SMB model. Perhaps, oceanic forcing or dynamical changes (thinning from longer-term climate trends) are responsible for some of the coastal mass loss here, by definition not part of the SMB model, and not sensed by the lower spatial resolution of GRACE. These possibilities are discussed in more detail below.

3.4.4 Sub-surface Ocean Temperature Analysis

Figure 3.8 shows the differences between AMSSWT in 2010 and previous years (2000 to 2009) for Greenland’s coastal areas. Sub-surface ocean temperature in 2010 is significantly higher than previous years near both southeast and southwest Greenland. However, northwest Greenland in 2010 does not experience this temperature anomaly. Figure 3.9 shows time series of AMSSWT obtained from voxels near respective GPS stations for the period 2000–2010. As in Figure 3.8, high temperature was observed in 2010 compared with the previous decade. In addition, the spatial variations of AMSSWT can be clearly seen: AMSSWT reaches its maximum in southeast Greenland and decreases to southwest Greenland, further decreasing in northwest Greenland.

3.4.5 Correlation Analysis

We now investigate a series of correlations between uplift and atmospheric or oceanic parameters, in particular looking for short-term (several year) linear relations between forcing and response. Since glacier dynamics (a possible influence on coastal mass loss and uplift) can be highly non-linear, with response times exceeding decades, we may be able to infer its influence indirectly by investigating conditions where correlations between the simple forcing functions described here (atmospheric or ocean temperature) are not observed.

3.4.5.1 Uplift and Atmospheric Factors

To investigate the possible relationship between air surface temperature and seasonal uplift pattern, we first look at data for sites with more than 5 years of GPS data. We looked at correlations between uplift and atmospheric parameters, with uplift weighted by its uncertainty. We assess a correlation to be good when the correlation is both strong (correlation coefficient $R>=0.5$) and significant ($P<=0.05$). Uplift duration and CAPDD are not well correlated (Figure 3.10), implying a role for ocean forcing for at least some sites. Figure 3.11 investigates correlations between the magnitude of annual uplift, AMSAT, and CAPDD. Both AMSAT and CAPDD show good correlation with seasonal uplift at KELY and QAQ1. However, uplift and the atmospheric parameters are not well correlated at THU3, and CAPDD is not well correlated with uplift at KULU.

We can use the larger GPS dataset to investigate possible relationships between seasonal uplift and AMSAT and CAPDD for the years 2008 – 2010 by looking at the pattern of variation (Figure 3.12). Poor agreement between uplift and the two atmospheric parameters is observed at most sites, except for KELY. Moderate agreements between uplift and either AMSAT or CAPDD are observed for QAQ1, KAGA, SRMP, and RINK.

The larger GPS dataset can also be used to investigate possible temporal variations in the relationship between seasonal uplift and AMSAT, CAPDD for 2008–2010 (Figure 3.13). 2010 uplift shows stronger correlations with both local AMSAT and CAPDD compared to previous years. 2009 exhibits especially poor correlation between uplift and the local atmospheric parameters.

3.4.5.2 Uplift and Ocean Warming

As with the correlation analysis between seasonal uplift and atmospheric parameters, we first look at the correlation between seasonal uplift and AMSSWT for sites with more than 5 years of GPS data (Figure 3.11c). Seasonal uplift and AMSSWT are well correlated only for KELY over this longer time period. Strong negative correlation between uplift and AMSSWT is observed at THU3. However, when we look at the larger GPS data set for shorter 2008 – 2010 period (Figure 3.12), a different pattern emerges. Sea-

sonal uplift has a pattern similar to AMSSWT for most sites in southern Greenland. For example, compare the uplift pattern to AMSSWT for these 3 years at the seven adjacent sites TIMM, HJOR, TREO, LYNS, HEL2, KSNB, and PLPK in southeast Greenland (Figure 3.12). The temporal variation in uplift closely matches trends in the ocean parameter (AMSSWT) but is only in moderate agreement with the atmospheric parameters (AMSAT and CAPDD). However, this pattern breaks down for sites in northwest Greenland (Figure 3.12). Figure 3.13 suggests that 2010 uplift is somewhat better correlated with AMSSWT than CAPDD, although the differences are small. Nevertheless, these results suggest an important role for oceanic forcing in the 2010 melt anomaly, especially for southern sites. As with the atmospheric parameters, uplift correlates poorly with AMSSWT in 2009, when uplift is small at many sites (Figure 3.5).

3.4.6 Uplift Acceleration

The spatial gradients for air and sub-surface water temperature differ: surface air temperature decreases from south to north, while sub-surface water temperature decreases clockwise around Greenland from southeast to northwest, following the path of the Irminger Current (IC) (Figures 6 and 9). Hence, it may be possible to estimate the relative influence of air and ocean forcing on the 2010 uplift anomaly by looking at spatial variations in the short-term changes (acceleration) of uplift.

Acceleration of vertical crustal motion was estimated from the GPS time series by fitting a constant acceleration model, following Jiang et al. (2010). Here, we focus on two time scales, the mid-2007 to early 2011 period for all available stations, and the decadal (or longer) time series available for four stations.

Figure 3.14 compares the uplift acceleration of 17 GPS sites (between mid-2007 and early 2011) and both atmospheric and oceanic parameters in 2010. Although there are relatively good correlations between acceleration and two atmospheric parameters (AMSAT and CAPDD), the strongest correlation is with AMSSWT. Also, the largest acceleration occurs at site PLPK in southeast Greenland rather than the southernmost site QAQ1. QAQ1 had the highest temperature and longest CAPDD in 2010, yet did not experience the largest uplift anomaly in that year. This suggests that atmospheric

temperature is not the dominant factor causing the difference in accelerations. Site PLPK is located close to where the IC first approaches the coast of Greenland (Figure 3.1). Hence, the observed uplift acceleration in 2010 may reflect the influence of warm Irminger Water (IW), through its melting of sub-surface ice in marine-terminating glaciers (Holland et al., 2008; Straneo et al., 2010, 2012).

During the period mid-2007 to early 2011, all sites in south and central Greenland show positive accelerations, with the highest accelerations recorded at sites in southeast Greenland. In contrast, sites in northwest Greenland show negative acceleration (Figure 3.14 and Table 3.3a). This marks a significant change from our earlier study (Jiang et al., 2010) which showed accelerating uplift in northwest Greenland up until 2008. Comparing with the result of Jiang et al. (2010), our data show higher accelerations for sites in south Greenland until May 2011, reflecting the enhanced 2010 uplift. Figure 3.15 shows the relative difference between uplift in 2010 compared to 2008 and 2009. Over this period, uplift (and presumably mass loss) increases in southern Greenland, but decreases or is essentially unchanged in northwest Greenland.

3.4.7 Comparison to GRACE

Our GPS data are in agreement with GRACE observations showing significant anomalous mass loss in southern Greenland in 2010, as observed by Bevis et al. (2012). However, we do not observe mass gain in northern Greenland suggested by the GRACE observations. As pointed out by Bevis et al. (2012), this difference likely reflects the spatial resolution of GRACE, giving this sensor sensitivity to mass gain in the interior of Greenland (to which coastal GPS would not be sensitive) and perhaps sensitivity to mass changes on the other side of Baffin Bay (Devon, Ellesmere Islands).

It is also useful to compare our GPS results with GRACE over various time spans. Accelerations of the four GPS time series with longer time spans are shown in Table 3.3b. From 2007 to 2009, ice loss slowed down in the southeast and sped up in the northwest (Schrama and Wouters, 2011; Chen et al., 2011; Khan et al., 2010), while the new GPS data detected acceleration beginning again in the south Greenland with the intense 2010 melt season. Thus, the positive accelerations in southeast Greenland and negative or zero

accelerations in northwest Greenland between middle 2007 and early 2011 are dominated by variations of mass loss in the summer of 2010.

In terms of annual variations, Wouters et al. (2008) detected large mass loss along the coasts of southeastern and northwestern Greenland in the summers of 2003, 2005, and 2007. Our data show high uplift at northwest and southeast GPS site in 2003 and 2005 but not in 2007. The different spatial scales of GPS and GRACE could cause this difference.

3.5 Discussion

Seasonal uplift in coastal Greenland, as measured by high precision GPS and our cubic spline time series model, shows considerable site-to-site and year-to-year variation, which we believe correlates with variations in the mass loss of nearby outlet glaciers. This provides a useful tool for investigating the conditions of melting, and overall mass balance in Greenland, since most ice melting is concentrated in low elevation coastal ablation zones. The coastal “necklace” of high precision GPS stations emplaced and maintained by various geodetic institutions (Bevis et al., 2012) thus provides an important tool for monitoring the health of the Greenland ice sheet.

The role of warm sub-surface water in accelerating melting of marine-terminating glaciers was noted in Alaska (Motyka et al., 2003) and Antarctica (Payne et al., 2004; Shepherd et al., 2004). Warming ocean currents have been implicated in Greenland’s accelerating mass loss since the late 1990s, through increased submarine melting, increased calving, and related dynamic effects (Myers et al., 2007; Holland et al., 2008; Straneo et al., 2010, 2012; Seale et al., 2011; Joughin et al., 2012). Amundson et al. (2010) pointed out that melting of the mélange in front of a calving glacier would reduce flow resistance for inland ice. Motyka et al. (2011) proposed that basal melting of a floating ice tongue would also increase calving and acceleration of inland ice. The warmest water found along the Greenland margin is fed by the IC, a branch of the North Atlantic Current, ultimately sourced from the Gulf Stream. The IC carries warm and saline subtropical water into subpolar basins and forms a key part of the subpolar gyre. As it approaches the Greenland coast, it meets cold, fresh polar melt water coast that is

lower in density, flowing south along the Greenland coast. At this point, the IC becomes a sub-surface current. The depth range of the IC is variable, but it typically occupies the depth range 100m – 600m (e.g., Myers et al., 2007; Holland et al., 2008; Straneo et al., 2012). While cold, fresh polar water transported by the East and West Greenland Currents (EGC and WGC) is in direct contact with Greenland fjords (Figure 3.16), IW can nevertheless enter at the bottom of some glacier fjords, especially along the southeast and southwest coasts of Greenland, because it is more dense, reflecting its higher salinity.

Our GPS data clearly illustrate the spatial distribution of IW influence: from mid-2007 to early 2011, on average, uplift acceleration is maximum for stations in southeast Greenland, where the IC first advects heat to coastal Greenland and then decreases as the current flows clockwise around Greenland (Figures 14c and 16a). Presumably, the influence of warm IW decreases to the northwest because it becomes diluted by mixing with cold coastal waters and exchange with cold atmosphere.

There is a significant year-to-year variation in the amplitude of annual uplift in the southern coastal areas, with the variability decreasing to the north (Figures 5 and 12). The behavior of most sites in southeast and southwest Greenland closely follows the pattern of sub-surface ocean temperature variation between 2008 and 2010. In contrast, sites north of KAGA (69.2 °N) do not experience significant influence from warm IW during 2008 – 2010. Perhaps, the bathymetry of Davis Strait reduces IW influence north of that location. The bathymetry of Disco Bay, and the long, deep fjord of Jakobshavn Isbrae (near where KAGA is located) may also limit further northward penetration of warm water, by promoting mixing with cold surface waters. This is consistent with the oceanographic data of Straneo et al. (2012) showing only cold (< 3 °C) intermediate water north of this location and consistent with the Hadley EN3 model output (Figure 3.8).

Figure 3.16b shows mass loss in equivalent water height over Greenland between February 2003 and January 2008 observed by GRACE (Wouters et al., 2008). The location of maximum mass loss for this earlier period correlates with the point where the IC first turns towards Greenland, while mass loss decreases progressively northward

along the west coast, implying that this is a long-lived (at least on the decadal time scale) pattern. The northern limit of IW influence on melting in northwest coastal Greenland will be an important variable for future monitoring.

For the longer period of our observations, uplift and oceanic forcing are not well correlated (Figure 3.11c), suggesting nonlinearity between ice mass loss and oceanic forcing. One curious exception is KELY (Table 3.2 and Figure 3.11c). This site is located near a land-terminating glacier and exhibits good correlations between uplift and both CAPDD and AMSSWT, on both shorter (3 year) and longer (decadal) time scales (Figures 11 and 12). This station is located far from the coast (Figure 3.1 and Table 3.2), implying that mass loss should mainly be sensitive to atmospheric conditions. Its apparent correlation with offshore intermediate water temperature is puzzling.

THU3, although located near marine-terminating glaciers, exhibits negative correlation with sub-surface water temperature (Figure 3.11). Also, small seasonal uplift variations are observed for other sites in northwest Greenland (KULL, DKSG, and MARG), and correlations between uplift and atmospheric or ocean temperature are not observed for these sites (Figure 3.12). Both air and water temperatures at these high latitudes are so low for most of the year that small fluctuations in these parameters may have little or no effect on summer melting. Perhaps longer-term ice dynamics plays an important role, e.g., ocean or atmosphere changes a decade ago or longer caused changes in the flow regime that are just now showing up. Pritchard et al. (2009) pointed out that unlike southeast Greenland, dynamic thinning in the northwest is caused by dynamic imbalance. This dynamic imbalance may be associated with changes of ice thickness and surface slope (Huybrechts and de Wolde, 1999) caused by past climate forcing and may be a major influence on current mass loss and coastal uplift at these northwest sites, with warm summer conditions playing a secondary role.

Using passive microwave data, Box et al. (2010) observed a longer duration melt season in 2010, with an earlier start (end of April) and later ending (mid September), compared to the 1997–2009 average value. Our data suggest longer melting season duration at some sites. However, the GPS uplift data also show anomalously fast uplift in

2010 (Figure 3.3d and Table 3.1), suggesting that ice melting proceeded not only by a lengthening of the melt season, but also by more intense summer melting. Anomalously warm atmospheric conditions in 2010 could be a contributing factor to intense summer melting, potentially increasing surface melt in the ablation zone (Zwally et al., 2002). Reduced albedo during the long melt season, with more days with exposed bare rock, may also have contributed to local mass loss (Tedesco et al., 2011).

Murray et al. (2010) showed that mass losses and speed of tidewater glaciers in southeast Greenland increased for 2003 – 2006 and then decreased for 2007–2008. Similarly, our GPS data show large uplift for 2003 – 2006 and small uplift for 2007 – 2008 at QAQ1 and KULU (Figure 3.3c). Murray et al. (2010) suggest that there is a negative feedback loop between calving and ocean temperature, as the icebergs eventually cool the water. This causes a 2 year lag between initial speed up and mass loss (caused by influx of warm water) and subsequent slow down and decreased mass loss (caused by cooling of fjord and coastal water). Such “predator–prey” feedback relations are observed in many natural systems (e.g., Walker et al., 1981; Douglass and Knox, 2005; Koren and Feingold, 2011). Future studies may be able to better examine such variations, since regional changes in short-term glacier response can now be studied in some detail using the techniques outlined here.

3.6 Conclusions

We describe a new technique for investigating spatial and temporal variations of crustal uplift along coastal Greenland, allowing us to study annual variations in ice melting on a basin scale. Our data show large magnitude uplift for most GPS sites in 2010, indicating significant ice mass loss in that year, with the largest accelerations in southeast Greenland, decreasing clockwise to the northwest, suggesting the influence of the warm IC. The pattern of relative uplift in 2008, 2009, and 2010 correlates with sub-surface ocean temperature until about 69 °N(near KAGA), indicating that warm IW is sufficiently diluted with colder water north of this latitude that it has negligible influence on melting of marine-terminating outlet glaciers north of this point, during this time period. Ocean forcing is the dominant factor in coastal melting south of this point

for both eastern and western Greenland. On the other hand, a few stations near land terminating glaciers also show large uplift, and by implication large mass losses in 2010. Thus, a combination of warm water and warm air contributed to the anomalously large ice mass loss in Greenland in 2010. Poor correlation between uplift and air temperature or ocean temperature at northwestern sites suggests that longer-term ice dynamics may be a significant controlling factor for ice mass change in northwestern Greenland.

3.7 Acknowledgements

We thank Michael Bevis at Ohio State University, Shfaqat Abbas Khan at the Technical University of Denmark, and other investigators of the Greenland GPS Network (GNET) for providing high quality GPS data. The GPS data used in this study are archived at UNAVCO and SOPAC. We thank the Danish Meteorological Institute for providing weather and climate data for Greenland for the period 1958–2010. We thank Michiel R. van den Broeke and Jan van Angelen at Utrecht University for providing us with the RACMO2 SMB model output, and Dr. Matt King and the other anonymous reviewer for helpful comments on this manuscript. This research was supported in part by a NASA grant to THD.

3.8 References

- Altamimi, Z., Collilieux, X., Legrand, J., Garayt, B., and Boucher, C. (2007). Itrf2005: A new release of the international terrestrial reference frame based on time series of station positions and earth orientation parameters. *Journal of Geophysical Research: Solid Earth (1978–2012)*, 112(B9).
- Amundson, J. M., Fahnestock, M., Truffer, M., Brown, J., Lüthi, M. P., and Motyka, R. J. (2010). Ice mélange dynamics and implications for terminus stability, jakobshavn isbræ, greenland. *Journal of Geophysical Research: Earth Surface (2003–2012)*, 115(F1).
- Bennett, R. A. (2008). Instantaneous deformation from continuous gps: Contributions from quasi-periodic loads. *Geophysical Journal International*, 174(3):1052–1064.
- Bevis, M., Wahr, J., Khan, S. A., Madsen, F. B., Brown, A., Willis, M., Kendrick, E., Knudsen, P., Box, J. E., van Dam, T., et al. (2012). Bedrock displacements in greenland manifest ice mass variations, climate cycles and climate change. *Proceedings of the National Academy of Sciences*, 109(30):11944–11948.
- Blewitt, G. (2008). Fixed point theorems of gps carrier phase ambiguity resolution and their application to massive network processing: Ambizap. *Journal of Geophysical Research: Solid Earth (1978–2012)*, 113(B12).
- Böhm, J., Niell, A., Tregoning, P., and Schuh, H. (2006). Global mapping function (gmf): A new empirical mapping function based on numerical weather model data. *Geophysical Research Letters*, 33(7).
- Box, J., Cappelen, J., Decker, D., Fettweis, X., Mote, T., Tedesco, M., and van de Wal, R. (2010). Greenland [in arctic report card 2010].
- Carstensen, L. and Jørgensen, B. (2011). Weather and climate data from greenland 1958-2010 danish meteorological institute. Technical report, Technical Report.
- Chen, J., Wilson, C., and Tapley, B. (2006). Satellite gravity measurements confirm accelerated melting of greenland ice sheet. *Science*, 313(5795):1958–1960.

Chen, J., Wilson, C., and Tapley, B. (2011). Interannual variability of greenland ice losses from satellite gravimetry. *Journal of Geophysical Research: Solid Earth (1978–2012)*, 116(B7).

Davis, J., Wernicke, B., Bisnath, S., Niemi, N., and Elósegui, P. (2006). Subcontinental-scale crustal velocity changes along the pacific–north america plate boundary. *Nature*, 441(7097):1131–1134.

Davis, J. L., Wernicke, B. P., and Tamisiea, M. E. (2012). On seasonal signals in geodetic time series. *Journal of Geophysical Research: Solid Earth (1978–2012)*, 117(B1).

Douglass, D. H. and Knox, R. S. (2005). Climate forcing by the volcanic eruption of mount pinatubo. *Geophysical Research Letters*, 32(5).

Ettema, J., Van den Broeke, M., Meijgaard, E. v., Van de Berg, W., Box, J., and Steffen, K. (2010a). Climate of the greenland ice sheet using a high-resolution climate model—part 1: Evaluation. *The Cryosphere*, 4(4):511–527.

Ettema, J., Van den Broeke, M., Van Meijgaard, E., and Van de Berg, W. (2010b). Climate of the greenland ice sheet using a high-resolution climate model-part 2: Near-surface climate and energy balance. *The Cryosphere*, 4(4):529.

Ettema, J., van den Broeke, M. R., van Meijgaard, E., van de Berg, W. J., Bamber, J. L., Box, J. E., and Bales, R. C. (2009). Higher surface mass balance of the greenland ice sheet revealed by high-resolution climate modeling. *Geophysical Research Letters*, 36(12).

Hall, D. K., Williams, R. S., Luthcke, S. B., and Digirolamo, N. E. (2008). Greenland ice sheet surface temperature, melt and mass loss: 2000–06. *Journal of Glaciology*, 54(184):81–93.

Hanna, E., Cappelen, J., Fettweis, X., Huybrechts, P., Luckman, A., and Ribergaard, M. (2009). Hydrologic response of the greenland ice sheet: the role of oceanographic warming. *Hydrological Processes*, 23(1):7–30.

- Hanna, E., Huybrechts, P., Janssens, I., Cappelen, J., Steffen, K., and Stephens, A. (2005). Runoff and mass balance of the greenland ice sheet: 1958–2003. *Journal of Geophysical Research: Atmospheres (1984–2012)*, 110(D13).
- Holland, D. M., Thomas, R. H., De Young, B., Ribergaard, M. H., and Lyberth, B. (2008). Acceleration of jakobshavn isbrae triggered by warm subsurface ocean waters. *Nature Geoscience*, 1(10):659–664.
- Huybrechts, P. and de Wolde, J. (1999). The dynamic response of the greenland and antarctic ice sheets to multiple-century climatic warming. *Journal of Climate*, 12(8):2169–2188.
- Ingleby, B. and Huddleston, M. (2007). Quality control of ocean temperature and salinity profiles—historical and real-time data. *Journal of Marine Systems*, 65(1):158–175.
- Jacob, T., Wahr, J., Pfeffer, W. T., and Swenson, S. (2012). Recent contributions of glaciers and ice caps to sea level rise. *Nature*, 482(7386):514–518.
- Jiang, Y., Dixon, T. H., and Wdowinski, S. (2010). Accelerating uplift in the north atlantic region as an indicator of ice loss. *Nature Geoscience*, 3(6):404–407.
- Joughin, I., Alley, R. B., and Holland, D. M. (2012). Ice-sheet response to oceanic forcing. *science*, 338(6111):1172–1176.
- Khan, S. A., Wahr, J., Bevis, M., Velicogna, I., and Kendrick, E. (2010). Spread of ice mass loss into northwest greenland observed by grace and gps. *Geophysical Research Letters*, 37(6).
- Koren, I. and Feingold, G. (2011). Aerosol–cloud–precipitation system as a predator-prey problem. *Proceedings of the National Academy of Sciences*, 108(30):12227–12232.
- Krabill, W., Hanna, E., Huybrechts, P., Abdalati, W., Cappelen, J., Csatho, B., Frederick, E., Manizade, S., Martin, C., Sonntag, J., et al. (2004). Greenland ice sheet: increased coastal thinning. *Geophysical Research Letters*, 31(24).

Kuipers Munneke, P., Van den Broeke, M., Lenaerts, J., Flanner, M., Gardner, A., and Van de Berg, W. (2011). A new albedo parameterization for use in climate models over the antarctic ice sheet. *Journal of Geophysical Research: Atmospheres (1984–2012)*, 116(D5).

Letellier, T. (2005). *Etude des ondes de marée sur les plateaux continentaux*. PhD thesis, Toulouse 3.

Luthcke, S. B., Zwally, H., Abdalati, W., Rowlands, D., Ray, R., Nerem, R., Lemoine, F., McCarthy, J., and Chinn, D. (2006). Recent greenland ice mass loss by drainage system from satellite gravity observations. *Science*, 314(5803):1286–1289.

Motyka, R. J., Hunter, L., Echelmeyer, K. A., and Connor, C. (2003). Submarine melting at the terminus of a temperate tidewater glacier, leconte glacier, alaska, usa. *Annals of Glaciology*, 36(1):57–65.

Motyka, R. J., Truffer, M., Fahnestock, M., Mortensen, J., Rysgaard, S., and Howat, I. (2011). Submarine melting of the 1985 jakobshavn isbræ floating tongue and the triggering of the current retreat. *Journal of Geophysical Research: Earth Surface (2003–2012)*, 116(F1).

Murray, J. and Segall, P. (2005). Spatiotemporal evolution of a transient slip event on the san andreas fault near parkfield, california. *Journal of Geophysical Research: Solid Earth (1978–2012)*, 110(B9).

Murray, T., Scharrer, K., James, T., Dye, S., Hanna, E., Booth, A., Selmes, N., Luckman, A., Hughes, A., Cook, S., et al. (2010). Ocean regulation hypothesis for glacier dynamics in southeast greenland and implications for ice sheet mass changes. *Journal of Geophysical Research: Earth Surface (2003–2012)*, 115(F3).

Myers, P. G., Kulan, N., and Ribergaard, M. H. (2007). Irminger water variability in the west greenland current. *Geophysical Research Letters*, 34(17).

Payne, A. J., Vieli, A., Shepherd, A. P., Wingham, D. J., and Rignot, E. (2004). Recent dramatic thinning of largest west antarctic ice stream triggered by oceans. *Geophysical Research Letters*, 31(23).

Petrov, L. and Boy, J.-P. (2004). Study of the atmospheric pressure loading signal in very long baseline interferometry observations. *Journal of Geophysical Research: Solid Earth (1978–2012)*, 109(B3).

Pritchard, H. D., Arthern, R. J., Vaughan, D. G., and Edwards, L. A. (2009). Extensive dynamic thinning on the margins of the greenland and antarctic ice sheets. *Nature*, 461(7266):971–975.

Rignot, E., Box, J., Burgess, E., and Hanna, E. (2008). Mass balance of the greenland ice sheet from 1958 to 2007. *Geophysical Research Letters*, 35(20).

Rignot, E. and Kanagaratnam, P. (2006). Changes in the velocity structure of the greenland ice sheet. *Science*, 311(5763):986–990.

Schrama, E. J. and Wouters, B. (2011). Revisiting greenland ice sheet mass loss observed by grace. *Journal of Geophysical Research: Solid Earth (1978–2012)*, 116(B2).

Seale, A., Christoffersen, P., Mugford, R. I., and O’Leary, M. (2011). Ocean forcing of the greenland ice sheet: Calving fronts and patterns of retreat identified by automatic satellite monitoring of eastern outlet glaciers. *Journal of Geophysical Research: Earth Surface (2003–2012)*, 116(F3).

Shepherd, A., Wingham, D., and Rignot, E. (2004). Warm ocean is eroding west antarctic ice sheet. *Geophysical Research Letters*, 31(23).

Straneo, F., Hamilton, G. S., Sutherland, D. A., Stearns, L. A., Davidson, F., Hammill, M. O., Stenson, G. B., and Rosing-Asvid, A. (2010). Rapid circulation of warm subtropical waters in a major glacial fjord in east greenland. *Nature Geoscience*, 3(3):182–186.

- Straneo, F., Sutherland, D. A., Holland, D., Gladish, C., Hamilton, G. S., Johnson, H. L., Rignot, E., Xu, Y., and Koppes, M. (2012). Characteristics of ocean waters reaching greenland's glaciers. *Annals of Glaciology*, 53(60):202–210.
- Tedesco, M., Fettweis, X., Van den Broeke, M., Van de Wal, R., Smeets, C., van de Berg, W. J., Serreze, M., and Box, J. (2011). The role of albedo and accumulation in the 2010 melting record in greenland. *Environmental Research Letters*, 6(1):014005.
- Thomas, R., Frederick, E., Krabill, W., Manizade, S., and Martin, C. (2006). Progressive increase in ice loss from greenland. *Geophysical Research Letters*, 33(10).
- Van Angelen, J., Lenaerts, J., Lhermitte, S., Fettweis, X., Kuipers Munneke, P., van den Broeke, M., and Van Meijgaard, E. (2012). Sensitivity of greenland ice sheet surface mass balance to surface albedo parameterization: a study with a regional climate model. *Cryosphere*, 6:1175–1186.
- Van de Wal, R., Boot, W., Van den Broeke, M., Smeets, C., Reijmer, C., Donker, J., and Oerlemans, J. (2008). Large and rapid melt-induced velocity changes in the ablation zone of the greenland ice sheet. *science*, 321(5885):111–113.
- van den Broeke, M., Bamber, J., Ettema, J., Rignot, E., Schrama, E., van de Berg, W. J., van Meijgaard, E., Velicogna, I., and Wouters, B. (2009). Partitioning recent greenland mass loss. *science*, 326(5955):984–986.
- Velicogna, I. (2009). Increasing rates of ice mass loss from the greenland and antarctic ice sheets revealed by grace. *Geophysical Research Letters*, 36(19).
- Velicogna, I. and Wahr, J. (2006). Acceleration of greenland ice mass loss in spring 2004. *Nature*, 443(7109):329–331.
- Walker, J. C., Hays, P., and Kasting, J. (1981). A negative feedback mechanism for the long-term stabilization of the earth's surface temperature. *Journal of Geophysical Research*, 86(C10):9776–9782.

Wouters, B., Chambers, D., and Schrama, E. (2008). Grace observes small-scale mass loss in greenland. *Geophysical Research Letters*, 35(20).

Zumberge, J., Heflin, M., Jefferson, D., Watkins, M., and Webb, F. H. (1997). Precise point positioning for the efficient and robust analysis of gps data from large networks. *Journal of Geophysical Research: Solid Earth (1978–2012)*, 102(B3):5005–5017.

Zwally, H. J., Abdalati, W., Herring, T., Larson, K., Saba, J., and Steffen, K. (2002). Surface melt-induced acceleration of greenland ice-sheet flow. *Science*, 297(5579):218–222.

Zwally, H. J., Giovinetto, M. B., Li, J., Cornejo, H. G., Beckley, M. A., Brenner, A. C., Saba, J. L., and Yi, D. (2005). Mass changes of the greenland and antarctic ice sheets and shelves and contributions to sea-level rise: 1992–2002. *Journal of Glaciology*, 51(175):509–527.

Table 3.1: Parameters describing seasonal uplift and atmospheric/oceanic condition at KELY, KULU, QAQ1 and THU3.

Year	1997	1998	1999	2000	2001	2002	2003	2004	2005	2006	2007	2008	2009	2010
KELY														
Start time (doy)	91±12	139±7	153±8	139±9	169±12	149±15	133±23	106±21	119±40	151±9	134±5	153±28	205±74	108±36
End time (doy)	218±14	356±9	333±9	330±16	357±12	336±30	304±45	259±13	314±29	350±10	288±7	356±21	373±54	335±12
Duration (days)	128±15	217±10	180±9	191±15	188±13	187±28	171±43	153±22	195±37	198±10	154±6	203±29	169±75	228±35
Uplift (mm)	2.9±1.0	10.0±1.3	8.8±1.5	10.3±1.7	7.5±1.6	4.3±1.4	3.4±1.3	3.4±1.1	3.1±1.0	5.6±1.0	7.0±1.0	6.4±2.2	2.1±2.2	14.1±2.5
Uplift rate (10^{-2} mm day $^{-1}$)	2.2±0.6	4.6±0.6	4.9±0.8	5.4±0.8	4.0±0.8	2.3±0.7	2.0±0.7	2.2±0.6	1.6±0.5	2.9±0.5	4.5±0.5	3.2±0.4	1.2±0.5	6.2±0.6
AMSAT (°C)	N/D	N/D	-3.3	-4.3	-5.6	-2.7	-5.0	-2.6	-4.4	-4.2	-4.4	-4.7	-4.7	-0.2
CAPDD (days)	N/D	N/D	166	172	155	175	162	161	170	156	163	148	196	196
AMSSWT (°C)	N/D	N/D	2.4	2.7	2.3	2.6	2.9	2.8	2.4	2.4	2.5	2.3	3.1	3.1
KULU														
Start time (doy)	152±8	144±6	172±11	155±6	140±12	187±9	245±11	188±15	77±10	193±11	172±3			
End time (doy)	338±7	322±8	294±10	365±14	396±7	389±9	400±9	315±23	355±4	369±3	356±2			
Duration (days)	185±8	177±8	122±33	210±13	255±13	203±10	154±11	127±24	278±11	176±11	185±3			
Uplift (mm)	9.9±1.2	7.0±1.1	2.6±0.8	10.3±1.1	7.4±1.0	9.1±1.0	4.5±0.8	1.4±0.8	11.1±0.7	7.2±0.6	14.7±0.7			
Uplift rate (10^{-2} mm day $^{-1}$)	5.3±0.5	4.0±0.6	2.1±0.5	4.9±0.6	2.9±0.4	4.5±0.5	2.9±0.5	1.1±0.5	4.0±0.3	4.1±0.4	7.9±0.4			
AMSAT (°C)	-0.5	-0.5	0.2	1.2	0.1	0.5	-0.5	0.1	-1.4	-1.0	0.5			
CAPDD (days)	185	208	203	215	200	184	184	189	155	155	195			
AMSSWT (°C)	4.9	5.1	5.0	5.4	5.6	5.5	5.1	5.5	5.5	5.5	5.9			
QAQ1														
Start time (doy)	144±14	192±8	198±7	219±6	194±56	165±37	225±23	165±11						
End time (doy)	336±19	376±9	404±5	384±6	298±65	350±19	384±13	370±8						
Duration (days)	192±18	183±9	206±7	165±7	101±40	185±36	159±21	204±12						
Uplift (mm)	4.6±0.9	6.8±0.8	8.3±0.8	5.8±0.7	0.6±0.4	3.6±1.6	5.1±1.5	12.4±1.7						
Uplift rate (10^{-2} mm day $^{-1}$)	2.4±0.5	3.7±0.4	4.0±0.4	3.5±0.4	0.5±0.3	1.9±0.4	3.2±0.4	6.1±0.4						
AMSAT (°C)	2.6	2.1	2.6	1.6	2.0	0.5	1.4	4.6						
CAPDD (days)	240	242	258	215	229	219	194	272						
AMSSWT (°C)	4.9	4.9	4.8	4.7	4.6	4.6	4.3	4.9						
THU3														
Start time (doy)	161±20	330±30	154±7	185±24	149±11	76±277	218±37	211±16						
End time (doy)	377±10	426±9	392±7	384±11	420±126	367±29	398±23	350±11						
Duration (days)	217±20	97±32	238±9	194±32	268±125	333±257	184±36	139±16						
Uplift (mm)	5.1±1.0	1.3±0.6	6.0±0.9	1.4±0.8	2.5±1.4	3.5±3.4	5.6±2.0	5.7±1.9						
Uplift rate (10^{-2} mm day $^{-1}$)	2.4±0.5	1.3±0.5	2.5±0.4	0.7±0.4	0.9±0.3	1.2±0.3	3.1±0.4	4.1±0.5						
AMSAT (°C)	-7.8	-9.6	-8.7	N/D	-8.5	-9.2	-9.0	-6.8						
CAPDD (days)	117	113	119	N/D	103	113	107	116						
AMSSWT (°C)	0.3	0.3	0.3	0.4	0.4	0.3	0.1	0.2						

Note: Uncertainty is defined at the 68% confidence interval (Appendix A). Units for start time and end time are day of year (doy). End times exceeding 365/366 indicate that seasonal uplift continues to the following year. N/D – no data.

Table 3.2: Recent uplift history and glacier proximity for all GPS sites considered in this study.

Site	Glacier	Distance (km)	Uplift(mm)			2010 Uplift	Increase(%)
			2008	2009	2010		
DKSG	M	5	5.2±0.8	8.3±0.7	8.1±1.0	35.8±12.7	-2.5±15.3
HEL2	M	3	12.2±0.7	9.0±0.7	19.0±0.7	35.80±4.4	52.6±4.1
HJOR	M	15	12.5±0.7	7.0±0.6	18.3±0.7	31.7±4.6	61.7±3.6
KAGA	M	7	7.6±0.7	8.3±0.7	16.7±0.8	54.5±4.7	50.3±4.8
KELY	L	30	6.4±1.0	2.1±1.0	14.1±1.1	54.6±7.9	85.1±7.2
KSNB	M	50	9.6±0.8	7.6±0.6	12±0.8	20.0±8.5	36.7±6.5
KULL	M	25	6.0±0.7	8.5±0.7	6.5±0.7	7.7±14.7	-30.8±17.7
KULU	M	50	2.3±3.4	2.9±0.7	11.9±0.8	80.7±28.6	75.6±6.1
LYNS	M	20	11.1±0.7	7.2±0.6	14.1±0.7	21.3±6.3	48.9±5.0
MARG	M	2	4.6±0.9	7.2±0.7	6.9±0.8	33.3±15.2	-4.3±15.8
PLPK	M	2	9.8±0.8	5.8±0.7	14.2±1.0	31.0±7.4	59.2±5.7
QAQ1	M/L	50/45	3.6±0.7	5.1±0.6	12.4±0.7	71.0±5.9	58.9±5.4
RINK	M	7	6.9±0.8	7.3±0.7	10.0±0.8	31.0±9.7	27.0±9.1
SENU	M/L	12/3	N/D	11.5±0.6	19.3±0.7	N/D	40.4±3.8
SRMP	M	2	6.9±0.7	7.7±0.7	11.6±0.8	40.5±7.3	33.6±7.6
THU3	M	25	3.5±1.5	5.6±0.8	5.7±0.8	38.6±27.7	1.8±19.6
TIMM	M	35	10.4±0.7	8.4±0.7	13.7±0.7	24.1±6.4	38.7±6.0
TREO	M	9	14.7±0.7	5.4±0.6	17.6±0.8	16.5±5.5	69.3±3.7

Note: M represents marine-terminating glacier, L represents land-terminating glacier. Percentage differences between uplift in 2010 and uplift in two earlier years are shown in last two columns.

Table 3.3: GPS uplift data fit to a model of constant acceleration.

a	Site	Longitude (deg N)	Longitude (deg E)	T _{start} (yr)	T _{stop} (yr)	N (Day)	V ₀ (mm yr ⁻¹)	Acceleration (mm yr ⁻²)	Amp (mm)	RMS (mm)
	DKSG	76.35	-61.67	2007.64	2011.39	1263	21.3±0.8	-1.6±0.4	4.3	7.4
	HEL2	66.40	-38.22	2007.65	2011.39	1324	4.3±0.8	6.9±0.4	8.1	7.4
	HJOR	63.42	-41.15	2007.62	2011.39	1134	1.1±0.9	4.3±0.5	7.4	7.9
	KAGA	69.22	-49.81	2007.36	2011.39	1418	11.1±0.9	4.3±0.4	6.5	8.1
	KELY	66.99	-50.94	2007.64	2011.39	1062	0.0±0.9	2.7±0.4	4.9	7.2
	KSNB	66.86	-35.58	2007.64	2011.39	1271	2.2±0.7	5.5±0.4	5.1	6.9
	KULL	74.58	-57.23	2007.62	2011.39	1311	12.2±0.8	-0.9±0.4	3.9	7.4
	KULU	65.58	-37.15	2007.61	2011.39	1171	4.9±0.8	2.6±0.4	3.7	7.2
	LYNS	64.43	-40.20	2007.66	2011.39	1341	7.1±0.9	2.0±0.5	5.4	8.5
	MARG	77.19	-65.69	2007.67	2011.39	1349	10.8±0.8	-0.3±0.4	2.9	7.8
	PLPK	66.90	-34.03	2007.61	2011.18	1235	-1.3±0.8	7.0±0.5	4.8	7.4
	QAQ1	60.72	-46.05	2007.65	2011.39	1250	-0.9±0.8	3.3±0.4	3.7	7.0
	RINK	71.85	-50.99	2007.67	2011.39	1346	4.2±0.8	3.4±0.4	4.7	7.9
	SENU	61.07	-54.39	2008.38	2011.39	1053	-5.4±1.0	11.8±0.6	11.5	6.9
	SRMP	72.91	-47.14	2007.62	2011.39	1365	15.1±0.7	1.6±0.4	4.7	7.4
	THU3	76.54	-68.83	2007.64	2011.39	1195	11.0±0.8	-1.2±0.4	2.6	7.8
	TIMM	62.54	-42.29	2007.65	2011.28	1115	3.1±1.0	3.1±0.5	6.6	8.7
	TREO	64.28	-41.38	2007.67	2011.39	1273	1.6±0.9	5.0±0.4	6.4	8.2
b	KELY	66.99	-50.94	1996.04	2011.39	4564	-3.2±0.1	0.6±0.1	3.8	7.5
	KULU	65.58	-37.15	1999.88	2011.39	3696	3.5±0.2	0.8±0.1	3.8	8.3
	QAQ1	60.72	-46.05	2002.39	2011.39	3034	1.8±0.3	0.5±0.1	3.5	6.9
	THU3	76.54	-68.83	2002.40	2011.39	3017	4.5±0.4	0.7±0.1	1.9	7.8

T_{start,end}: start and end time of GPS time series, in years.

N: number of days of data in GPS time series.

Amp: amplitude of annual variation.

RMS: root mean square misfit of the constant acceleration model to the time series.

V₀: vertical velocity at the beginning of time series.

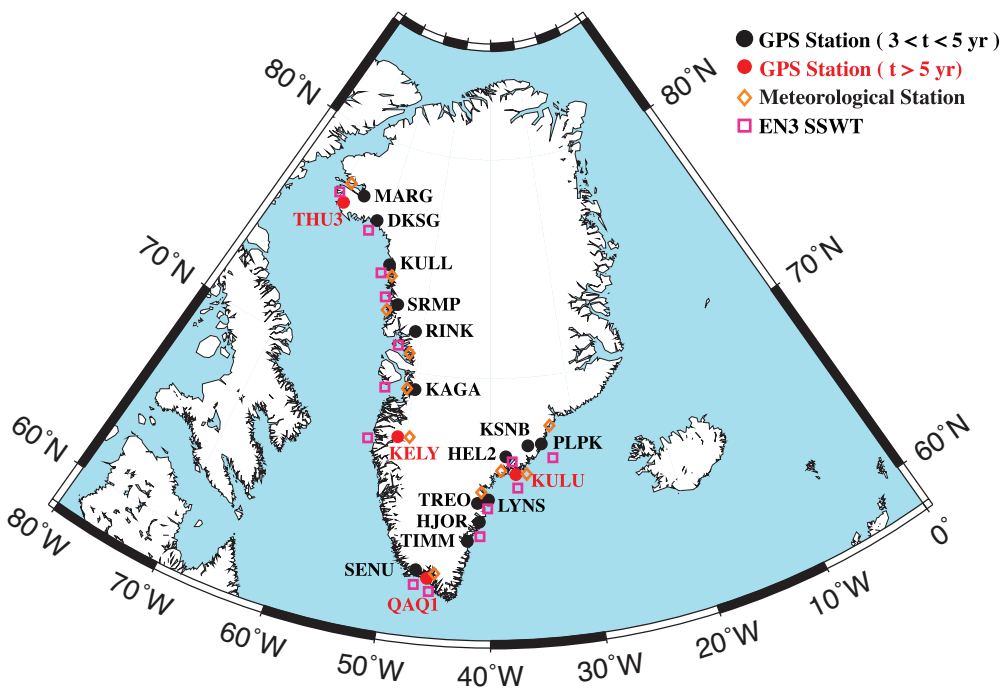


Figure 3.1: Map of Greenland showing location of GPS sites, meteorological stations, and other data used in this study. Red circles indicate GPS sites with more than 5 years of data. Black circles indicate sites with 3 to 5 years of data. Orange diamonds indicate meteorological stations. Pink squares indicate pixels of sub-surface water temperature produced by EN3 model.

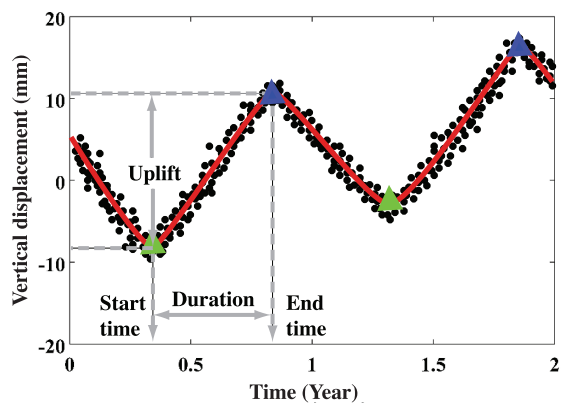


Figure 3.2: Hypothetical 2 year time series showing four parameters (start time, end time, duration, and uplift) defined for a melt season. Each black dot represents daily vertical position estimate. Red curve is best fit model. Blue triangles mark the maximum position value per year, and green triangles are the minimum value per year. A fifth parameter (rate of summer uplift) is the average slope of the curve between the start time and end time of uplift.

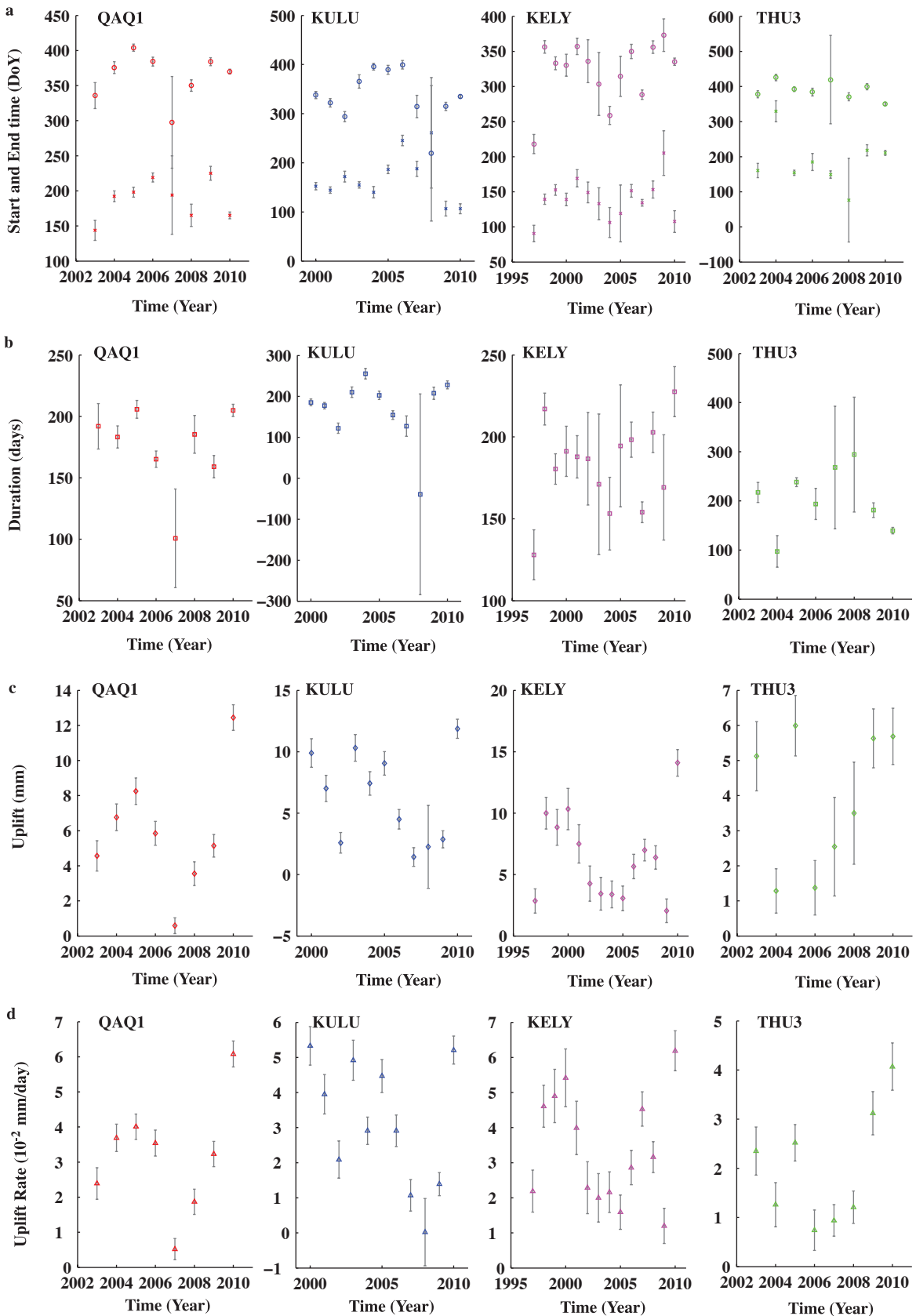


Figure 3.3: Annual variations of the five parameters defining seasonal uplift calculated for the four sites with longest observation record (red circles in Figure 3.1). (a) Uplift start time (cross) and end time (circle), (b) uplift duration, (c) uplift magnitude, and (d) uplift rate. Gray line represents uncertainty.

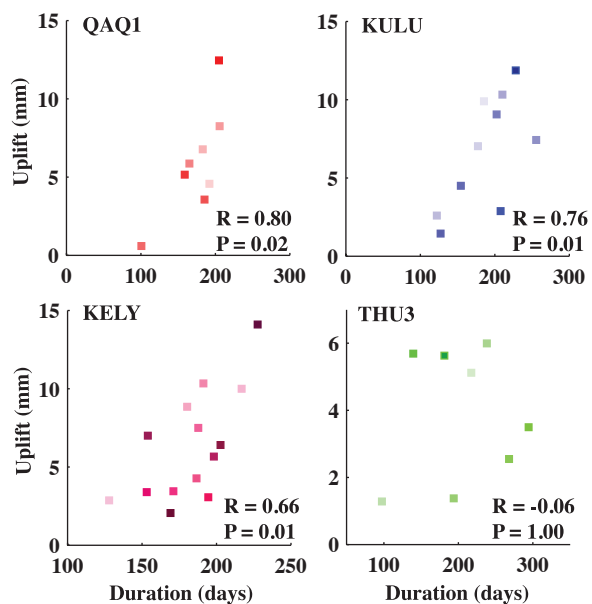


Figure 3.4: Uplift versus duration for the four sites with longest observation record. Colors varying from light to dark represent data from earlier to more recent.

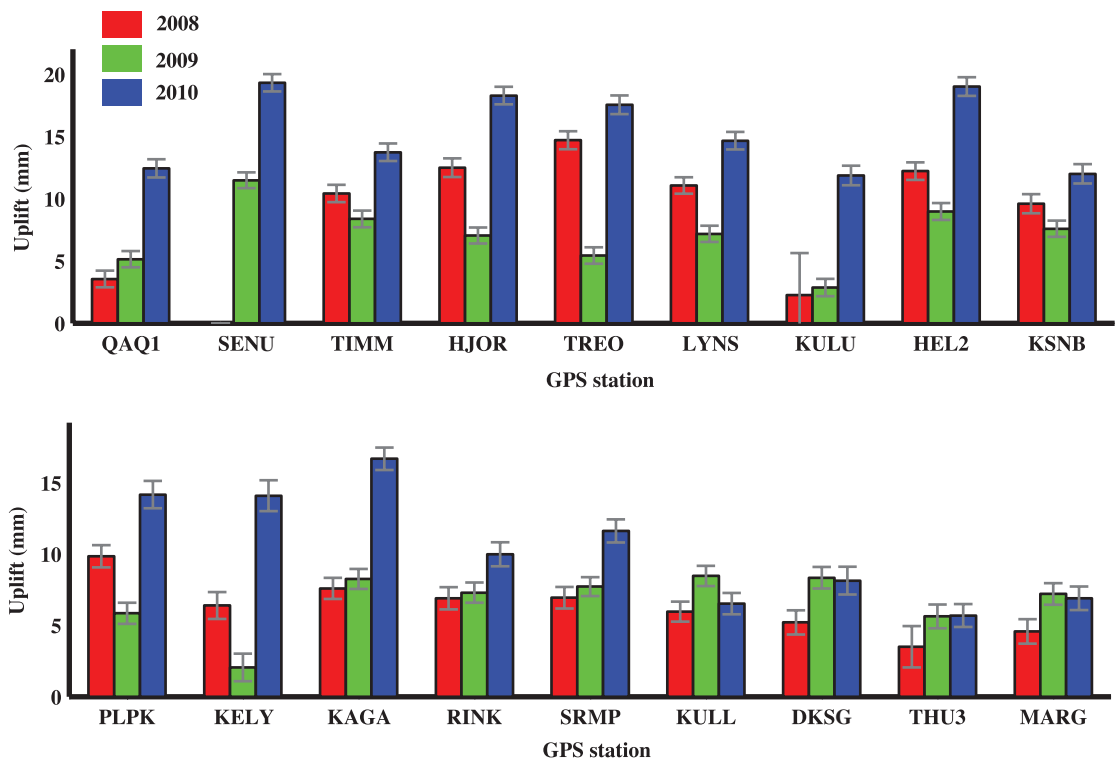


Figure 3.5: Seasonal uplift patterns for 2008–2010. GPS sites are ordered by latitude, from south to north. Note change between KAGA (69.2°N) and RINK (71.9°N) with lower amplitude and lower variability uplift at the more northern sites.

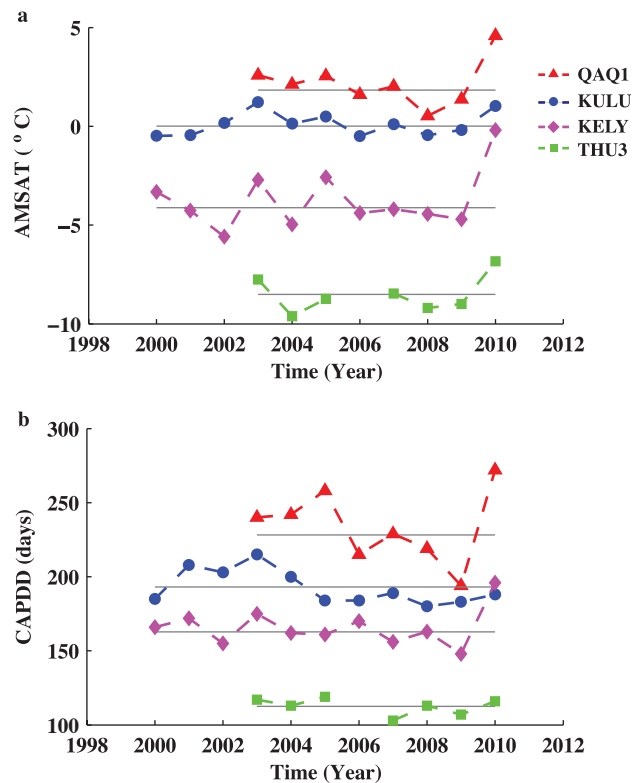


Figure 3.6: (a) AMSAT (Annual mean surface air temperature). (b) CAPDD (Cumulative annual positive degree days) for the four GPS stations with longest observation record. Solid gray line represents the mean value of reference period.

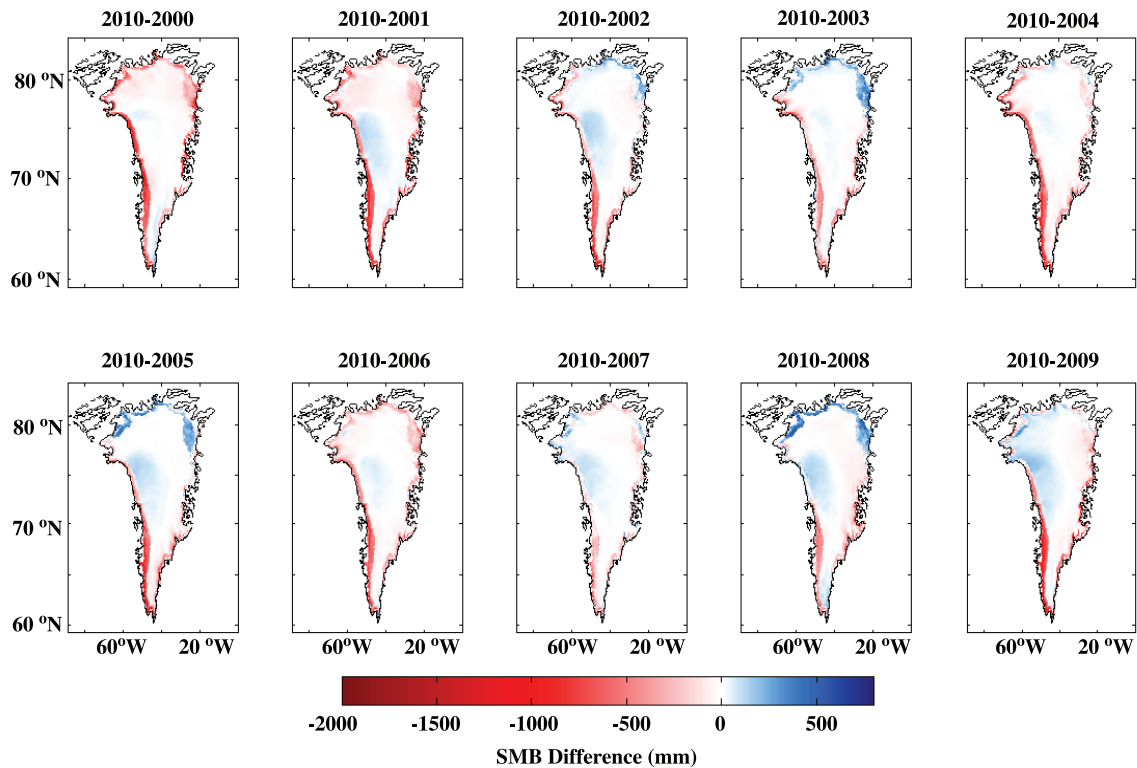


Figure 3.7: Difference of Surface Mass Balance (SMB model from RACMO2) in summertime (June to August) between 2010 and 20XX (XX= 00–09) for the Greenland region. Red color indicates that 2010 had a relatively negative SMB (more surface mass loss or less surface mass gain) compared to previous years, and blue color indicates that 2010 had a relatively positive SMB (less surface mass loss or more surface mass gain) compared to previous years.

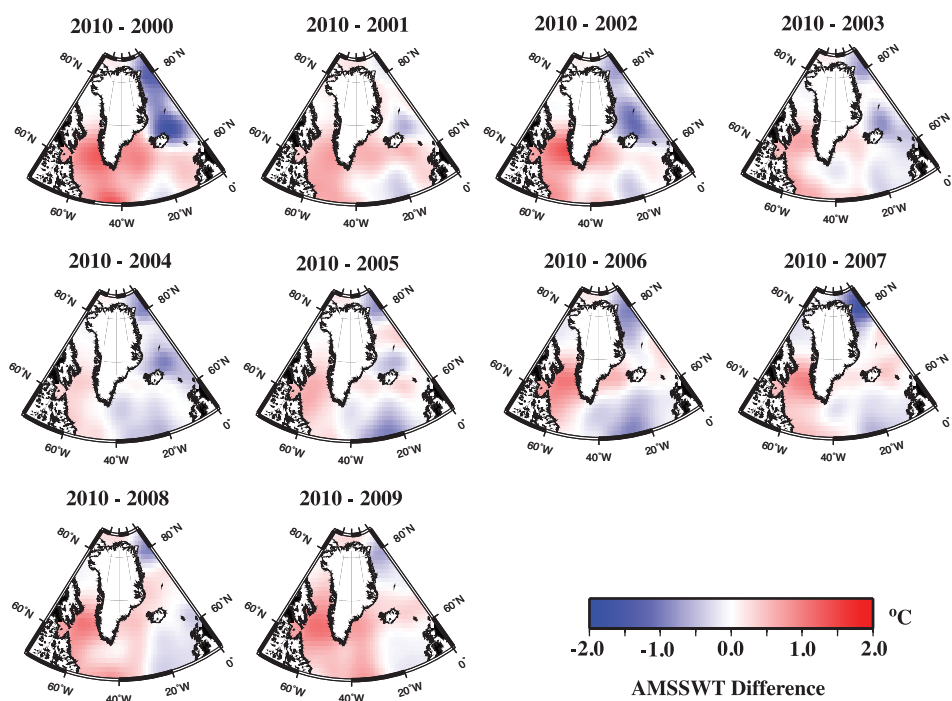


Figure 3.8: Difference of AMSSWT (Annual mean, sub-surface water temperature, depth range 5m – 447 m) between 2010 and 20XX (XX = 00–09) for the Greenland region. Warmer colors indicate that 2010 was warmer than the previous year at a given location.

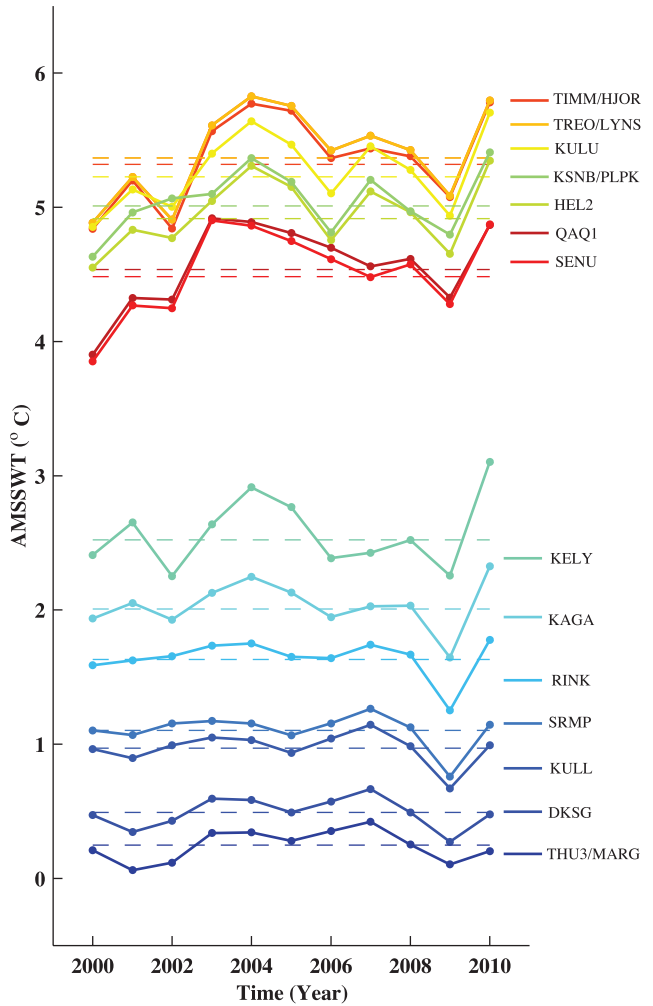


Figure 3.9: AMSSWT (Figure 3.8) for “voxels” (model volume elements) nearest a given GPS station. Warmer colors indicate southern latitudes, cooler colors indicate northern latitudes. Dashed color line represents 2000–2009 means. Note the pronounced 2010 anomaly for most locations, decreasing in intensity to the north.

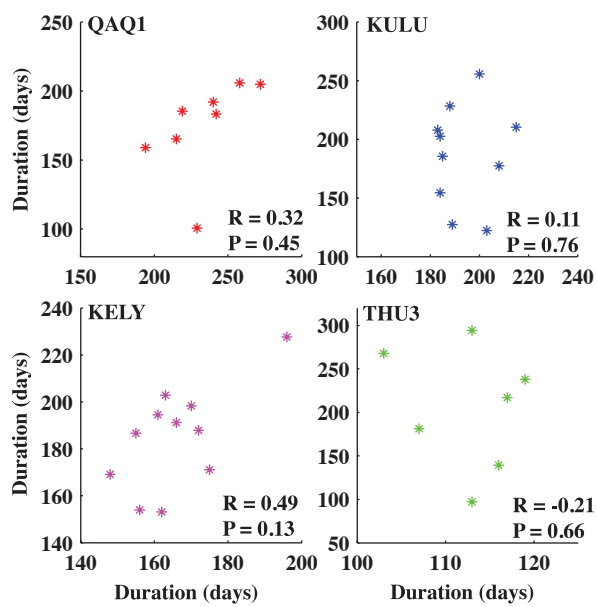


Figure 3.10: Uplift duration versus CAPDD (Figure 3.6).

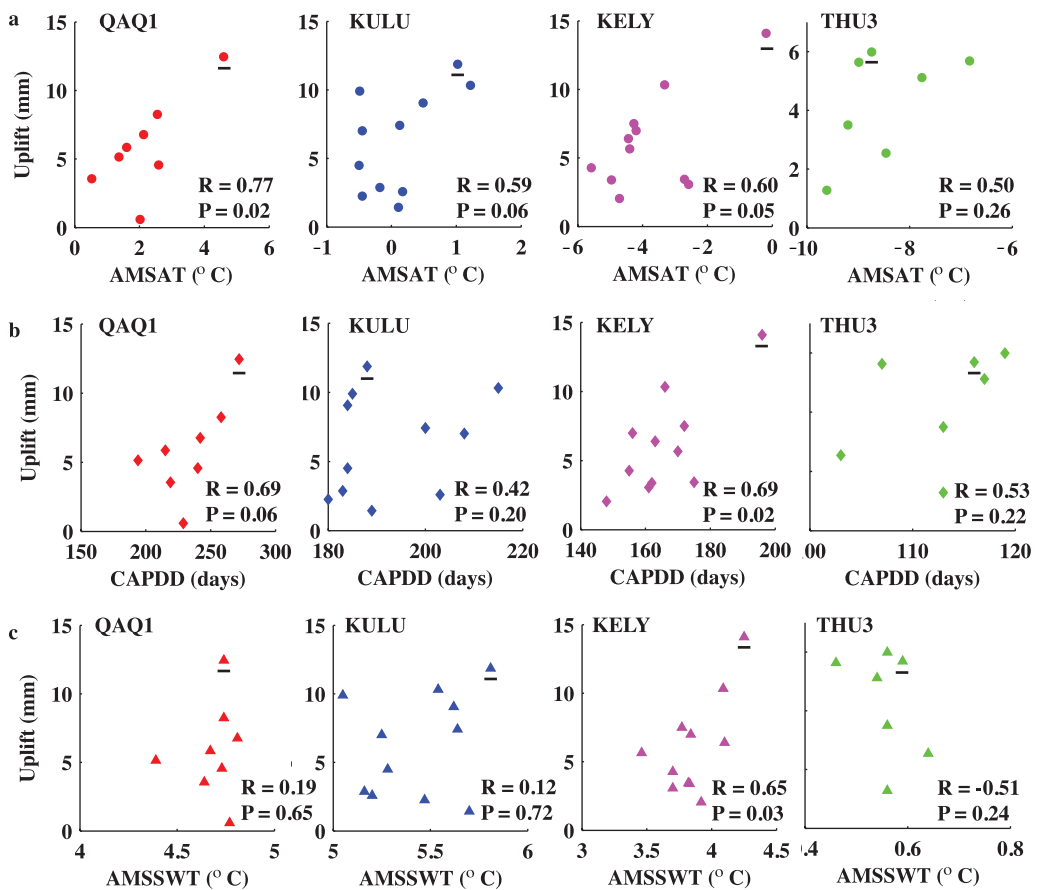
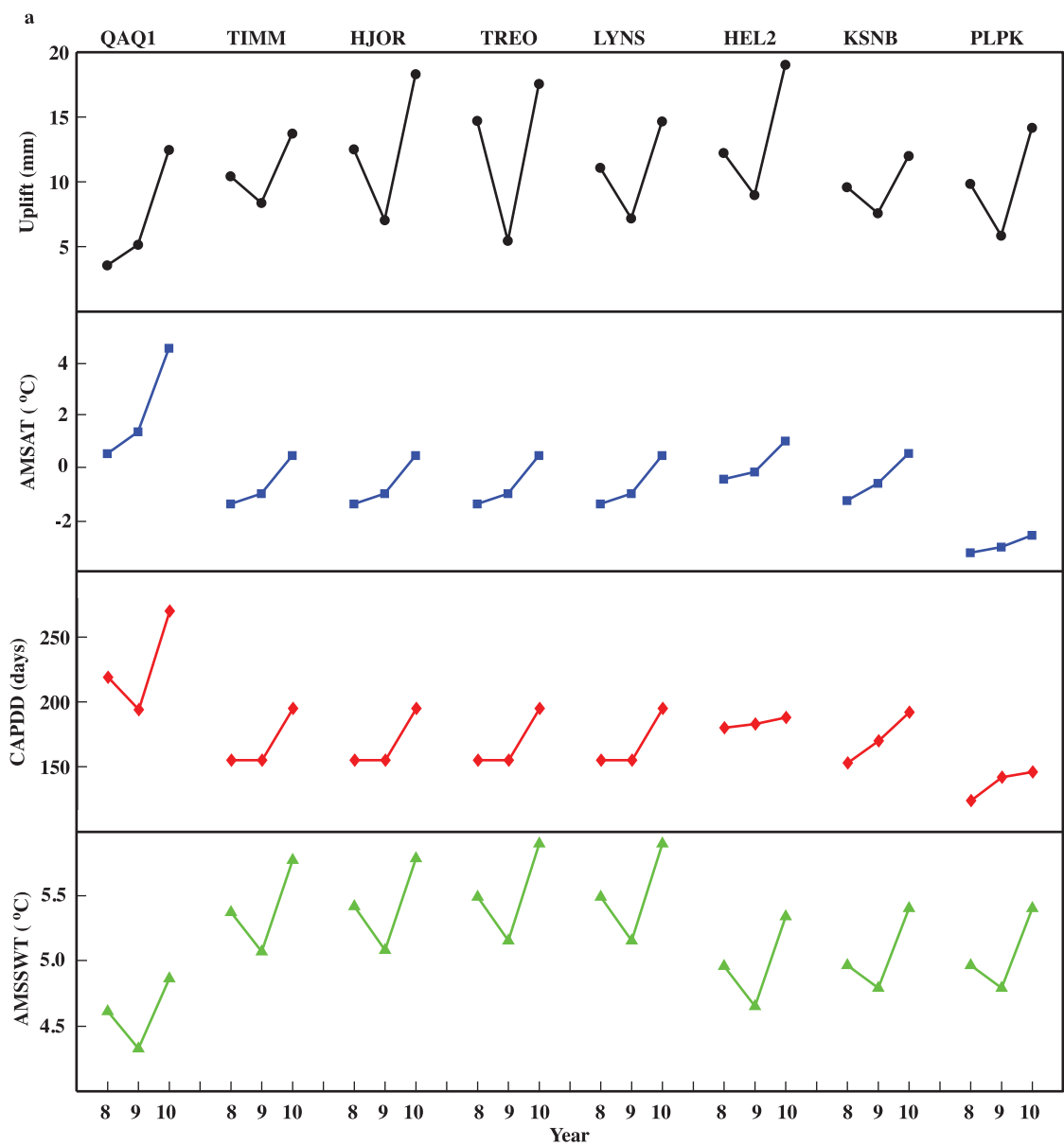


Figure 3.11: Spatial variation of seasonal uplift for four stations with longest time span related to (a) AMSAT (Figure 3.6); (b) CAPDD (Figure 3.6); and (c) AMSSWT (Figure 3.8). Underlined symbol is 2010.



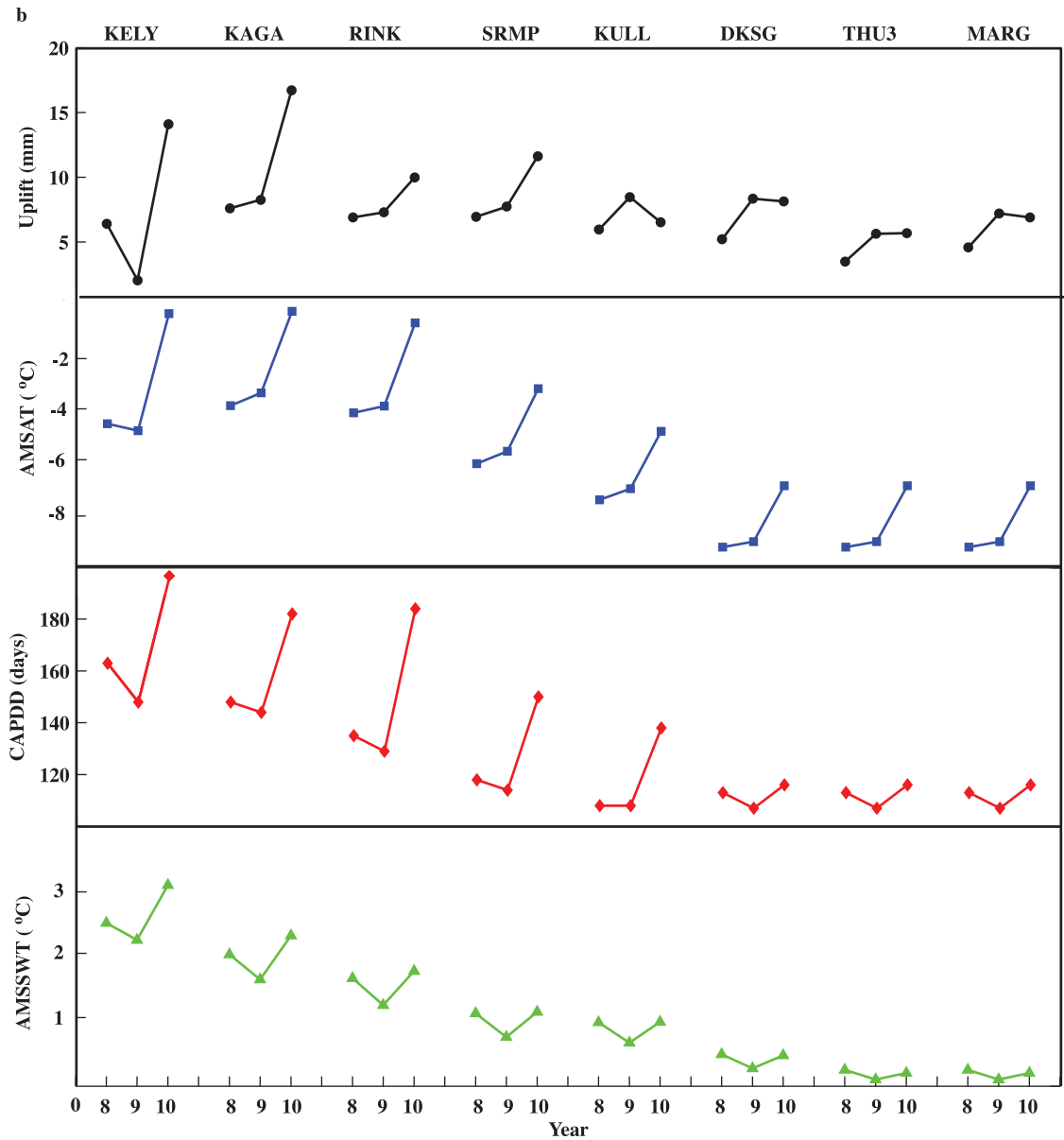


Figure 3.12: Comparison between seasonal uplift patterns and atmospheric parameters (AMSAT and CAPDD, Figure 3.6) as well as the ocean temperature parameter (AMSSWT, Figure 3.8) for 2008–2010. Uplift pattern as shown in Figure 3.5. SENU and KULU are eliminated here due to lack of data in 2008. GPS stations are ordered from south to north.

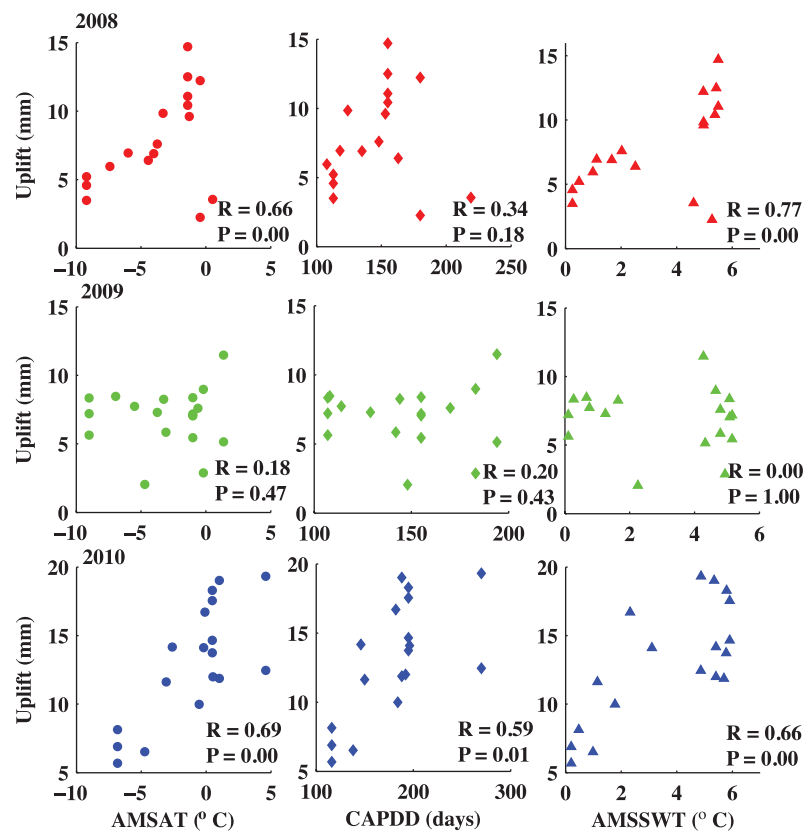


Figure 3.13: Temporal variation of seasonal uplift for all stations for 2008–2010 as a function of AMSAT (Figure 3.6), CAPDD (Figure 3.6), and AMSSWT(Figure 3.8).

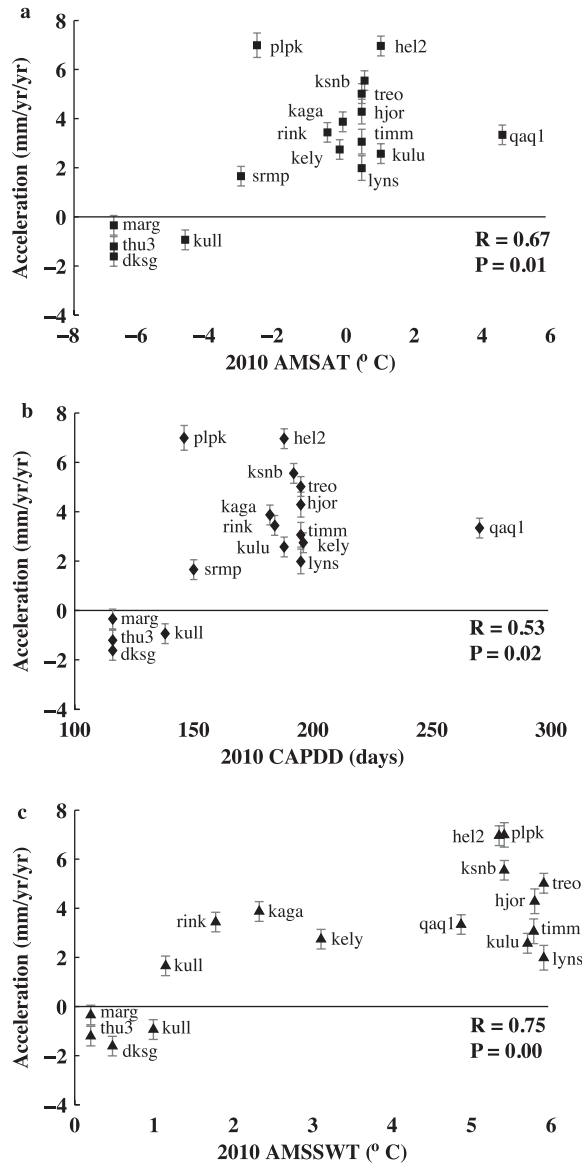


Figure 3.14: Spatial variation of uplift accelerations as a function of (a) AMSAT (Figure 3.6), (b) CAPDD (Figure 3.6), and (c) AMSSWT (Figure 3.8) of 2010.

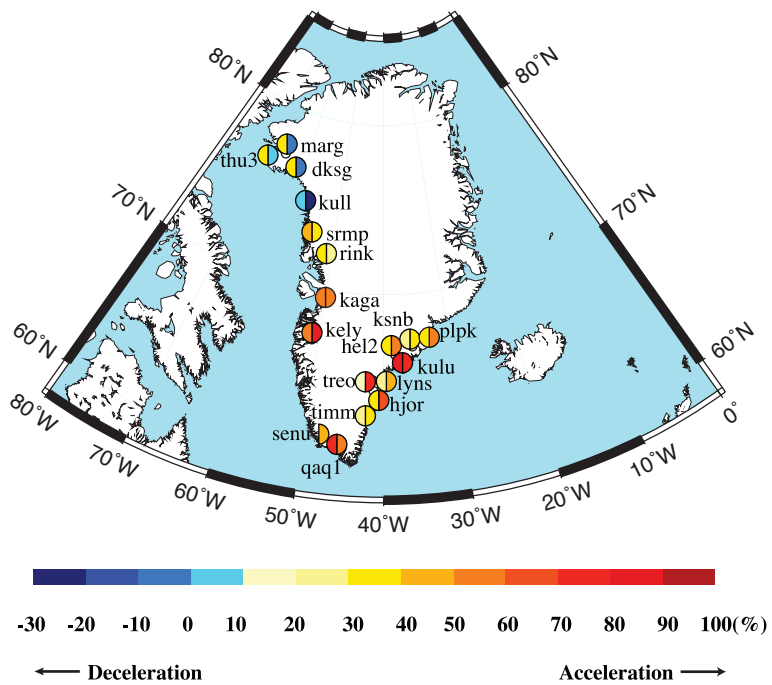


Figure 3.15: Site map of relative difference between uplift in 2010 and uplift in 2008 and 2009. The left half circle shows percentage difference between the uplift in 2008 and 2010: $\Delta U_{10/08} = (U_{10} - U_{08})/U_{10}$; right half circle shows percentage difference between uplift in 2009 and 2010: $\Delta U_{10/09} = (U_{10} - U_{09})/U_{10}$.

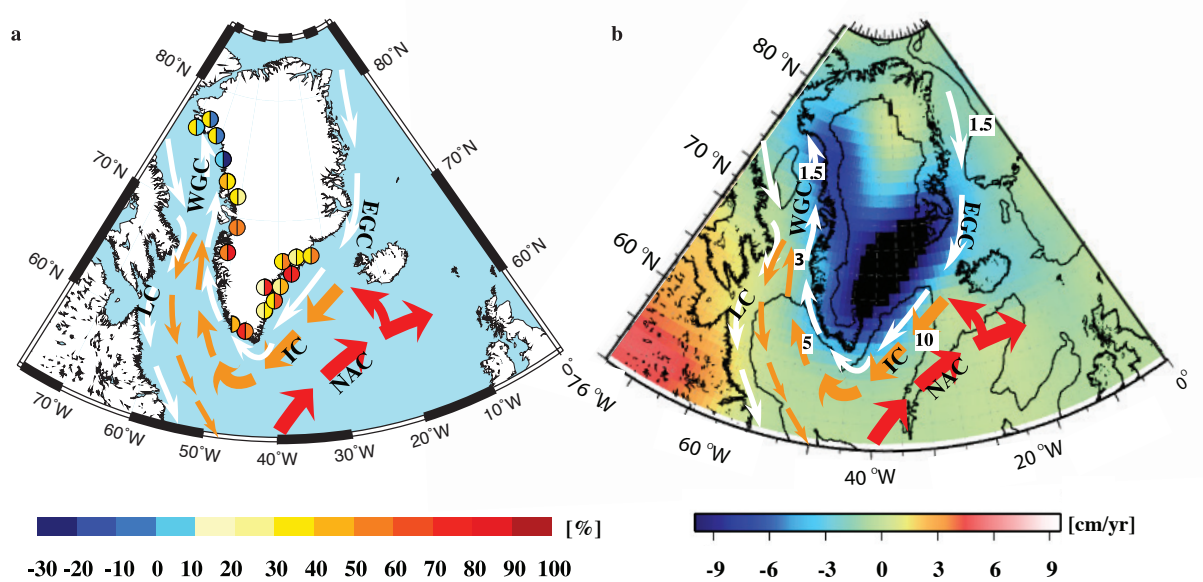


Figure 3.16: Relation between ocean currents, coastal uplift, and ice mass balance of coastal Greenland. Red arrows indicate the mean path of the warm North Atlantic Current (NAC); orange arrows indicate Irminger Current (IC), white arrows indicate East Greenland Current (EGC), West Greenland Current (WGC) and Labrador Current (LC). (a) Relative difference between uplift in 2010 and that in 2008 and 2009 as shown in Figure 15. Names of GPS stations were omitted here. (b) Mass loss in equivalent water height over Greenland between February 2003 and January 2008 observed by GRACE (Wouters et al., 2008). Numbers indicate the mean temperature ($^{\circ}\text{C}$) of Atlantic-sourced waters on the Greenland shelf (Straneo et al., 2012).

4. Recent increases in Arctic freshwater flux affects Labrador Sea convection and Atlantic overturning circulation ²

4.1 Abstract

The Atlantic Meridional Overturning Circulation (AMOC) is an important component of ocean thermohaline circulation. Melting of Greenland's ice sheet is freshening the North Atlantic, but whether the augmented freshwater flux is disrupting the AMOC is unclear. Dense Labrador Sea Water (LSW), formed by winter cooling of saline North Atlantic water and subsequent convection, is a key component of the deep southward return flow of the AMOC. Although LSW formation recently decreased, it also reached historically high values in the mid-1990s, making the connection to freshwater flux unclear. Here we derive a new estimate of recent freshwater flux from Greenland using updated GRACE satellite data, present new flux estimates for heat and salt from the North Atlantic into the Labrador Sea, and explain recent variations in LSW formation. We suggest that changes in LSW can be directly linked to recent freshening, and suggest a possible link to AMOC weakening.

4.2 Introduction

It has long been accepted that the AMOC has two stable modes (Stommel, 1961; Rooth, 1982; Broecker et al., 1985) and that anthropogenic warming could weaken or shut down the AMOC (Broecker, 1987; Wood et al., 1999). Recent accelerated melting of the Greenland ice sheet is freshening the North Atlantic (Jiang et al., 2010; Rignot et al., 2011; Enderlin et al., 2014; Velicogna et al., 2014; Yang et al., 2013). So-called “hosing experiments”, where freshwater may be distributed over broad or narrow regions of the North Atlantic in numerical models, have been used to study the sensitivity of the

²This chapter has been reprinted from Nature Communications: Yang, Q., Dixon, T. H., Myers, G. P., Bonin, J., Chambers, D., van den Broeke, M. R., (2016), Recent increases in Arctic freshwater flux affects Labrador Sea convection and Atlantic overturning circulation, Nat. Commun., 7:10525, doi: 10.1038/ncomms10525.

AMOC to freshwater flux Fichefet et al. (2003); Jungclaus et al. (2006); Stouffer et al. (2006); Hu et al. (2011); Swingedouw et al. (2013); Ridley et al. (2005); Brunnabend et al. (2015). Some of these studies suggest that AMOC strength is sensitive to Greenland melting (Fichefet et al., 2003; Brunnabend et al., 2015) while others do not (Jungclaus et al., 2006; Hu et al., 2011; Ridley et al., 2005). A few studies suggest that freshwater additions of 0.1 Sv (100 mSv) (Rahmstorf, 1995; Rahmstorf et al., 2005; Hawkins et al., 2011) or possibly less (Fichefet et al., 2003; Brunnabend et al., 2015) could affect the AMOC.

Changes in the AMOC are difficult to measure directly: currents that comprise the deeper, southward flowing portions can be diffuse and/or spatially and temporally variable, and instrumental drift can mask subtle, long term changes in oceanic properties. It is also challenging to separate changes forced by anthropogenic warming from natural variability. The AMOC is difficult to model numerically: model grids may be too coarse to reflect realistic oceanic processes and geographic constraints, and feedbacks among atmosphere, ocean and cryosphere (land and sea ice) are poorly known.

The Labrador Sea is a key location for the formation of one of the dense, deep water components of the AMOC via winter convection, but the process is sensitive to surface conditions (Yashayaev and Loder, 2009). Wood et al. (1999) suggest the possibility of a shutdown in Labrador Sea convection in response to global warming. Kuhlbrodt et al. (2001) provide a theoretical stability analysis, and suggest that winter convection in the Labrador Sea can be turned off by increased freshwater input. Unfortunately, winter convection here is difficult to observe directly due to extreme conditions and its small spatial scale.

Here we consider recent Labrador Sea changes associated with increased freshwater flux. We derive a new estimate for recent increased freshwater flux into the sub-polar North Atlantic, and suggest that because of the clockwise nature of ocean circulation around Greenland (Joyce and Proshutinsky, 2007), most of this increase is being focused towards the Labrador Sea (Figure 4.1), magnifying its impact and increasing the likelihood of significant effects on the AMOC.

4.3 Results

4.3.1 Recent accelerated melting of the Greenland ice sheet

Numerous studies have described recent acceleration of Greenland's ice mass loss (Jiang et al., 2010; Rignot et al., 2011; Enderlin et al., 2014; Velicogna et al., 2014; Yang et al., 2013). We use GRACE data updated to October 2014 to derive a new acceleration estimate and its onset time (Methods). GRACE data and uncertainty estimates follow Bonin and Chambers (2013). We fit a constant acceleration model to the data, and extrapolate the best-fit model back to the time of zero mass loss rate, obtaining 20 Gt yr⁻² acceleration with a start time of 1996 ± 1.4 years (Figure 4.2). Several lines of evidence suggest that the ice sheet was relatively stable from 1980 to the early 1990s (Howat and Eddy, 2011; Box and Colgan, 2013), and we use that assumption in our modeling of GRACE data and freshwater flux calculations (below and Methods section).

4.3.2 Irminger Water heat and salt fluxes

Warming of sub-polar mode waters including Irminger Water in the mid- to late-1990s (Myers et al., 2007b; Thierry et al., 2008) is thought to influence coastal mass loss in Greenland by increasing submarine melting of outlet glaciers and related dynamic effects (Holland et al., 2008; Joughin et al., 2012; Straneo and Heimbach, 2013). Here, we examine the variability of heat and salt fluxes of Irminger Water along three sections (Figure 4.1) offshore southwest coastal Greenland for the period 1949 – 2013 (Methods). Currents associated with the sub-polar gyre here are quite compact as they round the southern tip of Greenland, limiting spatial variability and facilitating accurate flux measurements, because the cross section area of current is well defined. Note that while flux (*sensu stricto*) is flow rate per unit area, and transport (or total flux) represents the flux integrated over the larger area of interest, the terms “flux” and “transport” are often used interchangeably in the oceanographic literature. We follow the broader (*sensu lato*) usage here.

We carry out our analysis on the upper 700 m, the greatest depth common to all years, binned on a 2 m vertical grid. Time series of heat flux and salt flux at the three sections are shown in Figure 4.3. At the southernmost Cape Farewell section, both

heat flux and salt flux experienced a large multi-year anomaly around 1995, followed by another in the late 1990s. The heat flux was 80% higher than a previous multi-year anomaly in the 1960s. Similar variability is seen at the more northerly Cape Desolation section, although salinities and heat are generally lower, and only exceed previous levels after 2000. No significant anomalies were observed at the northernmost Paamiut section during these times, but the heat and salt fluxes are still roughly 50% higher after 2000 than they were in the 1980s, and approach levels not seen since the 1960s. Thus, we conclude that Irminger Water became warmer and saltier in the mid-late 1990s, which agrees well with the onset time of recent accelerated Greenland mass loss (Figure 4.22). This is consistent with the idea that accelerating ice mass loss in the mid-late 1990s reflects, at least in part, the appearance of warmer Irminger Water on the peripheral continental shelf at that time (Holland et al., 2008). The anomalous heat flux we observe off southern Greenland in the mid-1990s can be directly tied to warming of the North Atlantic (Figure A9; see also Straneo and Heimbach (2013)).

Northward reduction in heat and salt transport between the Cape Desolation and Paamiut sections likely reflects strong offshore eddy transport (Jakobsen et al., 2003), advecting Irminger Water into the interior of the Labrador Sea. However, since the sections are only occupied once a year in summer, some seasonal aliasing is possible. The eddies also transport fresh shelf water into the Labrador Sea (Myers et al., 2009).

4.3.3 Estimates of freshwater flux into the Labrador Sea

Major sources of freshwater entering the Labrador Sea include precipitation, oceanic transport, and melt from the Greenland ice sheet, glaciers in the Canadian Arctic Archipelago (CAA) and Arctic sea ice. Precipitation in the Labrador Sea region is about 20 – 30 mSv (Myers et al., 2007a) , and there has been a general increase over the North Atlantic region in the last few decades as the hydrologic cycle accelerates (Josey and Marsh, 2005). Oceanic transport from the Arctic Ocean is the largest source of Labrador Sea freshwater, and is derived from several sources, including the difference between precipitation and evaporation, river discharge, and fractionation associated with annual sea ice formation. Peterson et al. (2002) show that the average annual river

discharge from six rivers in Eurasia into the Arctic Ocean has increased by 7% (~ 4 mSv) from 1936 to 1999. The Arctic Ocean exports low salinity water to the North Atlantic through two main pathways: Fram Strait east of Greenland, and the CAA west of Greenland. The CAA pathway has three main routes: Barrow Strait, Nares Strait, and Cardigan Strait-Hell Gate. Roughly 100 mSv of freshwater is exported through each of the east and west pathways, relative to a reference salinity of 34.80 (Haine et al., 2015). Within broad error bars, oceanic transport from the Arctic Ocean is relatively stable on the decadal time scale, although there has been some reduction through the CAA and then Davis Strait, and shorter term fluctuations are common (Haine et al., 2015; Castro de la Guardia et al., 2015; Curry et al., 2014).

Here we focus on three Arctic freshwater sources that are undergoing rapid increases, that likely contribute freshwater to the Labrador Sea, and that can be estimated from remote observations: the Greenland ice sheet, CAA glaciers, and Arctic sea ice. We also consider snowmelt runoff from tundra in Greenland and the CAA as they follow directly from the same models used to quantify Greenland ice sheet and CAA glacier melt (Bamber et al., 2012; Lenaerts et al., 2013). As we are not considering the large Arctic oceanic transport term and several other sources, our estimate is a minimum estimate.

Freshwater flux from Greenland is composed of ice and tundra runoff plus ice discharge; this quantity is equal to accumulation minus mass balance (Methods). We derive mass balance for Greenland from GRACE, while accumulation is obtained from the RACMO2.3 model Ettema et al. (2009); Noël et al. (2015). Our GRACE data suggest that mass loss of the Greenland ice sheet accelerates from 1996 onward (Figure 4.2, Methods). Our mass balance estimate agrees with the estimate of Box and Colgan26, with the Greenland ice sheet in near balance from 1980 to about 1996, after which it starts to lose mass (Figure 4.3). Therefore, we assume that between 1980 and 1996, freshwater flux from Greenland is approximately equal to accumulation; after 1996, freshwater flux from Greenland equals the sum of mass loss and accumulation (Figure 4.3). Since the accumulation is highly variable from year to year, we smooth it with a 5-year running mean. Figure 4 shows the resulting freshwater flux estimates from Greenland. This approach

yields freshwater flux estimates that agree with those of Bamber et al. (2012) during the period of data overlap, once a correction for solid ice discharge is applied⁸ (Figure 4.4). Freshwater from the CAA is approximated by ice and tundra runoff predicted by RACMO2.3 since ice discharge (0.16 mSv) is negligible (Gardner et al., 2011).

Large amounts of Arctic sea ice and freshwater are exported from the Arctic Ocean to the North Atlantic through several pathways. Of these, Fram Strait and the CAA are the major ones; nearly all (~98%) Arctic Ocean export drains through them (Haine et al., 2015). However, there are large uncertainties in these fluxes (Haine et al., 2015). We focus on changes in freshwater flux as inferred from recent accelerated melting of Arctic sea ice, assuming that the change is partitioned the same way as total export, i.e., 98% of the change is advected through Fram Strait and the CAA. Changes in the annual minimum of Arctic sea ice volume are a relevant indicator (see Methods and Appendix B). We first use the annual minimum volume predicted by the Pan-Arctic Ice Ocean Modeling and Assimilation System (PIOMAS) model (Zhang and Rothrock, 2003). We also apply the same method to the Arctic sea ice extent and sea ice area data sets (Fetterer et al., 2009), where “extent” defines a region as either “ice-covered” or “not ice-covered” using a threshold of 15%; “area” is a more conservative estimate, defined as the percentage of actual sea ice within a given data cell. We assume a standard ice thickness of 2 m (Laxon et al., 2003) to convert ice extent and ice area to volume, obtaining results that are somewhat smaller than the PIOMAS volume model. Figure 4.4 shows results from the PIOMAS volume model. Results from the other two approaches are shown in Figures A12 and A13.

Figure 4 also shows the summed result from these various freshwater sources (recall that this summed value does not include several major sources and is therefore a minimum estimate), which is our estimate of the freshwater flux into the sub-polar North Atlantic. Freshwater flux from Greenland is relatively stable from 1979 to the mid-late 1990s and then increases. Freshwater flux from the CAA is relatively stable until the early 2000s and then increases. Freshwater flux from Arctic sea ice increases mainly during the period 1990 to 2000. The total freshwater flux for the sub-polar North Atlantic from these

sources is about 60 mSv by 2013 with an increase of 20 mSv during the last two decades. Of this \sim 12 mSv comes from the Greenland ice sheet and CAA glaciers, while \sim 8 mSv represents excess melting of Arctic sea ice.

Focused freshwater flux into the Labrador Sea has the potential to disrupt the AMOC by increasing the buoyancy of surface waters and reducing the formation of dense, deep water (Stouffer et al., 2006). How much of the enhanced freshwater flux that we calculate actually winds up in the Labrador Sea?

Myers et al. (2009); Myers (2005) showed that a significant fraction of freshwater originating in and around Greenland is transported to the Labrador Sea: melt water from eastern Greenland is entrained in the East Greenland Current, where it moves south and merges with the Irminger Current as it rounds Cape Farewell; melt water from southwestern Greenland joins the West Greenland Current, similarly merging with the Irminger Current (Figure 4.1). Meltwater from the CAA enters the Labrador Sea through Davis and Hudson straits, either directly or indirectly (McGeehan and Maslowski, 2012). The pattern of boundary currents and eddy activity around Greenland and Labrador insures that at least 75 percent of the freshwater flux from the Greenland ice sheet and CAA eventually winds up in the Labrador Sea (Appendix B). Freshwater and sea ice drained from the Arctic Ocean moves south through Fram Strait and the CAA37, also contributing to freshening of the Labrador Sea both remotely and locally (Koenigk et al., 2006; Peterson et al., 2006). We estimate that at least 65 percent of freshwater and sea ice exported from the Arctic Ocean through Fram Strait and the CAA ultimately makes it to the Labrador Sea (Appendix B). Assuming these estimates are correct, of the 20 mSv freshwater flux increase that we estimate, at least 14mSv (70%) winds up in the Labrador Sea (Appendix B). Given typical coastal current velocities, most of this freshwater is transported to the Labrador Sea within 3 - 12 months. Some freshwater from the CAA may take 2 – 3 years to reach the Labrador Sea due to recirculation and storage in Baffin Bay and/or recirculation in the sub-polar gyre.

4.3.4 Impact of increased freshwater flux on deep water formation

To investigate effects of increased freshwater flux on deep water formation in the Labrador Sea, we can either look at the mean density of LSW within a given depth range, or look at the thickness of LSW as defined by a given density range. We used both approaches, obtaining similar results. Figure 4.5 shows results from the second approach, where we calculate the thickness of LSW, defined by kg m^{-3} , from 1950 to 2013, using the objective analyses of the EN4.0.2 data set from the UK Met Office Hadley Center (Good et al., 2013). The data set includes monthly temperature and salinity with a spatial resolution of $1^\circ \times 1^\circ$ and 42 depth intervals (5 m to 5350 m) from 1900 to present. Results for density over a fixed depth range (1000 m – 2500 m) are shown in Figure A15.

Figure 4.5 shows the time series of LSW thickness, compared to our estimate of freshwater flux and to the Irminger salt flux time series. From 1950 to the mid-1990s, Irminger salt flux and LSW thickness are weakly correlated ($R = 0.3$, $P = 0.03$), and both show multidecadal oscillations, with highs in the 1960s, lows in the 1980s, and highs in the 1990s. In particular, LSW thickness increased significantly (by 65%) between 1990 and 1995 when salt flux increased, consistent with the idea that dense deep water in the Labrador Sea originates from warm, saline North Atlantic water that subsequently experiences winter cooling. However, this relationship begins to break down in the mid-to-late 1990s, when freshwater flux from Greenland and other sources increased rapidly. Since then, LSW thickness decreased continuously, reaching lows not observed since the early 1970s, despite continued high salt flux. One interpretation of this is that increased freshwater flux has now overwhelmed increased salt flux from the Atlantic, and has begun to influence LSW formation. Recall that increased salt flux from the Atlantic is accompanied by increased heat flux (Figure 4.3) which promotes melting of marine-terminating outlet glaciers in southern Greenland (Holland et al., 2008; Rignot and Kanagaratnam, 2006), and increased freshwater flux.

Our data are consistent with recent studies showing a decline in the thickness of the dense mode of LSW since 1994/95, with a switch to a less dense and presumably fresher and warmer upper mode Rhein et al. (2011); Kieke and Yashayaev (2015). Yashayaev

et al. (2015) show declining upper salinity since the mid-2000s and suggest that salinity is the controlling factor for ocean stratification in this region. Declining upper layer salinity would weaken or even prevent Labrador Sea convection. However, cold winter air also plays a role in LSW formation. Severe winter conditions and strong air-sea heat exchange for the period 1990 – 1995 may have contributed to the increased LSW thickness (Lazier et al., 2002), while milder winter conditions and weaker cooling since 1995 may have contributed to LSW decline Vage et al. (2009). The Labrador Sea is also sensitive to multidecadal climate variations. Hydrographic properties in the Labrador Sea exhibit multidecadal variability that resemble the Atlantic Multidecadal Oscillation (AMO) and the North Atlantic Oscillation (NAO) (Yashayaev et al., 2015), and these variations are obvious in the flux (Figure 4.3) and LSW thickness (Figure 4.5) time series. Bidecadal variability in the Labrador Sea forced by volcanic activity has also been proposed (Swingedouw et al., 2015). Despite these complications, our data clearly show a steep, recent increase in freshwater flux into the Labrador Sea and a steep decline in LSW thickness (and density) at the same time (Figure 4.5), which is inconsistent with the estimated salt flux into the region. This suggests a potential impact on formation of North Atlantic Deep Water.

4.4 Discussion

Our reconstructed annual freshwater flux for the sub-polar North Atlantic reaches 60 mSv in 2013 with an increase of 20 mSv in the last two decades (Figure 4.4). At least 70 percent (14 mSv) of this increased freshwater is focused towards the Labrador Sea (Appendix B). This is a minimum estimate since we do not consider other major sources. LSW formation may reflect a delicate balance between this cold freshwater and warm, salty North Atlantic water from the Irminger Current. The flux of freshwater from Greenland may in turn be influenced by warm Atlantic water and its influence on the regional ocean and atmosphere, a potentially important feedback in the system.

Since LSW is an important component of the dense southward return flow of the AMOC, factors influencing LSW formation may in turn impact the AMOC. Hosing experiments show different sensitivities of the AMOC to freshwater fluxes at high

latitudes (Fichefet et al., 2003; Jungclaus et al., 2006; Stouffer et al., 2006; Hu et al., 2011; Swingedouw et al., 2013; Ridley et al., 2005; Brunnabend et al., 2015) 11-17. Hu et al. (2011) suggest that freshwater inputs much larger than we observe are required. On the other hand, Fichefet et al. (2003) suggest that freshwater flux anomalies as small as 15 mSv will affect the AMOC. Brunnabend et al. (2015) suggest that freshwater flux anomalies as small as 7 mSv applied over 30 years could impact the AMOC. Different model outcomes partly reflect their spatial resolution, the degree to which freshwater fluxes are focused towards the Labrador Sea, and the time scale over which anomalous flux is applied. Swingedouw et al. (2013) compared different model responses to freshwater release around Greenland, assuming freshwater focusing into the Labrador Sea. They show significant AMOC weakening after several decades with a flux anomaly of 100 mSv.

If our inference that the sub-polar gyre's coastal currents focus melt water from Greenland, CAA glaciers and Arctic sea ice into the Labrador Sea is correct, then present rates of increased freshwater flux may be sufficient to influence convection in the Labrador Sea and by implication the AMOC. Northward decreases in heat and salt flux across our three sections in southwest Greenland indicate strong mixing of coastal water and westward advection into the Labrador Sea. Eddy kinetic energy reaches a local maximum offshore Cape Desolation and Paamiut, where a front develops between Irminger Water and fresh shelf water, promoting baroclinic instability and eddy formation; these eddies propagate westward into the Labrador Sea. Local bathymetric structures, especially the sill at Davis Strait, also promote westward propagation of coastal water from southwestern Greenland. Recent high-resolution eddy permitting or eddy-resolving numerical models support this type of spatial focusing, and indicate decline or even shutdown of Labrador Sea convection with enhanced freshwater flux from Greenland (Weijer et al., 2012) or from the Arctic Ocean through the CAA (McGeehan and Maslowski, 2011). Since freshwater lenses can retain their integrity for some time, "temporal focusing" may also be important. Summer (June, July, August) freshwater fluxes from Greenland and CAA's ice and snow runoff greatly exceed the annual mean. Summer freshwater flux from Greenland and the

CAA increased by about 50 mSv from mid-late 1990s to 2013, reaching a high of 150 mSv in 2012 (Figure A16), potentially limiting convection during the subsequent winter.

We suggest that recent freshening in the vicinity of Greenland is reducing formation of dense LSW, potentially weakening the AMOC. Recent observations are beginning to document declines in the AMOC (Robson et al., 2013; Smeed et al., 2014; Rahmstorf et al., 2015), consistent with our hypothesis. Longer time series will be required to confirm this link, but our preliminary results suggest that detailed studies of Labrador Sea hydrography and proximal sources of freshwater, including Greenland, have the potential to improve our understanding of AMOC variability and sensitivity to anthropogenic warming.

4.5 Methods

4.5.1 GRACE data

The GRACE time series were created via the least squares inversion method described in Bonin and Chambers (2013). Release-05 GRACE data from the Center for Space Research (CSR) were used, with the standard post-processing applied as described in that paper: C20 is replaced by Satellite Laser Ranging (SLR) estimates, a geocenter model is added, GIA is corrected for, and the monthly averages of the Atmosphere and Ocean Dealiasing (AOD) product are restored.

The inversion technique is designed to localize the mass change signal, such that coastal mass loss from Greenland does not leak into the ocean or into interior Greenland due to GRACE's inherently low spatial resolution. Briefly, the method involves breaking Greenland and the surrounding area into pre-defined regions (Greenland drainage basins; Figure A17). Each region is assumed to have a uniform mass distribution when gridded as $1^\circ \times 1^\circ$ -binned kernels. The transformation to degree/order 60 spherical harmonics is then made upon each individual regional kernel, resulting in a smoothed version of each region that mimics what GRACE would see from its limited resolution, if a uniform mass of 1 was placed over the kernel, with zeroes elsewhere.

The goal is to find a set of multipliers for each region which most closely describes mass distribution over Greenland, given the assumption of uniform weights across each

pre-defined shape. A least squares method is used to fit an optimal multiplier to each basin simultaneously, such that the combination of the multipliers times the smoothed basin kernels best fits the actual (smoothed) GRACE data for that month. An optimal amount of process noise is added to stabilize the solution (Bonin and Chambers, 2013).

The GRACE mass balance in this paper is the sum of the individual signals from the 16 Greenland regions (Figure A17).

4.5.2 Irminger Water heat and salt flux analysis

Details of the data collection and analysis are discussed in Myers et al. (2007b) and summarized here. Prior to 1984 the estimates are based on a climatological analysis of the Labrador Sea. The 1984 – 2013 observations are collected on a set of standard sections by the Danish Meteorological Institute. Each section (Figure 4.1) involves the same 5 stations, but in some years only 3 or 4 stations could be occupied. The sections are occupied annually in most years, in late June or early July. Direct sampling using bottles was performed in 1984-87, while CTD (Conductivity-Temperature-Depth) data were collected in later years. We carry out our analysis on the upper 700 m, the deepest depth common to all years, binned on a 2 m vertical grid. For current motions, we determine the geostrophic velocity, relative to 700 dbar (\sim 700 m depth) or the bottom in shallower water, for each pair of stations at each depth, and add an estimate of the barotropic velocity (Myers et al., 2009). If data are missing, we do not include that point in the calculation. We calculate heat flux (Q_t) and salt flux (Q_s) at each depth and then sum those whose temperature and salinity are consistent with Irminger Water to obtain the total transport:

$$Q_t = \rho \cdot C_p \cdot \int_{s=1}^{s=5} \int_{z=-700}^{z=0} v(s, z) \cdot (T(s, z) - T_{\text{ref}}) dz ds \quad (4.1)$$

$$Q_s = \int_{s=1}^{s=5} \int_{z=-700}^{z=0} v(s, z) \cdot (S(s, z) - S_{\text{ref}}) dz ds \quad (4.2)$$

where ρ and C_p are ocean water density and heat capacity respectively, $v(s, z), T(s, z)$ and $S(s, z)$ are velocity, temperature and salinity in station s at depth z respectively, T_{ref} is

the reference temperature (0°C) and S_{ref} is the reference salinity(34.80). Here, we choose a broad definition including both pure and modified Irminger Water, with temperature warmer than 3.5°C and salinity higher than 34.88 (Myers et al., 2007b).

4.5.3 Freshwater flux

To estimate the freshwater flux from Greenland, we first use a simple constant acceleration model to fit the monthly GRACE mass balance data:

$$M(t_i) = a + bt_i + \frac{1}{2}ct_i^2 \quad (4.3)$$

where $M(t_i)$ ($i=1,2,3\dots n$) are GRACE monthly solutions, a is the initial mass of Greenland, b is the initial mass balance, and c is the acceleration term. Given the estimated parameters, the mass balance (MB) of Greenland can be represented by:

$$MB(t_i) = b + ct_i \quad (4.4)$$

The start time of recent accelerated mass loss is the time t_i when $MB(t_i)$ is zero. The mass balance of Greenland is:

$$MB = SMB - D \quad (4.5)$$

where SMB is surface mass balance and D is discharge, related to freshwater flux (FWF) by:

$$SMB = A - R \quad (4.6)$$

$$FWF = R + D \quad (4.7)$$

where A is the accumulation and R is runoff.

We then calculate freshwater flux from Greenland using the above relations, rewriting them as:

$$FWF = A - MB \quad (4.8)$$

where accumulation (A) is predicted by RACMO2.3 and mass balance (MB) is estimated from the GRACE data. Note that accumulation is defined over ice and tundra and mass

balance is the total mass balance of Greenland, including ice and tundra. Therefore, freshwater flux from Greenland is composed of ice mass loss and tundra runoff (Figure A18). Mass balance is considered equal to zero prior to the recent acceleration phase, beginning in 1996. Since mass balance is the long-term average, accumulation is smoothed with 5-year running average.

For the CAA, we assume $FWF = R$ when estimating freshwater flux since ice discharge from the CAA is negligible compared to runoff (Gardner et al., 2011). Thus, freshwater flux from the CAA is derived from runoff predicted by RACMO2.3. Note that both ice runoff and tundra runoff are considered in the freshwater flux calculation (Figure A19).

For Arctic sea ice, we focus just on recent accelerated melting of multi-year ice, which results in loss of ice area and extent, rather than the much larger contribution from the annual freeze-thaw cycle, which forms significant freshwater through fractionation (Appendix B), but is more difficult to quantify with remote methods. We use three data sets (area, extent and volume; see Appendix B and Figure A12) to estimate freshwater flux from accelerated melting of Arctic sea ice. All three approaches give similar results (Figure A13). The one based on volume is shown in Figure 4.4. To convert area and extent to mass, we assume sea ice thickness is 2 m (Laxon et al., 2003) and sea ice density is 900 kg m^{-3} . Annual melting of Arctic sea ice is estimated by fitting annual minimum Arctic sea ice mass estimates with a linear state space model (Appendix B).

4.6 Acknowledgements

West Greenland Current data were provided by the Danish Meteorological Institute (DMI), as well as the Greenland Institute of Natural Resource (GINR) for more recent years. We thank three anonymous reviewers for their insightful comments. This research was funded by NASA grants to THD and DC.

4.7 References

- Bamber, J., van den Broeke, M., Ettema, J., Lenaerts, J., and Rignot, E. (2012). Recent large increases in freshwater fluxes from greenland into the north atlantic. *Geophysical Research Letters*, 39(19):L19501.
- Bonin, J. and Chambers, D. (2013). Uncertainty estimates of a grace inversion modelling technique over greenland using a simulation. *Geophysical Journal International*, 194(1):212–229.
- Box, J. E. and Colgan, W. (2013). Greenland ice sheet mass balance reconstruction. part iii: marine ice loss and total mass balance (1840–2010). *Journal of Climate*, 26(18):6990–7002.
- Broecker, W. S. (1987). Unpleasant surprises in the greenhouse? *Nature*, 328:123–126.
- Broecker, W. S., Peteet, D. M., and Rind, D. (1985). Does the ocean-atmosphere system have more than one stable mode of operation. *Nature*, 315(6014):21–26.
- Brunnabend, S. E., Schröter, J., Rietbroek, R., and Kusche, J. (2015). Regional sea level change in response to ice mass loss in greenland, the west antarctic and alaska. *Journal of Geophysical Research-Oceans*, 120:doi: 10.1002/2015JC011244.
- Castro de la Guardia, L., Hu, X. M., and Myers, P. G. (2015). Potential positive feedback between greenland ice sheet melt and baffin bay heat content on the west greenland shelf. *Geophysical Research Letters*, 42(12):4922–4930.
- Curry, B., Lee, C. M., Petrie, B., Moritz, R. E., and Kwok, R. (2014). Multiyear volume, liquid freshwater, and sea ice transports through davis strait, 2004-10*. *Journal of Physical Oceanography*, 44(4):1244–1266.
- Enderlin, E. M., Howat, I. M., Jeong, S., Noh, M.-J., van Angelen, J. H., and van den Broeke, M. R. (2014). An improved mass budget for the greenland ice sheet. *Geophysical Research Letters*, 41(3):866–872.

- Ettema, J., van den Broeke, M. R., van Meijgaard, E., van de Berg, W. J., Bamber, J. L., Box, J. E., and Bales, R. C. (2009). Higher surface mass balance of the greenland ice sheet revealed by high-resolution climate modeling. *Geophysical Research Letters*, 36(12):L12501.
- Fetterer, F., Knowles, K., Meier, W., and Savoie, M. (2002, updated daily). Sea ice index. pages National Snow and Ice Data Center, Boulder, Colorado.
- Fichefet, T., Poncin, C., Goosse, H., Huybrechts, P., Janssens, I., and Le Treut, H. (2003). Implications of changes in freshwater flux from the greenland ice sheet for the climate of the 21st century. *Geophysical Research Letters*, 30(17):1911.
- Gardner, A. S., Moholdt, G., Wouters, B., Wolken, G. J., Burgess, D. O., Sharp, M. J., Cogley, J. G., Braun, C., and Labine, C. (2011). Sharply increased mass loss from glaciers and ice caps in the canadian arctic archipelago. *Nature*, 473(7347):357–360.
- Good, S. A., Martin, M. J., and Rayner, N. A. (2013). En4: Quality controlled ocean temperature and salinity profiles and monthly objective analyses with uncertainty estimates. *Journal of Geophysical Research-Oceans*, 118(12):6704–6716.
- Haine, T. W. N., Curry, B., Gerdes, R., Hansen, E., Karcher, M., Lee, C., Rudels, B., Spreen, G., de Steur, L., Stewart, K. D., and Woodgate, R. (2015). Arctic freshwater export: status, mechanisms, and prospects. *Global and Planetary Change*, 125:13–35.
- Hawkins, E., Smith, R. S., Allison, L. C., Gregory, J. M., Woollings, T. J., Pohlmann, H., and de Cuevas, B. (2011). Bistability of the atlantic overturning circulation in a global climate model and links to ocean freshwater transport. *Geophysical Research Letters*, 38:L10605.
- Holland, D. M., Thomas, R. H., de Young, B., Ribergaard, M. H., and Lyberth, B. (2008). Acceleration of jakobshavn isbrae triggered by warm subsurface ocean waters. *Nature Geoscience*, 1(10):659–664.
- Howat, I. M. and Eddy, A. (2011). Multi-decadal retreat of greenland’s marine-terminating glaciers. *Journal of Glaciology*, 57(203):389–396.

- Hu, A. X., Meehl, G. A., Han, W. Q., and Yin, J. J. (2011). Effect of the potential melting of the greenland ice sheet on the meridional overturning circulation and global climate in the future. *Deep-Sea Research Part Ii-Topical Studies in Oceanography*, 58(17-18):1914–1926.
- Jakobsen, P. K., Ribergaard, M. H., Quadfasel, D., Schmitt, T., and Hughes, C. W. (2003). Near-surface circulation in the northern north atlantic as inferred from lagrangian drifters: variability from the mesoscale to interannual. *Journal of Geophysical Research-Oceans*, 108(C8):3251.
- Jiang, Y., Dixon, T. H., and Wdowinski, S. (2010). Accelerating uplift in the north atlantic region as an indicator of ice loss. *Nature Geoscience*, 3(6):404–407.
- Josey, S. A. and Marsh, R. (2005). Surface freshwater flux variability and recent freshening of the north atlantic in the eastern subpolar gyre. *Journal of Geophysical Research-Oceans*, 110(C5):C05008.
- Joughin, I., Alley, R. B., and Holland, D. M. (2012). Ice-sheet response to oceanic forcing. *Science*, 338(6111):1172–6.
- Joyce, T. M. and Proshutinsky, A. (2007). Greenland’s island rule and the arctic ocean circulation. *Journal of Marine Research*, 65(5):639–653.
- Jungclaus, J. H., Haak, H., Esch, M., Roeckner, E., and Marotzke, J. (2006). Will greenland melting halt the thermohaline circulation? *Geophysical Research Letters*, 33(17):L17708.
- Kieke, D. and Yashayaev, I. (2015). Studies of labrador sea water formation and variability in the subpolar north atlantic in the light of international partnership and collaboration. *Progress in Oceanography*, 132:220–232.
- Koenigk, T., Mikolajewicz, U., Haak, H., and Jungclaus, J. (2006). Variability of fram strait sea ice export: causes, impacts and feedbacks in a coupled climate model. *Climate Dynamics*, 26(1):17–34.

- Kuhlbrodt, T., Titz, S., Feudel, U., and Rahmstorf, S. (2001). A simple model of seasonal open ocean convection. *Ocean Dynamics*, 52(1):36–49.
- Laxon, S., Peacock, N., and Smith, D. (2003). High interannual variability of sea ice thickness in the arctic region. *Nature*, 425(6961):947–950.
- Lazier, J., Hendry, R., Clarke, A., Yashayaev, I., and Rhines, P. (2002). Convection and restratification in the labrador sea, 1990-2000. *Deep Sea Research Part I: Oceanographic Research Papers*, 49(10):1819–1835.
- Lenaerts, J. T. M., van Angelen, J. H., van den Broeke, M. R., Gardner, A. S., Wouters, B., and van Meijgaard, E. (2013). Irreversible mass loss of canadian arctic archipelago glaciers. *Geophysical Research Letters*, 40(5):870–874.
- McGeehan, T. and Maslowski, W. (2011). Impact of shelf basin freshwater transport on deep convection in the western labrador sea. *Journal of Physical Oceanography*, 41(11):2187–2210.
- McGeehan, T. and Maslowski, W. (2012). Evaluation and control mechanisms of volume and freshwater export through the canadian arctic archipelago in a high-resolution pan-arctic ice-ocean model. *Journal of Geophysical Research*, 117:C00D14.
- Myers, P. G. (2005). Impact of freshwater from the canadian arctic archipelago on labrador sea water formation. *Geophysical Research Letters*, 32(6):L06605.
- Myers, P. G., Donnelly, C., and Ribergaard, M. H. (2009). Structure and variability of the west greenland current in summer derived from 6 repeat standard sections. *Progress in Oceanography*, 80(1-2):93–112.
- Myers, P. G., Josey, S. A., Wheler, B., and Kulan, N. (2007a). Interdecadal variability in labrador sea precipitation minus evaporation and salinity. *Progress in Oceanography*, 73(3-4):341–357.
- Myers, P. G., Kulan, N., and Ribergaard, M. H. (2007b). Irminger water variability in the west greenland current. *Geophysical Research Letters*, 34(17):L17601.

- Noël, B., van de Berg, W. J., van Meijgaard, E., Kuipers Munneke, P., van de Wal, R. S. W., and van den Broeke, M. R. (2015). Summer snowfall on the greenland ice sheet: a study with the updated regional climate model racmo2.3. *The Cryosphere Discussions*, 9(1):1177–1208.
- Peterson, B. J., Holmes, R. M., McClelland, J. W., Vorosmarty, C. J., Lammers, R. B., Shiklomanov, A. I., Shiklomanov, I. A., and Rahmstorf, S. (2002). Increasing river discharge to the arctic ocean. *Science*, 298(5601):2171–2173.
- Peterson, B. J., McClelland, J., Curry, R., Holmes, R. M., Walsh, J. E., and Aagaard, K. (2006). Trajectory shifts in the arctic and subarctic freshwater cycle. *Science*, 313(5790):1061–1066.
- Rahmstorf, S. (1995). Bifurcations of the atlantic thermohaline circulation in response to changes in the hydrological cycle. *Nature*, 378(6553):145–149.
- Rahmstorf, S., Box, J. E., Feulner, G., Mann, M. E., Robinson, A., Rutherford, S., and Schaffernicht, E. J. (2015). Exceptional twentieth-century slowdown in atlantic ocean overturning circulation. *Nature Climate Change*, 5(5):475–480.
- Rahmstorf, S., Crucifix, M., Ganopolski, A., Goosse, H., Kamenkovich, I., Knutti, R., Lohmann, G., Marsh, R., Mysak, L. A., Wang, Z. M., and Weaver, A. J. (2005). Thermohaline circulation hysteresis: A model intercomparison. *Geophysical Research Letters*, 32(23):L23605.
- Rhein, M., Kieke, D., Hutt-Kabus, S., Roessler, A., Mertens, C., Meissner, R., Klein, B., Boning, C. W., and Yashayaev, I. (2011). Deep water formation, the subpolar gyre, and the meridional overturning circulation in the subpolar north atlantic. *Deep-Sea Research Part II:Topical Studies in Oceanography*, 58(17-18):1819–1832.
- Ridley, J. K., Huybrechts, P., Gregory, J. M., and Lowe, J. A. (2005). Elimination of the greenland ice sheet in a high co2 climate. *Journal of Climate*, 18(17):3409–3427.
- Rignot, E. and Kanagaratnam, P. (2006). Changes in the velocity structure of the greenland ice sheet. *Science*, 311(5763):986–990.

- Rignot, E., Velicogna, I., van den Broeke, M. R., Monaghan, A., and Lenaerts, J. T. M. (2011). Acceleration of the contribution of the greenland and antarctic ice sheets to sea level rise. *Geophysical Research Letters*, 38(5):L05503.
- Robson, J., Hodson, D., Hawkins, E., and Sutton, R. (2013). Atlantic overturning in decline? *Nature Geoscience*, 7(1):2–3.
- Rooth, C. (1982). Hydrology and ocean circulation. *Progress in Oceanography*, 11(2):131–149.
- Smeed, D. A., McCarthy, G. D., Cunningham, S. A., Frajka-Williams, E., Rayner, D., Johns, W. E., Meinen, C. S., Baringer, M. O., Moat, B. I., Duchez, A., and Bryden, H. L. (2014). Observed decline of the atlantic meridional overturning circulation 2004–2012. *Ocean Sci.*, 10(1):29–38.
- Stommel, H. (1961). Thermohaline convection with two stable regimes of flow. *Tellus*, 13(2):224–230.
- Stouffer, R. J., Yin, J., Gregory, J. M., Dixon, K. W., Spelman, M. J., Hurlin, W., Weaver, A. J., Eby, M., Flato, G. M., Hasumi, H., Hu, A., Jungclaus, J. H., Kamenkovich, I. V., Levermann, A., Montoya, M., Murakami, S., Nawrath, S., Oka, A., Peltier, W. R., Robitaille, D. Y., Sokolov, A., Vettoretti, G., and Weber, S. L. (2006). Investigating the causes of the response of the thermohaline circulation to past and future climate changes. *Journal of Climate*, 19(8):1365–1387.
- Straneo, F. and Heimbach, P. (2013). North atlantic warming and the retreat of greenland’s outlet glaciers. *Nature*, 504(7478):36–43.
- Swingedouw, D., Ortega, P., Mignot, J., Guilyardi, E., Masson-Delmotte, V., Butler, P. G., Khodri, M., and Seferian, R. (2015). Bidecadal north atlantic ocean circulation variability controlled by timing of volcanic eruptions. *Nature Communications*, 6:6545.
- Swingedouw, D., Rodehacke, C., Behrens, E., Menary, M., Olsen, S., Gao, Y., Mikolajewicz, U., Mignot, J., and Biastoch, A. (2013). Decadal fingerprints of freshwater dis-

charge around greenland in a multi-model ensemble. *Climate Dynamics*, 41(3-4):695–720.

Thierry, V., de Boisséson, E., and Mercier, H. (2008). Interannual variability of the subpolar mode water properties over the reykjanes ridge during 1990–2006. *Journal of Geophysical Research*, 113(C4):C04016.

Vage, K., Pickart, R. S., Thierry, V., Reverdin, G., Lee, C. M., Petrie, B., Agnew, T. A., Wong, A., and Ribergaard, M. H. (2009). Surprising return of deep convection to the subpolar north atlantic ocean in winter 2007-2008. *Nature Geoscience*, 2(1):67–72.

Velicogna, I., Sutterley, T., and van den Broeke, M. (2014). Regional acceleration in ice mass loss from greenland and antarctica using grace time-variable gravity data. *Geophysical Research Letters*, 41(22):8130–8137.

Weijer, W., Maltrud, M. E., Hecht, M. W., Dijkstra, H. A., and Kliphus, M. A. (2012). Response of the atlantic ocean circulation to greenland ice sheet melting in a strongly-eddying ocean model. *Geophysical Research Letters*, 39:L09606.

Wood, R. A., Keen, A. B., Mitchell, J. F. B., and Gregory, J. M. (1999). Changing spatial structure of the thermohaline circulation in response to atmospheric co₂ forcing in a climate model. *Nature*, 401(6752):508–508.

Yang, Q., Dixon, T. H., and Wdowinski, S. (2013). Annual variation of coastal uplift in greenland as an indicator of variable and accelerating ice mass loss. *Geochemistry Geophysics Geosystems*, 14(5):1569–1589.

Yashayaev, I. and Loder, J. W. (2009). Enhanced production of labrador sea water in 2008. *Geophysical Research Letters*, 36(1):L01606.

Yashayaev, I., Seidov, D., and Demirov, E. (2015). A new collective view of oceanography of the arctic and north atlantic basins. *Progress in Oceanography*, 132:1–21.

Zhang, J. L. and Rothrock, D. A. (2003). Modeling global sea ice with a thickness and enthalpy distribution model in generalized curvilinear coordinates. *Monthly Weather Review*, 131(5):845–861.

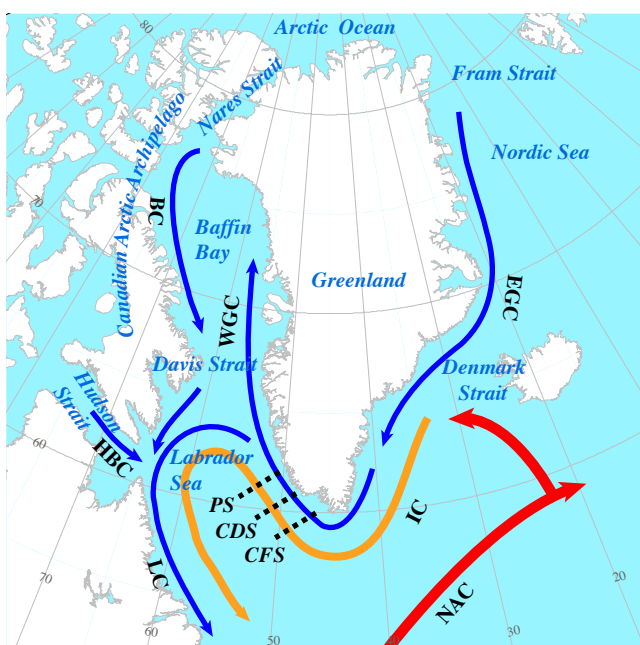


Figure 4.1: Study region showing oceanographic sections and major currents around Greenland. Red and orange arrows indicate Atlantic-origin water, blue arrows indicate Arctic-origin water. NAC is North Atlantic Current; IC is Irminger Current; EGC is East Greenland Current; WGC is West Greenland Current; BC is Baffin Current; HBC is Hudson's Bay Current; LC is Labrador Current; CFS is Cape Farewell Section; CDS is Cape Desolation Section; PS is Paamiut Section. 3-D structure of major water masses in the Labrador Sea is shown in Figure A8.

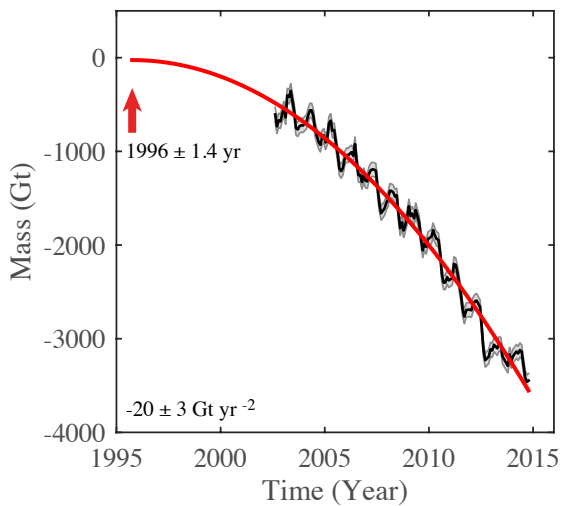


Figure 4.2: Mass change of Greenland estimated from GRACE for the period 2002 - 2014. Black curve shows data, grey shading indicates monthly uncertainty, and red curve shows the best fitting constant acceleration model. Onset time of acceleration defined when rate of mass change is zero, in 1996 (red arrow), with mass arbitrarily set to zero.

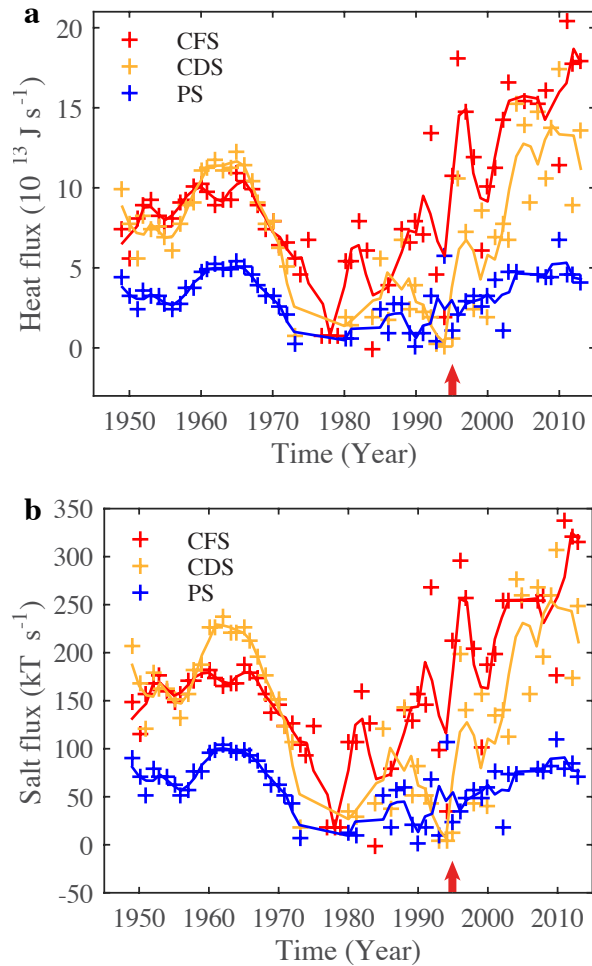


Figure 4.3: Heat and salt fluxes of Irminger Water for the period 1949 – 2013. (a) Heat and (b) salt fluxes of Irminger Water are measured at three sections in southwest Greenland. Locations of three sections are shown in Figure 4.1. CFS is Cape Farewell Section; CDS is Cape Desolation Section; PS is Paamiut Section. Solid line represents a 3-year running average, yearly data shown by plus signs. Red arrow marks the onset time of accelerated mass loss for Greenland estimated from GRACE (Figure 4.2).

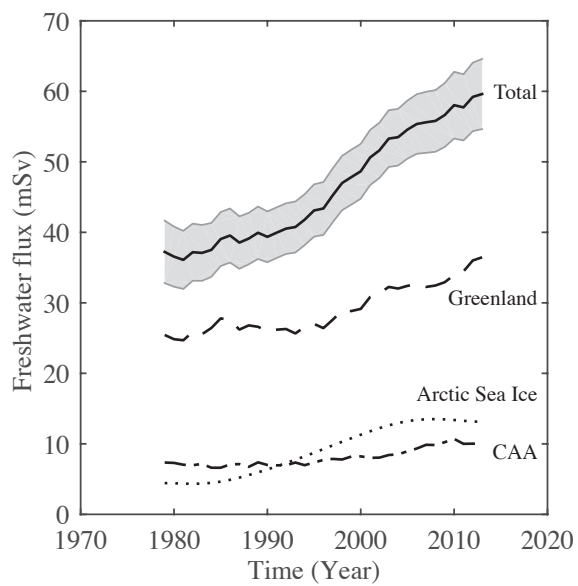


Figure 4.4: Freshwater flux from Greenland and CAA and Arctic sea ice for the period 1979 – 2013. For Arctic sea ice, we plot only changes in flux (see text). The sum of these sources (“Total”) is also plotted. Grey shading indicates propagated uncertainty (see Appendix B).

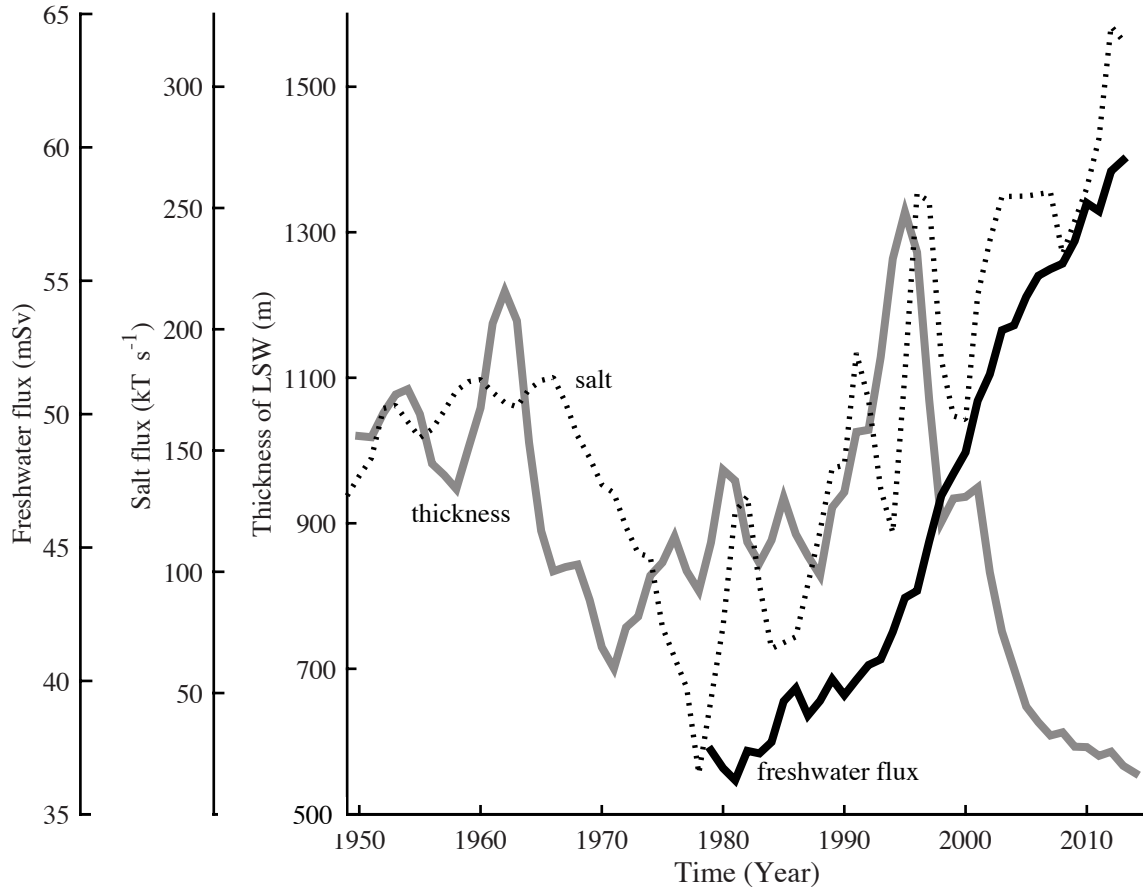


Figure 4.5: Thickness of LSW and total freshwater flux and salt flux of Irminger Water. Grey solid line indicates thickness of LSW, black solid line indicates total freshwater flux, and dotted line indicates salt flux of Irminger Water. Thickness and salt flux are smoothed with a 3-year running mean. Thickness is obtained from the objective analysis of EN4.0.2 dataset from the UK Met Office Hadley Center (Good et al., 2013). Thickness is averaged over 50° N - 65° N and 38° W - 65° W. Expression of salt flux in terms of freshwater flux is shown in Figure A14.

5. InSAR Monitoring of Ground Deformation Due to CO₂ injection at an Enhanced Oil Recovery Site, West Texas³

5.1 Abstract

Interferometric Synthetic Aperture Radar (InSAR) measurements have been used to measure ground deformation associated with fluid injection/production at an Enhanced Oil Recovery (EOR) field in Scurry County, West Texas. 100 million tons (Mt) of supercritical CO₂ have been sequestered here since 1972, of which about half has been sequestered since 2004. InSAR data show surface uplift up to 10 cm in the field between January 2007 and March 2011. We evaluated data concerning injection and production of CO₂, water, oil and hydrocarbon gas from 2004 to 2011 to investigate causes of the observed uplift. An analytical model is used to calculate reservoir pressure change and surface displacement. Our simulations show up to 10 MPa pressure buildup in the reservoir over four years of net injection and production. Surface displacement predictions agree well with the InSAR observations. Water injection alone cannot explain the 2007 – 2011 surface uplift because the net injected water (\sim 1 Mt) is negligible compared to the net injected CO₂ (\sim 24 Mt). The predicted total pressure buildup (up to 10 MPa) consists of net CO₂ injection (up to 12 MPa), net water injection (up to 2 MPa), and oil and gas production (up to -0.4 MPa). Hence, observed ground uplift was mainly caused by CO₂ injection.

5.2 Introduction

An important aspect of large-scale Carbon Capture, Utilization and Storage (CCUS) is the ability to assess the fate of injected CO₂ and test for leakage. These so-called Monitoring, Verification and Accounting (MVA) activities typically involve active

³This chapter has been reprinted from the International Journal of Greenhouse Gas Control with permission as: Yang, Q., Zhao, W. L., Dixon, T. H., Amelung, F., Han, W. S., Li, P., (2015), InSAR Monitoring of Ground Deformation Due to CO₂ injection at an Enhanced Oil Recovery Site, West Texas, Int. J. Greenhouse Gas Control, 41, 20-28. Copyright 2015 by Elsevier. doi:10.1016/j.ijggc.2015.06.016.

seismic surveys and down-hole techniques for precise tracking of CO₂ plume migration, both of which can be expensive. Since the economic viability of CCUS is impacted by the cost of MVA activities, development of lower cost approaches is desirable.

Injection of CO₂ or other fluid into a reservoir at depth increases fluid pressure in the reservoir, causing deformation in the overlying strata and inducing surface deformation. If the pressure change is large enough, the surface deformation may be measurable. In principle, the measured surface deformation can be inverted to estimate pressure changes at depth and track the CO₂ plume (e.g., Vasco et al., 2008, 2010; Rinaldi and Rutqvist, 2013; White et al., 2014; Karegar et al., 2015). Over long periods (decades or centuries), chemical reactions that result in formation of mineral phases will cause pressure and volume reduction and subsidence, and could not be distinguished from migration or leakage with this technique alone. On the other hand, surface deformation can be measured at relatively low cost, the interpretation is relatively straightforward, and the technique gives useful information in the critical few years immediately following injection.

Enhanced Oil Recovery (EOR) refers to techniques for increasing the amount of oil extracted at depleted or high viscosity oil fields. CO₂-Enhanced Oil Recovery (CO₂-EOR) has been used by the oil and gas industry for over 40 years (Orr and Taber, 1984), but only recently has its potential as a promising method of carbon sequestration been realized and investigated (Bryant et al., 2007). Considering the potential of CO₂-EOR for implementation of large-scale carbon emission reduction (Metz et al., 2005), it is important to test surface deformation MVA techniques in a CO₂-EOR field.

Interferometric Synthetic Aperture Radar (InSAR) technique has been successfully used to monitor surface deformation associated with CO₂ injection at the In Salah field in Algeria (Mathias et al., 2009a; Morris et al., 2011; Shi et al., 2012; Verdon et al., 2013). In this paper, we use InSAR to study surface deformation associated with a CO₂-EOR project in West Texas. We use an analytical model and historical injection and production data to estimate CO₂ plume extent and reservoir pressure change constrained by surface deformation observations. The study reveals that ground uplift between January 2007

and March 2011 is mainly caused by CO₂ injection. The maximum pressure change due to net injection and production of CO₂, water, oil and hydrocarbon gas is up to 10 MPa.

5.3 Study area description

The CO₂-EOR field is located in Scurry County, West Texas (Figure 5.1). The reservoir is the southeastern segment of the Horseshoe Atoll play within the Midland basin, one of the largest subsurface limestone reef mounds in the world (Galloway et al., 1983). It is a chain of oil fields with the major one being the Kelly-Snyder field. The producing zones are Pennsylvanian-aged Cisco and Canyon formations, and are comparable to a large class of potential brine storage reservoirs. Average depth of the producing zones is 2000 m (Vest Jr, 1970; Raines and Dobitz, 2001) with average reservoir pressures of 16 MPa and a temperature of 41.5 °C (Raines, 2005). The rock formation porosity (0 – 22.5%) and permeability (0.1 md – 1760 md) are described in Raines (2005). The reported average porosity and permeability are 9.8% and 19 mD respectively. Overlying the producing zone is the Permian-aged Wolfcamp formation, providing a very low permeability seal above the Cisco and Canyon Groups. The physical properties of the field make it a good candidate for CO₂-EOR as well as CO₂ sequestration.

Three production phases occurred in the oil field after it was discovered in 1948 (Figure 5.2). The primary recovery phase was 1948 – 1951. During this phase, 5 percent of original oil in place (2.73 billion barrels) was produced by the solution gas driven mechanism, resulting in decline of the original reservoir pressure by 50 percent, from 21.5 MPa to 11.4 MPa (Dicharry et al., 1973; Brummett Jr et al., 1976). The secondary recovery phase began in 1954. During this phase, water-flooding technology was used to produce oil and maintain reservoir pressure. 133 MCM (Million Cubic Meters) of water was injected into the reservoir, and reservoir pressure increased from 11.4 MPa to 16.2 MPa. However, after 17 years of water injection, over 40 percent of original oil in place was still left in the reservoir.

The tertiary/enhanced oil recovery phase started in 1972 (Crameik et al., 1972). During this phase, CO₂ was injected continuously into the reservoir to increase oil production. From 1972 to 2003, the CO₂ monthly injection rate was quite stable, with a

mean value of 0.28 MCM per month. The CO₂ injection rate has increased since 2004. The mean value of the CO₂ monthly injection rate in 2004 – 2011 was about six times higher compared to 1972 – 2003. Although water was also injected into the unit during the third phase, the sequestered water was small compared to the sequestered CO₂ since injected and produced volumes of water are approximately equal (Figure 5.2). Raines (2005) suggested that approximately 55 Mt (70 MCM) of CO₂ was sequestered in the reservoir from 1972 to 2005 based on a simple mass-balance model. Our study updates the injection and production data sets to 2011, and suggests that about 100 Mt (128 MCM) of CO₂ were sequestered in the reservoir from 1972 to 2011, with about 50 percent accumulated from 2004 to 2011. Note that in this paper, all the volume numbers are reported at the reservoir depth with pressure equal to 16 MPa and temperature equal to 41.5 °C.

5.4 Observed ground deformation

Advanced Land Observing Satellite (ALOS) image data from the Japan Aerospace Exploration Agency (JAXA) are used to monitor surface displacement above the CO₂-EOR field. The satellite repeat cycle is 46 days. Thirteen images were acquired from January 08, 2007 to March 06, 2011 on ascending path 184, frame 640, from which 53 interferograms were generated. The small Baseline Subset technique (Berardino et al., 2002) is applied to generate displacement time series. By using L-band SAR data, the interferometric phase tends to remain coherent even in vegetated areas. To reduce errors caused by phase unwrapping, we use the temporal coherence method (Pepe and Lanari, 2006) to mask out pixels with unwrapping error. SRTM version 4 (Reuter et al., 2007) 3 arc second DEM data were interpolated to 1 arc second (\sim 30 m) resolution to remove topographic effects (Figure 5.3).

A total displacement of up to \sim 10 cm LOS (line of sight) is detected (Figure 5.1a). Note that part of the oil field is not covered by our interferograms. No active injection or production occurred in this section during the InSAR observation period (discussed in section 5.5.3, Figure 5.5). Thus, we expect only moderate displacement here associated with nearby injection and production activity.

Figure 5.4a shows time series of LOS displacement at Snyder, Texas (red star marked in Figure 5.1). Increasing LOS displacement is observed from 2007 to 2011 when the cumulative volume of sequestered CO₂ increased. From 2007 to 2011, about 31 MCM (~24 Mt) CO₂ is stored in the reservoir, significantly larger than the amount of stored water (~ MCM/1 Mt) (Figure 5.4b), suggesting that the observed surface uplift is mainly caused by CO₂ injection.

5.5 Simulation

5.5.1 Analytical solution for ground displacement

An analytical solution for ground displacement associated with injection or withdrawal of fluid at depth may be derived in two steps: a) the approximate solution for reservoir pressure change due to fluid injection (Mathias et al., 2009a,b) and production (Theis, 1935); and b) the solution for surface deformation due to pressure change in depth estimated in an elastic half space (Xu et al., 2012).

First, we calculate the reservoir pressure change field due to fluid injection. Here, the approximate solution of Mathias et al. (2009a) is adopted to calculate pressure buildup due to injection of CO₂ in rock formations with large spatial extent. This solution is derived using the method of matched asymptotic expansions and accounts for two-phase Forchheimer flow (supercritical CO₂ and water), allowing for slight compressibility of fluid and rock formation. We also use the solution of Mathias to calculate pressure buildup due to water injection. Note that the Mathias solution reduces to the Theis (1935) solution for calculating pressure change due to water injection (single-phase flow) (Mathias et al., 2009a). We adopt the Theis solution to estimate pressure decline caused by fluid extraction (oil, hydrocarbon gas, water and CO₂). Theis (1935) provides a simplified model to estimate pressure drawdown due to pumping in a homogeneous, isotropic and infinite areal extent reservoir. We apply the Mathias solution to each injection well and calculate pressure change field caused by CO₂ injection and water injection respectively. Note that for wells injecting both CO₂ and water, we calculate the induced pressure buildup separately regardless of the mixing nature. As with pressure change due to injection, we apply the Theis equation to calculate pressure change field

caused by pumping of each type of fluid (oil, hydro-carbon gas, water and CO₂) at every individual production well. In summary, in this step we estimate a pressure change field caused by every single fluid element injected/extracted at an individual well, in preparation for surface displacement calculation in the next step.

Here we summarize the main formulations of the analytical solution for pressure buildup $P_{inj}(r, t)$ at radial distance r (note that x is dependent on r) and time t due to fluid (CO₂/water) injection (Mathias et al., 2009a) (equation 5.1-5.2) and the Theis solution for pressure drawdown $P_{pro}(r, t)$ due to fluid (CO₂/water/oil/HC gas) production (eq. 5.3).

$$P_{inj}(r, t) = P_0 \left\{ \frac{1}{2\gamma} Ei\left(\frac{\alpha x}{4\gamma}\right) + \frac{1}{2\gamma} (\ln(\frac{\alpha x}{4\gamma}) + 0.5772) \right\} \\ + P_0 \begin{cases} -\frac{1}{2} \ln(\frac{x}{2\gamma}) - 1 + \frac{1}{\gamma} - \frac{1}{\gamma} (\ln(\frac{\alpha x}{2\gamma^2}) + 0.5772) & x \leq 2\gamma \\ -\left(\frac{x}{2\gamma}\right)^{0.5} + \frac{1}{\gamma} - \frac{1}{2\gamma} (\ln(\frac{\alpha x}{2\gamma^2}) + 0.5772) & 2\gamma \leq x \leq \frac{2}{\gamma} \\ -\frac{1}{2\gamma} (\ln(\frac{\alpha x}{4\gamma}) + 0.5772) & x \geq \frac{2}{\gamma} \end{cases} \quad (5.1)$$

where: Ei is the exponential integral operator.

$$P_0 = \frac{Q_m \mu_f}{2\pi H \rho_f \kappa} \\ \gamma = \frac{\mu_f}{\mu_{brine}} \\ x = \frac{(r/r_w)^2}{t Q_m / (2\pi \omega H (r_w)^2 \rho_f)} \\ \alpha = \frac{Q_m \mu_f (c_{rock} + c_{brine})}{2\pi H \kappa} \quad (5.2)$$

where: r is the radial distance to injection well (m); r_w is the injector well radius, and we use $r_w = 0.1 m$ for our calculation; ρ_f is the density of injected fluid (kg/m^3); μ_f is the viscosity of injected fluid ($Pa \cdot s$); Q_m is the mass injection rate (kg/s); t is the injection time (s); c_{rock} is the formation compressibility (Pa^{-1}); κ is the formation permeability (m^2); μ_{brine} is the brine compressibility (Pa^{-1}); H is the formation thickness (m).

$$P_{pro}(r, t) = -\frac{Q_\nu \mu_f}{4\pi\kappa H} Ei\left(-\frac{\mu_f(\phi c_f + c_{rock})r^2}{4\kappa t}\right) \quad (5.3)$$

where: Q_ν is the volume injection rate (m^3/s); μ_f is the viscosity of produced fluid ($Pa \cdot s$); c_f is the compressibility of produced fluid (Pa^{-1}); ϕ is the formation porosity; other parameters are the same as in equation 5.1 and equation 5.2. Values of those parameters used in computing the pressure change are listed in Table 5.1 - 5.2.

Second, given the calculated fluid pressure field, we then calculate induced surface displacement. Xu et al. (2012) provide an analytical elastic solution for displacement in a half space forced by an arbitrary pressure distribution in the reservoir. Since the pressure caused by injection/production at individual well can be approximated as radial distribution, we first use Xu's solution to estimate surface displacement centered at each well according to the radial distributed pressure field of that well. Then, surface displacement of each well is linearly summed up to get the total surface displacement field due to all injection and production activities.

The main formulations of the analytical solution for vertical displacement $u_z(r)$ and horizontal displacement $u_r(r)$ at the radial distance r at the free surface results from the cumulative contribution of all the rings of dilation at radius r_0 and depth z' (xu2012fluid).

$$\begin{aligned} u_z(r) &= -\frac{2(1+\nu)(1-2\nu)}{\pi E} \iiint_{00Z_1}^{\infty\pi Z_2} \frac{p(r_0, t)z'}{(z'^2 + r^2 + r_0^2 - 2rr_0\cos\varphi)^{1.5}} r_0 dz' d\varphi dr_0 \\ u_r(r) &= \frac{2(1+\nu)(1-2\nu)}{\pi E} \iiint_{00Z_1}^{\infty\pi Z_2} \frac{p(r_0, t)(r - r_0\cos\varphi)}{\rho'^3(z'^2 + r^2 + r_0^2 - 2rr_0\cos\varphi)^{1.5}} r_0 dz' d\varphi dr_0 \end{aligned} \quad (5.4)$$

where: ν is the Poisson's ratio; E is the Young's modulus (GPa); $p(r_0, t)$ is the pressure change (Pa) at radial distance r_0 and time t , ϕ is the difference of azimuthal angle between surface point and the dilation center; z_1 is the depth of reservoir lower bound (m) and z_2 is the depth of reservoir upper bound (m).

Each of these solutions has been validated through numerical simulations (Xu et al., 2012; Mathias et al., 2009a) or comparison with in situ observation (Theis, 1935). However, the analytical model used in our paper has its limitations relating to the complexity of subsurface structure and deformation processes. But the simple analytical allows us to estimate large-scale pressure change and surface displacement by considering the realistic injection and production history for hundreds of operation wells. The calculation time is fast compared to more complex models, and as we shall show, provides an adequate fit to our data.

5.5.2 Input parameters of the analytical simulations

The depth and thickness of the reservoir are irregular (Han et al., 2010). In our model, we use an average thickness of 200 m, ranging from depth 2000 m to 2200 m, based on the depths of injection wells provided by Railroad Commission of Texas (RRC) and personal communication with the operator of the field. The average porosity (9.8%) and permeability (19 mD) reported by Raines (2005) were measured from a core-flooding test, which typically does not include reservoir scale imperfections such as fractures and other forms of secondary porosity. Obviously, the reservoir is very heterogeneous (Han et al., 2010) but our analytical solution only requires mean porosity and permeability values. To better represent its variation, we choose three levels of porosity and permeability (low, medium and high), and predict three corresponding sets of pressure change and surface displacement. We utilize the relationship between porosity and permeability for the Canyon formation (the third sequence) given by Lucia and Kerans (2004) to calculate permeability based on three-levels of porosity (Table 5.1). Rock formation (limestone) compressibility is obtained from Newman et al. (1973). These and other properties of the reservoir formation are summarized in Table 5.1. We further assume that the extracted hydrocarbon gas is purely methane, and that the salt concentration of injected water is 0.15 kg/l.

Fluid properties (CO_2 , water, methane and oil) at reservoir pressure (16 MPa) and temperature (41.5 °C) are summarized in Table 5.2. Properties of supercritical CO_2 and methane are obtained from the NIST fluid properties website

(<http://webbook.nist.gov/chemistry/fluid/>). Properties of salt water are derived based on the empirical correlations with pressure, temperature and salt concentration shown in Mathias et al. (2009b). Density and viscosity of the produced oil are obtained from Vest Jr (1970). Oil compressibility is obtained from Satter et al. (2008).

Two geomechanical parameters, Young's modulus and Poisson's ratio, are needed for surface displacement calculation. However, there are no publicly available data for these two geomechanical properties for the overlaying Walfcamp shale. Since surface displacement is less sensitive to Poisson's ratio, a common result in many Earth deformation problems (e.g., Bevis et al., 2005), we set the value of Poisson's ratio to 0.25, and then forward model to estimate the value of Young's modulus that best fits the surface displacement observed by InSAR. We selected a profile across the significant inflation area for comparison between model simulation and InSAR observation (Figure 5.1). Grid search ranges are 1 – 50 GPa with search increments of 1 GPa. Goodness of fit is assessed using the standard chi-square statistic.

5.5.3 Injection and production data during 2004 - 2011

Monthly injection and production rates during 2004 to 2011 at individual wells in the field were provided by the field operator. Information concerning locations and depths of individual wells is provided by the RRC. Both CO₂ and water were injected into the reservoir from 2004 to 2011 (Figure 5.2). In detail, 409 wells injected CO₂; 217 wells injected water and 603 wells extracted oil and HC gas. In this field, injected CO₂ is often mixed with water, and extracted oil and HC gas are often mixed with CO₂ and water. Location of active injection and production wells during 2004 - 2011 is shown in Figure 5.5.

To reduce the computation we divide the field into grids of 500 m width (Fig. 5.6). We then approximate the injection/production history by placing a virtual well at the center of each grid. For CO₂ and water, we calculate the mean injection/extraction rate by adding the net fluid injection and extraction for that grid respectively. For oil and HC gas, the production rate is set equal to the net fluid extracted for that grid.

To compare with InSAR observations, we should predict surface displacement from January 2007 to March 2011. However, pressure change due to constant rate injection/production is not linear with time: fluid pressure changes significantly in the first few months and then slows down (Rohmer and Raucoules, 2012). Thus, for a well being operated before 2007, pressure change during 2007 to 2011 cannot be simply calculated by just using data from January 2007 to March 2011. To address this problem, we check the injection/production history of every well to see if there is any operation before 2007. If there is, we calculate pressure changes during two periods for that well: one period from the beginning of operation to March 2011 and second period from the beginning of operation to December 2006. We then subtract the pressure change during the second phase from the pressure change during the first phase to derive pressure change between January 2007 and March 2011 (the period of InSAR observations). If there is no operation prior to 2007, pressure change is calculated using data from January 2007 to March 2011. It is worth noting that fluid production and injection in the field started in 1948 and 1954 respectively, and we only have injection/production data for each well from 2004. Thus, in our simulation, the operational beginning of each well is not earlier than 2004.

5.6 Simulation results

Figure 5.7 shows the simulated changes in reservoir pressure due to different fluid injection/extraction rates for three assumed values of rock formation porosity and permeability. The local maxima and minima patterns are similar for the different values of porosity and permeability. Calculated pressure change in the reservoir decreases for higher values of porosity and permeability. Net CO₂ injection/production significantly affects reservoir pressure. Since volumes of water injection and production are approximately the same (Figure 5.2, Figure 5.4b), pressure changes due to net water injection are negligible compared to those caused by net CO₂ injection, indicating that surface uplift observed by InSAR is dominated by CO₂ injection. Net water injection/production causes pressure buildup/drawdown in different areas of the field. Net oil and hydrocarbon gas production generally causes pressure drawdown in the field. In summary, pressure

changes due to CO₂ injection and production are much higher than that caused by water injection/production and oil/hydrocarbon gas production.

Figure 5.8 shows the simulated total pressure buildup due to all fluid injection and oil/hydrocarbon gas production production for three assumed values of porosity and permeability. The low value of porosity and permeability condition yields pressure buildup up to 10 MPa, while the high value yields up to 2 MPa pressure buildup. Maximum pressure buildup is more spread out for the high porosity and permeability values.

Based on the simulated pressure change field, a grid search method was used to estimate the value of Young's modulus that best fits the InSAR observations along the profile marked in Figure 5.1. To compare with InSAR LOS displacement, we convert the predicted surface displacement to LOS displacement using satellite azimuth and incidence information. Figure 5.9 shows goodness of fit versus Young's modulus at three levels of pressure change. The best-fit values for Young's moduli are listed in Table 5.3. Predicted LOS displacements using the best-fit Young's modulus at the three levels of pressure change are compared to the InSAR data along the profile (Figure 5.10). All three predictions agree well with InSAR observations along the profile. The high-pressure condition provides the smallest misfit between model prediction and observation, but the difference with the other models is small. The low and medium pressure conditions also provide a good fit between model prediction and observation. However, the best-fit Young's moduli derived from the low and medium pressure conditions (6 GPa and 10 GPa) are quite small compared to the best-fit Young's modulus derived from the high-pressure condition (18 GPa), and are on the low side of plausible crustal values. A similar deformation study in south Texas (Karegar et al., 2015) where pressure data were available for calibration gave a best estimate of average Young's modulus of 55 GPa +80/-20 GPa; at 95% confidence, the minimum estimate obtained in that study was 15 GPa, similar to our high estimate. We therefore take the estimate of 18 GPa as the most plausible value for Young's modulus and the corresponding estimate of the high-pressure buildup condition (up to 10 MPa) as the best pressure change estimate.

We then predict 2D LOS displacement fields for the three models of pressure change respectively using the best-fit Young's modulus derived from the profile fitting analysis. Simulated 2D LOS displacement at the high-pressure change condition and the residual between InSAR observation and model prediction are shown in Figure 5.11. Our simulation is able to match most of the uplift signal observed by InSAR. However, up to 4 cm of residual uplift remains. The residuals likely reflect a combination of atmospheric and reservoir heterogeneity. The former reflects deviations from the assumption used in our data analysis that atmospheric properties are laterally uniform. The latter reflects deviations from the assumption used in our modeling that the rheological properties of the reservoir are vertically and horizontally uniform.

5.7 Discussion

We modeled a reservoir as a simplified body with uniform properties. In fact, it almost certainly has significant spatial variation in porosity, permeability and elastic properties. We have also ignored inter-well pressure interaction when simulating reservoir pressure change. Despite these simplifications, we are able to obtain good fits to the surface deformation data and obtain useful information on the reservoir. This reflects the fact that the free surface is 2000 m above the reservoir, hence the effects of reservoir heterogeneity and inter-well pressure interactions on surface deformation are relatively small. In effect, the intervening crustal material acts like a low pass filter, attenuating short wavelength strain effects associated with spatial complexities of the reservoir and the injected fluid.

The relatively large uncertainty in our estimate of Young's modulus reflects the weak resolving power of surface deformation data for this parameter. Independent determination of Young's modulus from down-hole measurements, 3-D seismic surveys, or laboratory experiments on well bore samples would allow a more quantitative link between surface deformation and reservoir pressure change.

Gan and Frohlich (2013) suggested that increasing earthquakes in the Cogdell field, north of our study area, during 2006 – 2011 were likely triggered by CO₂ injection. However, our study area, which has also experienced significant fluid injection over the

same time period, has not experienced a significant increase in seismicity. Meanwhile, InSAR data show no surface uplift in the Cogdell field, while measurable uplift is observed in our study area. The different seismic and deformation responses to fluid injection between these two fields may reflect differences in regional subsurface structures. Our study area has been mapped as a single large reef mound, but structures in the Cogdell field show more spatial variation (Vest Jr, 1970). The Cogdell limestone may have experienced more intense weathering and karsting compared to our study area (Reid and Reid, 1991), potentially creating more heterogeneous structures, and potential faults and fractures. The recent earthquakes suggest the presence of faults in the Cogdell field. The absence of mapped faults and earthquake activity in our study area suggests no active faulting. Perhaps triggered earthquakes occur when injected gas or fluid reaches suitably orientated pre-existing faults, reducing the resolved normal stress and hence the effective friction, and promoting seismic slip on pre-existing faults.

5.8 Conclusions

We evaluated injection and production data for CO₂, water, oil and hydrocarbon gas at individual wells in a CO₂-EOR field between 2004 and 2011. Approximately 50 Mt of CO₂ were sequestered between 2004 and 2011, equal to the total sequestered CO₂ between 1972 and 2003. InSAR data observe up to 10 cm line of sight displacement between January 2007 and March 2011 in this field. Water injection alone cannot explain surface uplift between January 2007 and March 2011 because net injected water (\sim 1 Mt) is negligible during this period. However, significant amounts of CO₂ (\sim 24 Mt) were injected into the reservoir, contributing to observed surface uplift. An analytical simulation relating reservoir pressure and surface displacement using realistic injection and production data from individual wells predicts up to 10 MPa pressure buildup due to net fluid injection and production in 2007- 2011, using assumed average values of porosity and permeability. With better information on the mechanical properties of the reservoir, InSAR data could directly estimate reservoir pressure changes with time.

5.9 Acknowledgements

We thank the field operator for providing historical injection and production data. We also thank the Railroad Commission of Texas for providing information on the location and depth of individual wells in our study area. This research was supported by DOE grant DE-FE0001580. We thank Karen Kluger for support and advice throughout our project and two anonymous reviewers for thoughtful comments.

5.10 References

- Berardino, P., Fornaro, G., Lanari, R., and Sansosti, E. (2002). A new algorithm for surface deformation monitoring based on small baseline differential sar interferograms. *Geoscience and Remote Sensing, IEEE Transactions on*, 40(11):2375–2383.
- Bevis, M., Alsdorf, D., Kendrick, E., Fortes, L. P., Forsberg, B., Smalley, R., and Becker, J. (2005). Seasonal fluctuations in the mass of the amazon river system and earth’s elastic response. *Geophysical research letters*, 32(16).
- Brummett Jr, W., Emanuel, A., Ronquille, J., et al. (1976). Reservoir description by simulation at sacroc-a case history. *Journal of Petroleum Technology*, 28(10):1–241.
- Bryant, S. et al. (2007). Geologic co2 storage—can the oil and gas industry help save the planet? *Journal of Petroleum Technology*, 59(09):98–105.
- Crameik, T., Plassey, J., et al. (1972). Carbon dioxide injection project sacroc unit, scurry county, texas. In *Annual Meeting Papers, Division of Production*. American Petroleum Institute.
- Dicharry, R. M., Perryman, T., Ronquille, J., et al. (1973). Evaluation and design of a co2 miscible flood project-sacroc unit, kelly-snyder field. *Journal of Petroleum Technology*, 25(11):1–309.
- Galloway, W. E., Ewing, T., Garrett, C., Tyler, N., and Bebout, D. (1983). Atlas of major texas oil reservoirs.

Gan, W. and Frohlich, C. (2013). Gas injection may have triggered earthquakes in the cogdell oil field, texas. *Proceedings of the National Academy of Sciences*, 110(47):18786–18791.

Han, W. S., McPherson, B. J., Lichtner, P. C., and Wang, F. P. (2010). Evaluation of trapping mechanisms in geologic co₂ sequestration: Case study of sacroc northern platform, a 35-year co₂ injection site. *American Journal of Science*, 310(4):282–324.

Karegar, M. A., Dixon, T. H., Malservisi, R., Yang, Q., Hossaini, S. A., and Hovorka, S. D. (2015). Gps-based monitoring of surface deformation associated with co₂ injection at an enhanced oil recovery site. *International Journal of Greenhouse Gas Control*, 41:116–126.

Lucia, F. J. and Kerans, C. (2004). Permeability estimation using porosity logs and rock fabric stratigraphy: an example from the sacroc (pennsylvanian) field, scurry county, texas. *PUBLICATIONS-WEST TEXAS GEOLOGICAL SOCIETY*, 4:271.

Mathias, S. A., Hardisty, P. E., Trudell, M. R., and Zimmerman, R. W. (2009a). Approximate solutions for pressure buildup during co₂ injection in brine aquifers. *Transport in Porous Media*, 79(2):265–284.

Mathias, S. A., Hardisty, P. E., Trudell, M. R., and Zimmerman, R. W. (2009b). Screening and selection of sites for co₂ sequestration based on pressure buildup. *International Journal of Greenhouse gas control*, 3(5):577–585.

Metz, B., Davidson, O., de Coninck, H., Loos, M., Meyer, L., et al. (2005). Carbon dioxide capture and storage.

Morris, J. P., Hao, Y., Foxall, W., and McNab, W. (2011). A study of injection-induced mechanical deformation at the in salah co₂ storage project. *International Journal of Greenhouse Gas Control*, 5(2):270–280.

Newman, G. et al. (1973). Pore-volume compressibility of consolidated, friable, and unconsolidated reservoir rocks under hydrostatic loading. *Journal of Petroleum Technology*, 25(02):129–134.

Orr, F. and Taber, J. (1984). Use of carbon dioxide in enhanced oil recovery. *Science*, 224(4649):563–569.

Pepe, A. and Lanari, R. (2006). On the extension of the minimum cost flow algorithm for phase unwrapping of multitemporal differential sar interferograms. *Geoscience and Remote Sensing, IEEE Transactions on*, 44(9):2374–2383.

Raines, M. (2005). 66. kelly-snyder (cisco-canyon) fields/sacroc unit. *Oil and gas fields in west Texas*, pages 69–78.

Raines, M. and Dobitz, J. (2001). A review of the pennsylvanian sacroc unit. *PUBLICATIONS-WEST TEXAS GEOLOGICAL SOCIETY*, pages 67–74.

Reid, A. and Reid, S. T. (1991). The cogdell field study, kent and scurry counties, texas: A post-mortem. *Permian Basin Plays, Tomorrow's Technology Today: Midland, Texas, West Texas Geological Society, Publication*, pages 91–89.

Reuter, H. I., Nelson, A., and Jarvis, A. (2007). An evaluation of void-filling interpolation methods for srtm data. *International Journal of Geographical Information Science*, 21(9):983–1008.

Rinaldi, A. P. and Rutqvist, J. (2013). Modeling of deep fracture zone opening and transient ground surface uplift at kb-502 co 2 injection well, in salah, algeria. *International Journal of Greenhouse Gas Control*, 12:155–167.

Rohmer, J. and Raucoules, D. (2012). On the applicability of persistent scatterers interferometry (psi) analysis for long term co 2 storage monitoring. *Engineering Geology*, 147:137–148.

Satter, A., Iqbal, G. M., and Buchwalter, J. L. (2008). *Practical enhanced reservoir engineering: assisted with simulation software*. Pennwell Books.

Shi, J.-Q., Sinayuc, C., Durucan, S., and Korre, A. (2012). Assessment of carbon dioxide plume behaviour within the storage reservoir and the lower caprock around the kb-502 injection well at in salah. *International Journal of Greenhouse Gas Control*, 7:115–126.

Theis, C. V. (1935). *The relation between the lowering of the piezometric surface and the rate and duration of discharge of a well using ground water storage*. US Department of the Interior, Geological Survey, Water Resources Division, Ground Water Branch Washington, DC.

Vasco, D., Ferretti, A., and Novali, F. (2008). Reservoir monitoring and characterization using satellite geodetic data: Interferometric synthetic aperture radar observations from the krechba field, algeria. *Geophysics*, 73(6):WA113–WA122.

Vasco, D., Rucci, A., Ferretti, A., Novali, F., Bissell, R., Ringrose, P., Mathieson, A., and Wright, I. (2010). Satellite-based measurements of surface deformation reveal fluid flow associated with the geological storage of carbon dioxide. *Geophysical Research Letters*, 37(3).

Verdon, J. P., Kendall, J.-M., Stork, A. L., Chadwick, R. A., White, D. J., and Bissell, R. C. (2013). Comparison of geomechanical deformation induced by megatonne-scale co₂ storage at sleipner, weyburn, and in salah. *Proceedings of the National Academy of Sciences*, 110(30):E2762–E2771.

Vest Jr, E. (1970). Oil fields of pennsylvanian-permian horseshoe atoll, west texas.

White, J. A., Chiaramonte, L., Ezzedine, S., Foxall, W., Hao, Y., Ramirez, A., and McNab, W. (2014). Geomechanical behavior of the reservoir and caprock system at the in salah co₂ storage project. *Proceedings of the National Academy of Sciences*, 111(24):8747–8752.

Xu, Z., Fang, Y., Scheibe, T. D., and Bonneville, A. (2012). A fluid pressure and deformation analysis for geological sequestration of carbon dioxide. *Computers & Geosciences*, 46:31–37.

Table 5.1: Reservoir homogeneous properties used for pressure change calculation.

Reservoir Property	Symbol	Value			Unit
Porosity	φ	0.2(L)	0.25(M)	0.3(H)	%
Permeability	κ	17(L)	57(M)	152(M)	mD
Initial pressure	P_0	16			MPa
Temperature	T	41.5			°C
Depth (reservoir upper bound)	Z_1	-2000			m
Depth (reservoir lower bound)	Z_2	-2200			m
Thickness	H	200			m
Formation compressibility	C_{rock}	5.3E-10			1/Pa

Note: L , M and H represent low level, medium level and high level of porosity and permeability, respectively.

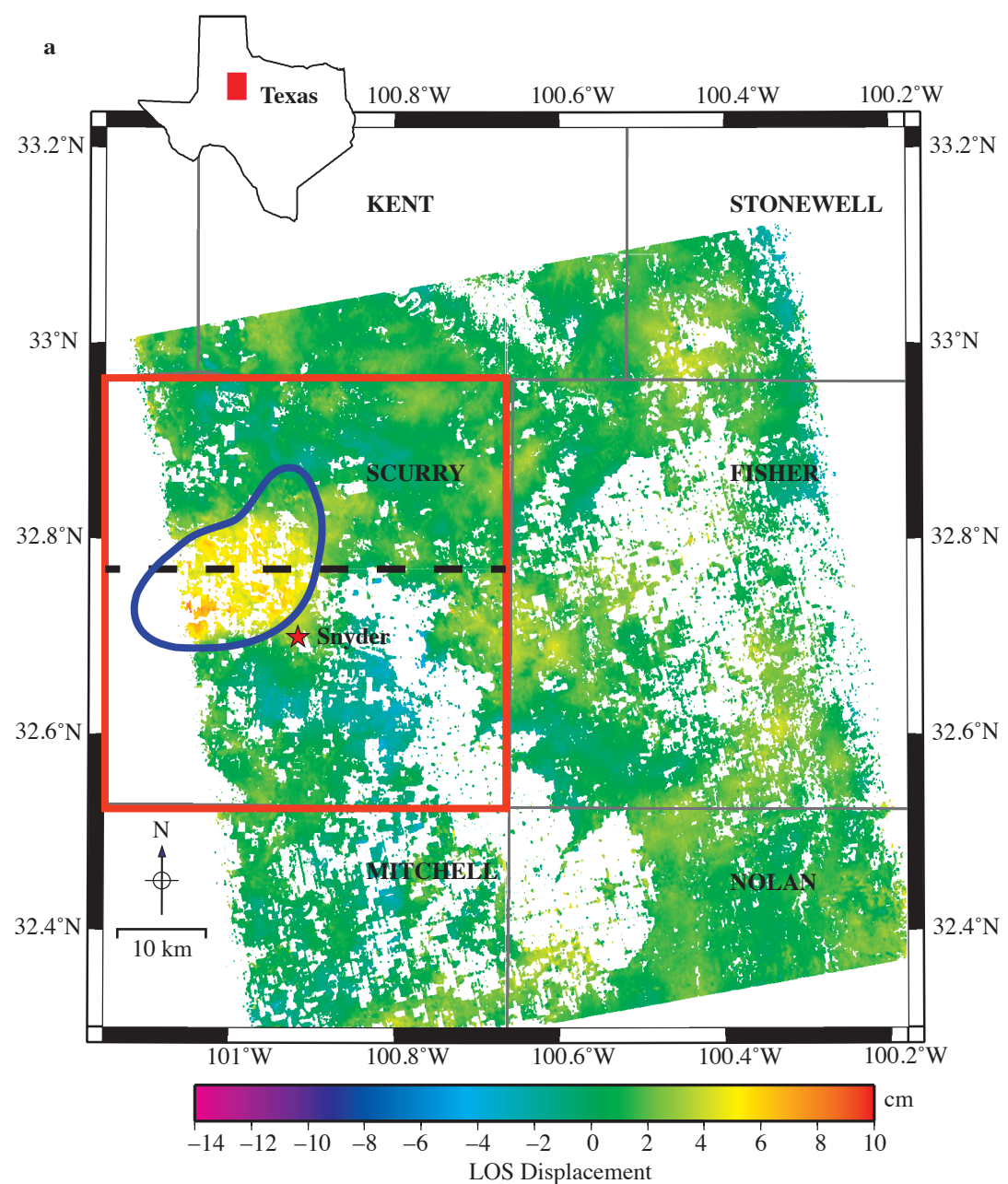
Table 5.2: Fluid properties at depth (16MPa,41.5 °C).

Fluid property	Symbol	Value				Unit
		Brine	CO2	Methane	Oil	
Density	ρ	1105	784	115	818	kg/m ³
Viscosity	μ	9.41E-04	6.85E-05	1.67E-05	3.75E-04	Pa·s
Compressibility	C	3.40E-10	2.10E-08	5.43E-08	2.17E-09	1/Pa

Table 5.3: Highest pressure buildup and best-fit Young's modulus at three levels of porosity and permeability.

Level of porosity and permeability	Highest ΔP (MPa)	Best-fit E (GPa)	χ^2
Low	10.32	18	0.78
Medium	4.32	10	0.80
High	2.10	6	0.83

Note: E represents Young's modulus. ΔP represents calculated pressure change. χ^2 represents normalized chi square value.



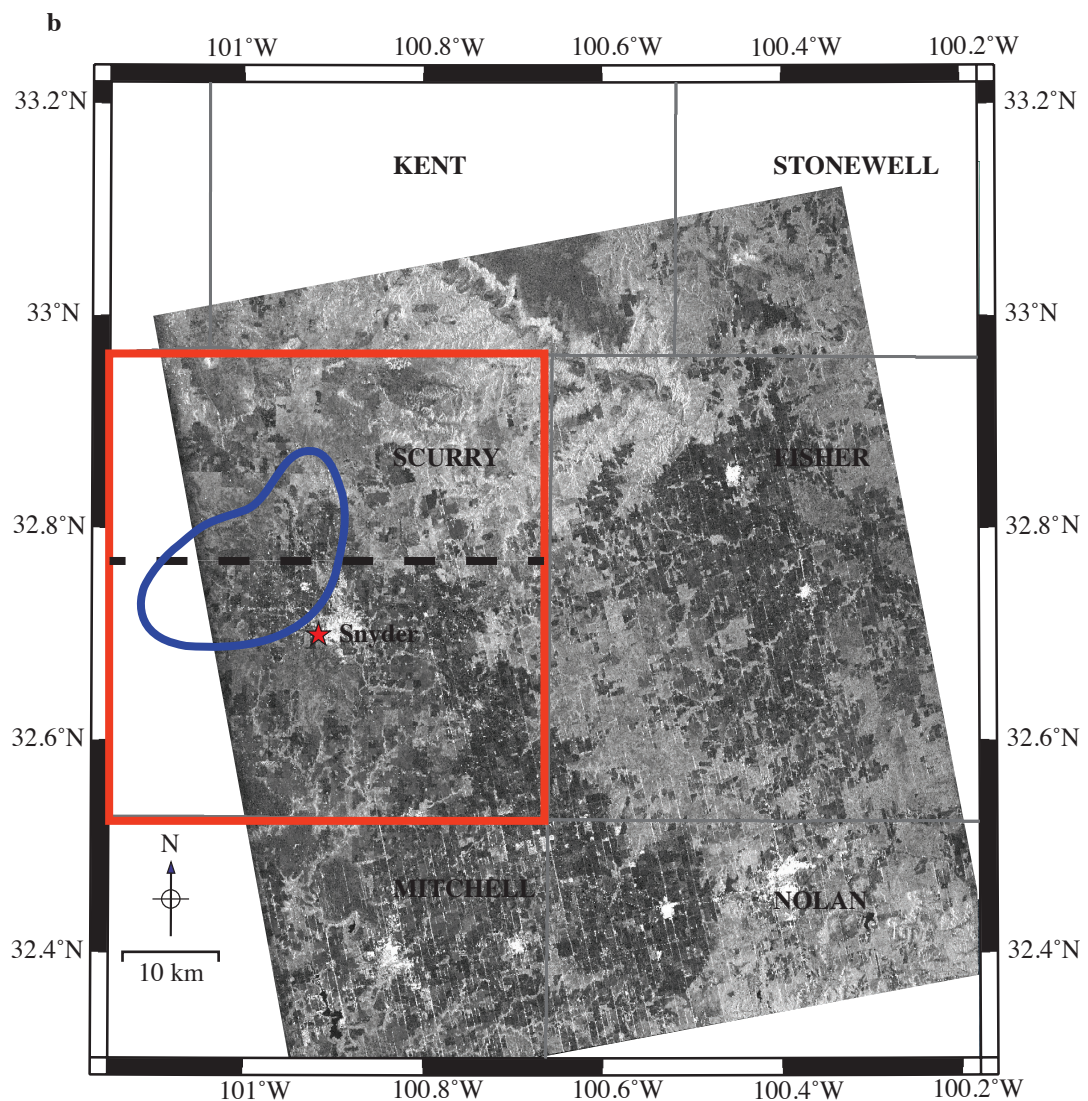


Figure 5.1: (a) Total LOS (line of sight) displacement from January. 08, 2007 to March. 06, 2011. (b) A SAR intensity image of the study area. Red star represents location of the town of Snyder, Texas. Light grey lines are county boundaries and county names are labeled. Red lines are the boundaries of our study area, Scurry County. Blue line is the approximate boundary of the oil field in the study area. Black dashed line represents location of a profile for surface displacement modeling in the following sections.

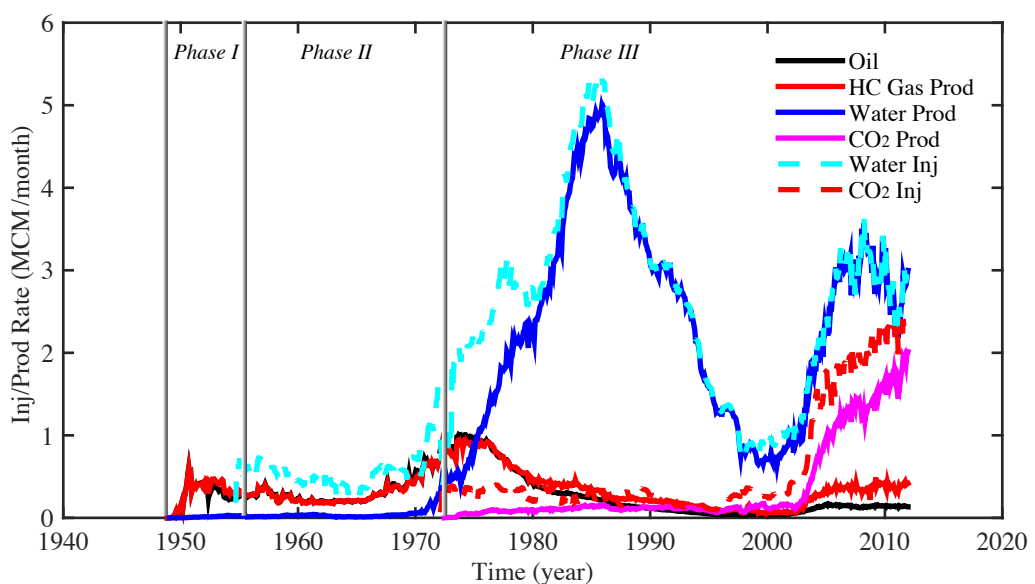


Figure 5.2: Injection and production history of the study site. Phase I is the primary recovery phase. Phase II is the secondary recovery phase. Phase III is the tertiary/enhanced oil recovery phases. Volumes of fluid injection and production are reported at 16 MPa, 41.5 °C (pressure and temperature at reservoir depth). HC is hydrocarbon.

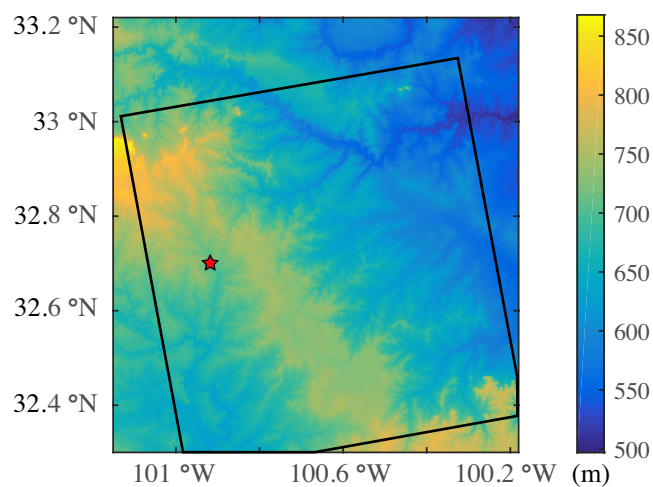


Figure 5.3: DEM of our study area. Black lines are the boundaries of the area covered by the interferogram. Red star represents location of the town Snyder, Texas.

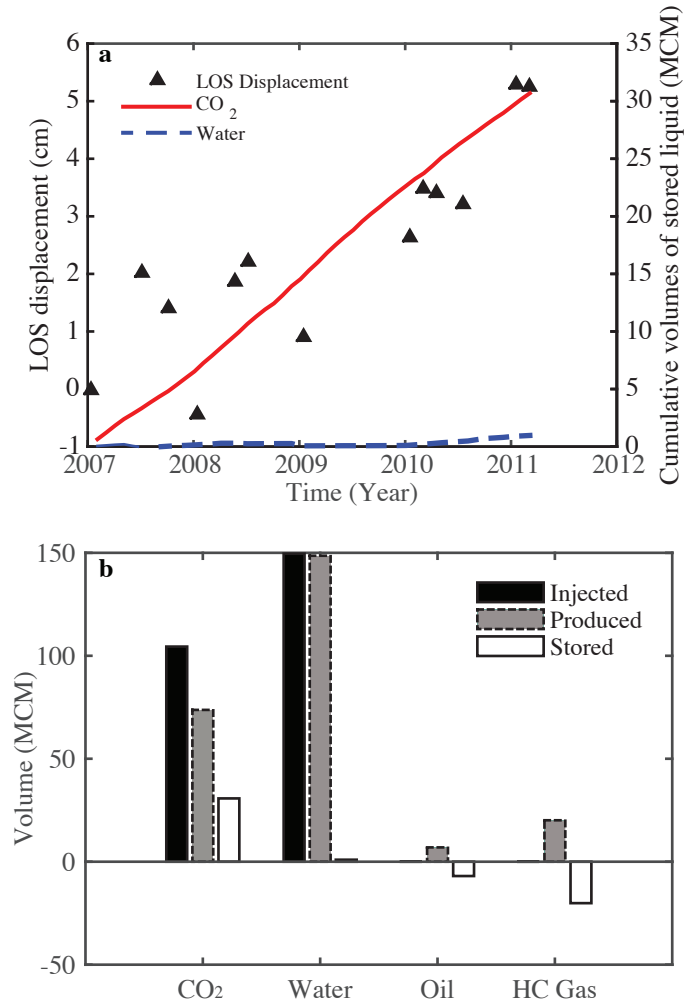


Figure 5.4: (a) Comparison between Line of Sight (LOS) displacement at Snyder (red star marked in Figure 5.1) and cumulative volumes of stored (injection minus production) CO_2 and water in the field from January 2007 to March 2011. (b) The total volumes of injected/produced/stored CO_2 , water, oil and HC gas in the field from January 2007 – March 2011. Volumes of fluid injection and production are reported at 16 MPa, 41.5 °C.

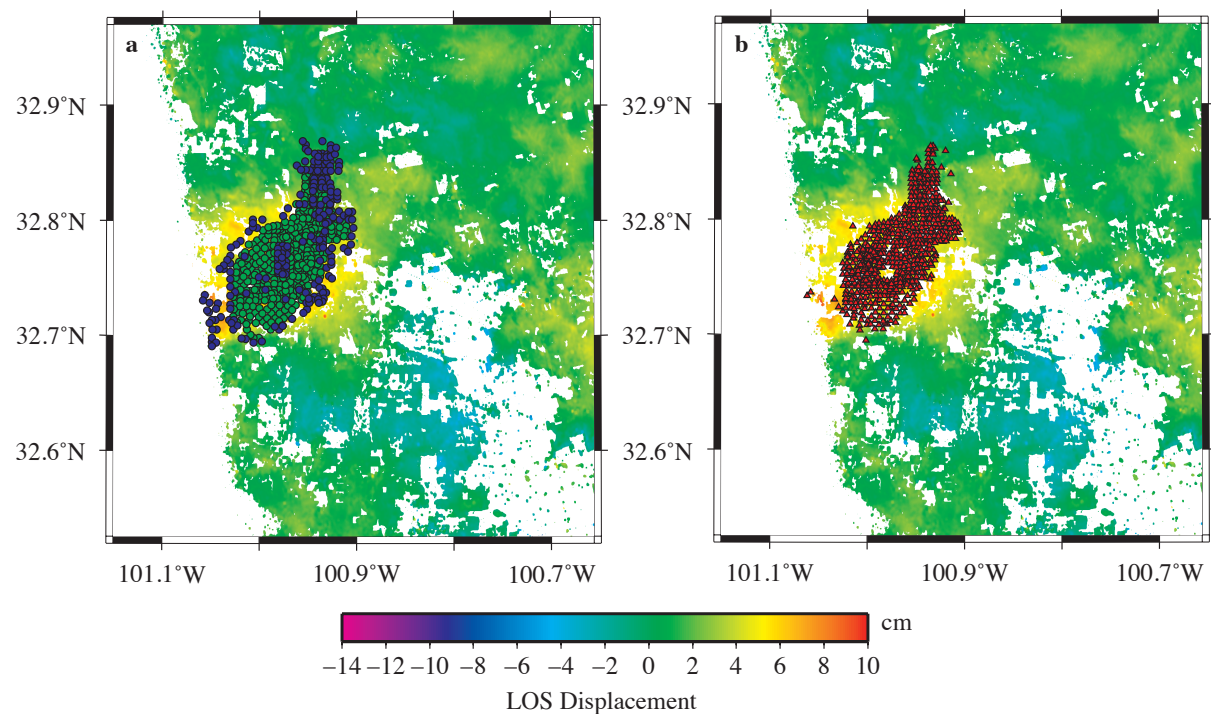


Figure 5.5: Map of study area, showing total LOS displacement from January 08, 2007 to March. 06, 2011, (a) wells injecting CO₂ (green circle) and water (blue circle), and (b) well producing CO₂, water, Oil and HC gas (red triangle).

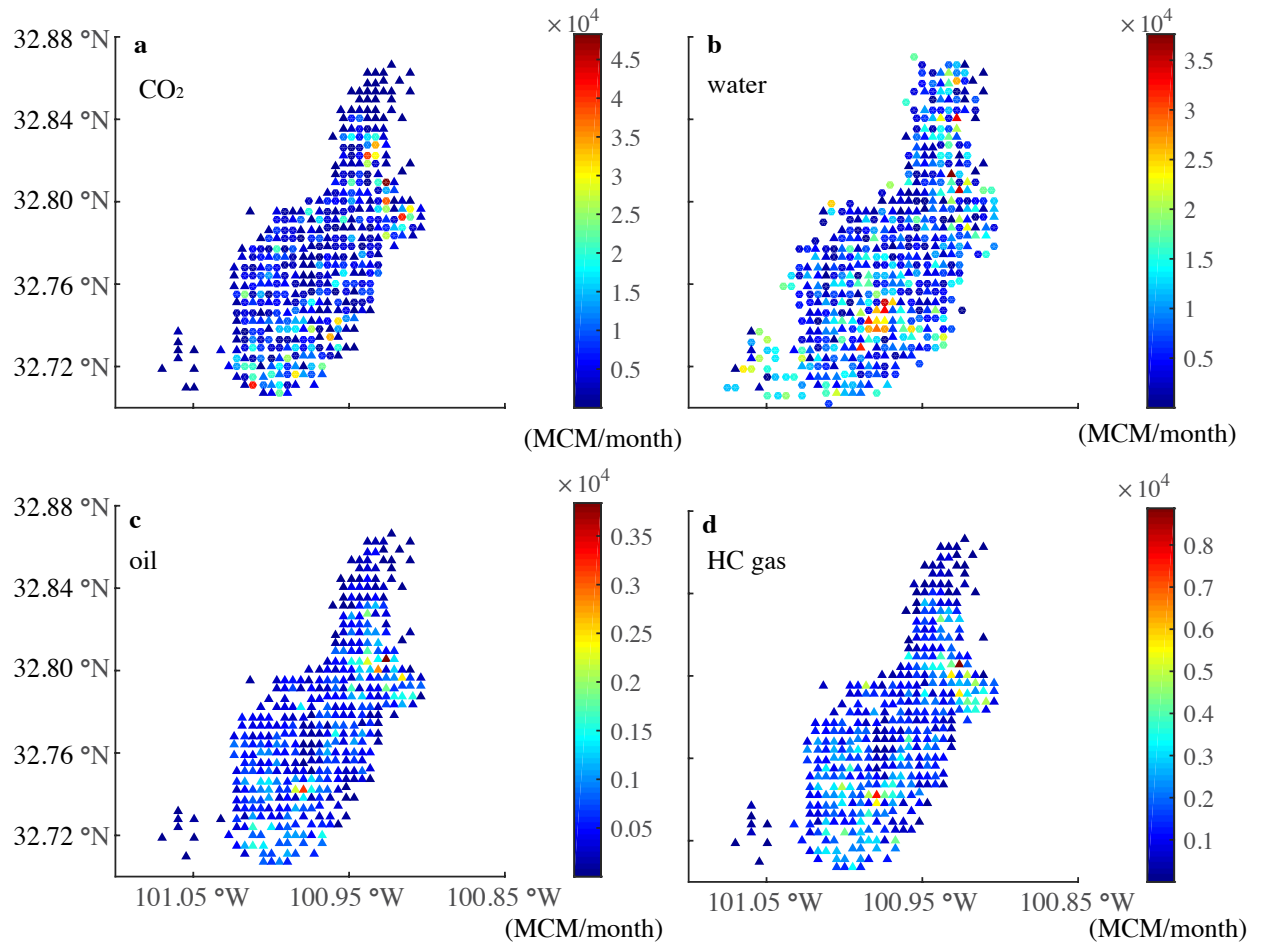


Figure 5.6: Location of virtual wells for each type fluid and the average monthly injection/production rate for each virtual well. Circles represent injection wells and triangles represent production wells. Volumes of fluid injection and production are reported at 16 MPa, 41.5 °C.

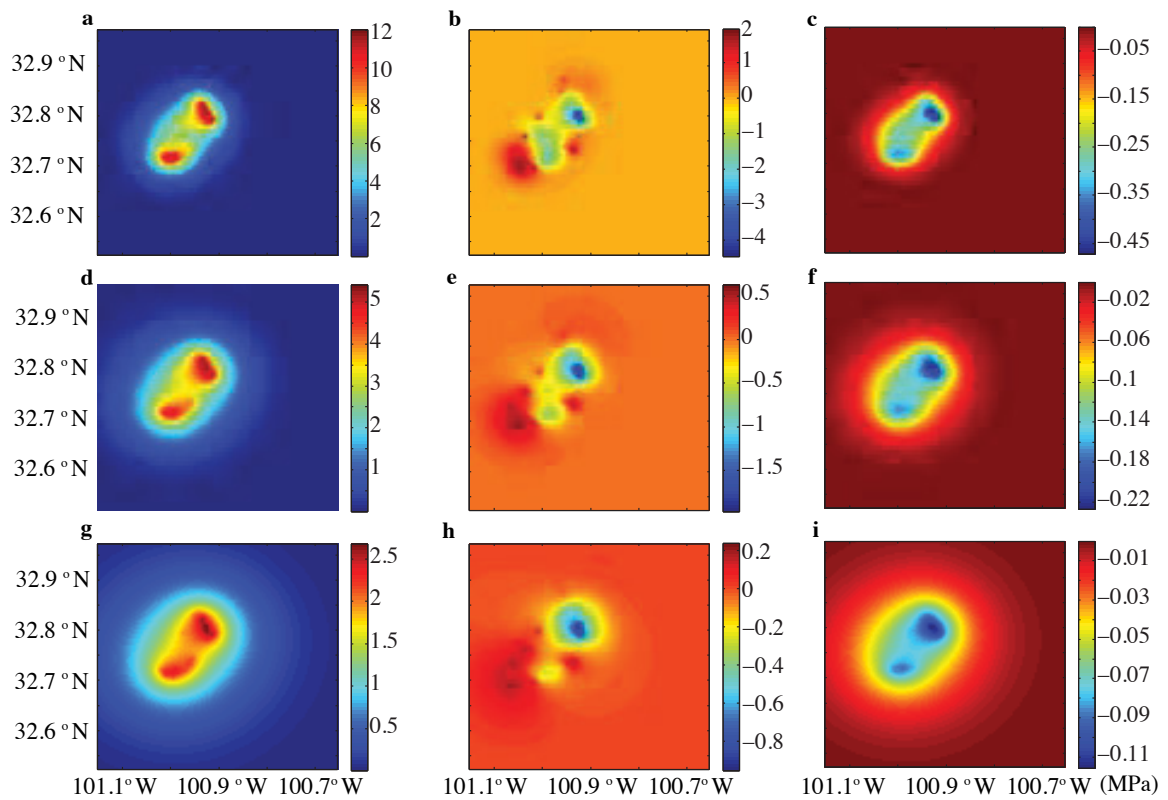


Figure 5.7: Calculated pressure change due to fluid injection and production at three levels of porosity and permeability. (a-c: low porosity/permeability; d-f: medium porosity/permeability; g-i: high porosity and permeability). a,d and g are calculated pressure buildup due to net CO_2 injection. b, e and h are derived from net water injection. c, f and I are derived from oil and HC gas production

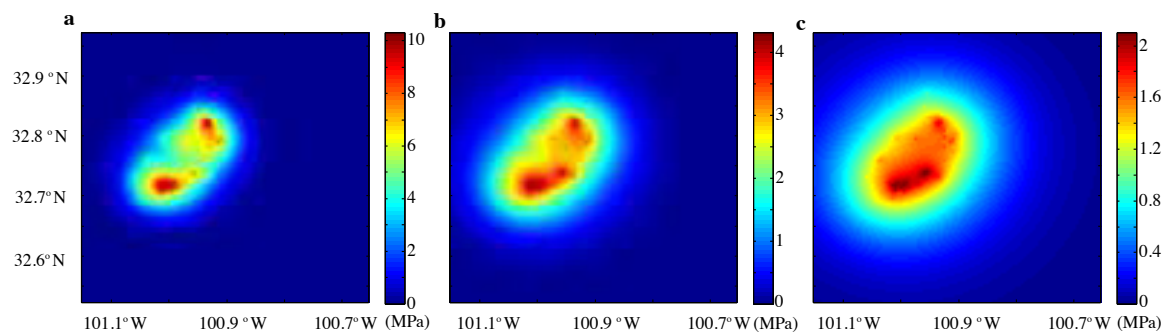


Figure 5.8: Calculated pressure change due to all injection and production activities at three levels of porosity and permeability. (a) low porosity/permeability level; (b) medium porosity/permeability level; (c) high porosity and permeability level.

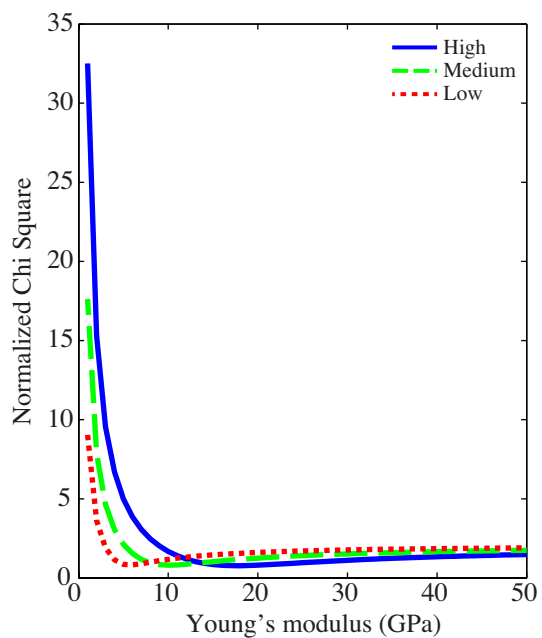


Figure 5.9: Goodness of fit versus Young's modulus at three levels of pressure change conditions. Simulated LOS displacements are fitted to LOS displacement observation along the profile shown in Figure 5.1. Note that the minimum value of Young's modulus is well constrained, but the upper bound value is not.

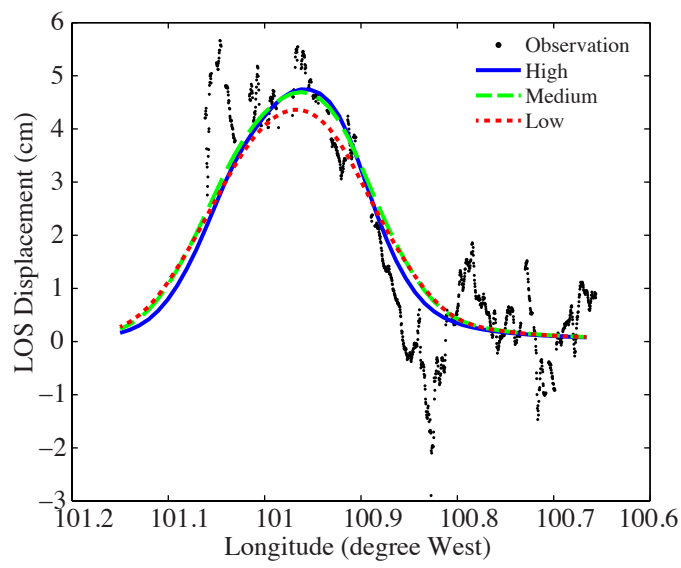


Figure 5.10: Simulated LOS displacement at three levels of pressure change conditions versus InSAR observation along the profile shown in Figure 5.1.

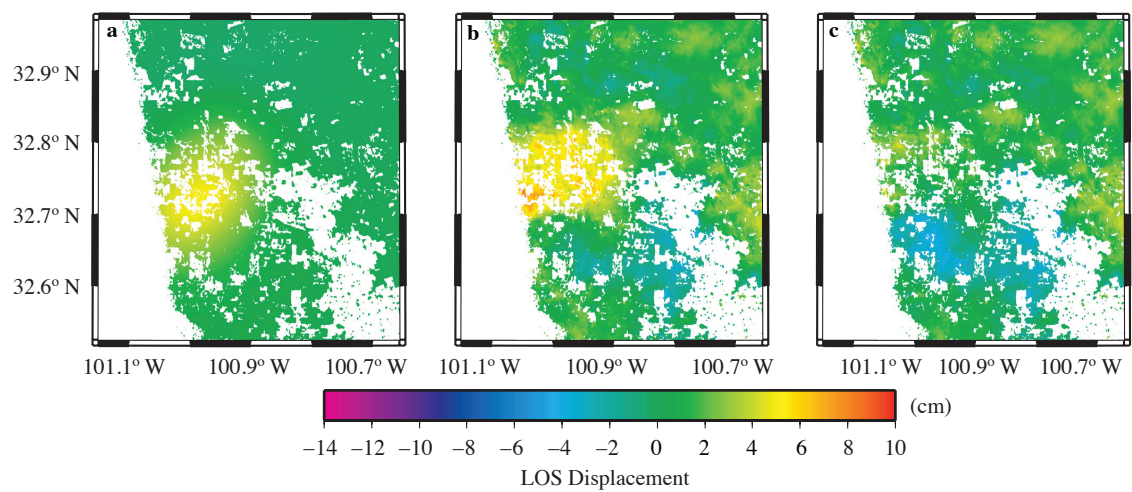


Figure 5.11: Comparison between simulated LOS displacements and InSAR observation for the entire study area. Surface displacements were derived from high-pressure change condition. (a) Simulated LOS displacements; (b) InSAR observation; (c) residual.

6. Conclusions and Future Work

6.1 Conclusions

This dissertation presents three studies that use satellite geodesy to study environmental and global change. The main conclusions from these studies are described in Chapters Three, Four and Five and are summarized here.

Chapter Three shows that short-term annual variations in coastal uplift in Greenland as measured by GPS are useful to study spatial and temporal changes in mass loss of the ice sheet. Anomalously large uplift is observed at most GPS sites in 2010, indicating significant ice mass loss in 2010. Comparison between GPS data and climatic data suggests that the anomalous melting in 2010 is caused by a combination of warm air and warm sub-surface ocean water. The Irminger Current, a warm subsurface current that constitutes part of the sub-polar gyre, plays an important role in "shaping" the spatial pattern of coastal melting; the amount of ice mass loss decreases along the pathway of the Irminger Current (from southeastern and southern and then southwestern Greenland). The maximum northern extent of its influence in 2010 was about 69 °N.

Chapter Four shows that accelerated melting of the Greenland ice sheet can in turn influence the regional ocean. Recent freshwater flux from Greenland is estimated using GRACE gravity data. Freshwater flux from Greenland, the Canadian Arctic Archipelago and the Arctic sea ice increase by 20 mSv from the mid-late 1990s to 2013. I estimate that at least 70 percent of the increase winds up in the Labrador Sea due to the clockwise nature of ocean circulation around Greenland. This study shows that a rapid decline in Labrador Sea Water thickness and density coincided with a rapid increase in freshwater flux into the Labrador Sea while the salt flux into the region remained high. This suggests that recent accelerated melting of the Greenland ice sheet has started to reduce

the formation of Labrador Sea Water and potentially weaken the Atlantic Meridional Overturning Circulation.

Chapter Five shows that InSAR monitoring of surface deformation is a promising approach to estimate pressure changes in deep reservoirs subject to fluid injection. Up to 10 cm surface uplift was observed between January 2007 and March 2011 at a CO₂-EOR field in Scurry County, West Texas. Monthly injection and production data and an analytical model are utilized to estimate the pressure change in the reservoir and to investigate causes of the observed uplift. Net CO₂ injection results in up to 12 MPa pressure build up in the reservoir, and was major contributor to the observed surface uplift.

6.2 Future Work

In Chapter Three, the GPS data are collected and processed up till 2011. This study shows extreme ice mass loss in 2010, while later studies show that ice mass loss in 2012 and 2015 was also high (e.g., Hanna et al., 2014; Tedesco et al., 2015). Continuous monitoring of annual variations in coastal uplift allows estimates of ice mass loss in coastal Greenland that are independent of GRACE. Longer observations would allow for better correlation analysis between annual uplift and climatic factors. Until now, only short-term elastic crustal response to current mass loss and long-term viscous crustal and upper mantle response to past ice mass loss have been considered as the controlling factor to vertical surface motion here. Since recent accelerated mass loss of the Greenland ice sheet started three decades ago, the viscous response to this recent mass change should be considered (e.g., Nick et al., 2009; Nield et al., 2014). KULU is a long-term GPS station located near Helheim Glacier in southeast Greenland. The GPS time series here shows non-linear uplift since 2003. The rapid speed up and a subsequent slowdown behavior are well known from various types of data for Helheim Glacier (e.g., Howat et al., 2005; Nick et al., 2009), which is probably a big source of the KULU uplift. Thus, it is probably an over-simplification to fit a constant acceleration model to the KULU GPS time series. A combination of various ice mass change record and a viscoelastic crustal/upper mantle response could better explain the non-linear uplift pattern at KULU.

In Chapter Four, the freshwater flux estimate is a minimum estimate. I focused on three freshwater sources that likely influence Labrador Sea convection and can be estimated by remote techniques: the Greenland Ice Sheet, glaciers in the Canadian Arctic Archipelago, and changes in Arctic sea ice. Other sources such as precipitation minus evaporation, oceanic transport and melt water from the annual freeze-thaw cycle of Arctic Sea ice also contribute to the Arctic freshwater budget. Thus, besides remote techniques, in situ measurements are required to better measure the Arctic freshwater budget. Chemical tracers can help to investigate the pathways of freshwater and distinguish freshwater of different origins (Haine et al., 2015). This study suggests that at least 70% of Arctic freshwater flux ends up in the Labrador Sea, reducing the formation of Labrador Sea Water, hence weakening the AMOC. This hypothesis can be validated by sophisticated numerical experiments that allow freshwater flux to be focused into the Labrador Sea and determining its effect on the AMOC.

In Chapter Five, I show that InSAR-monitored surface deformation can be an indicator of reservoir pressure change. However, better knowledge of rheological parameters such as Young's modulus is required to more quantitatively link surface deformation and reservoir pressure. Thus, independent determination of Young's modulus from down-hole measurements or other methods is suggested for future work.

6.3 References

- Haine, T. W. N., Curry, B., Gerdes, R., Hansen, E., Karcher, M., Lee, C., Rudels, B., Spreen, G., de Steur, L., Stewart, K. D., and Woodgate, R. (2015). Arctic freshwater export: status, mechanisms, and prospects. *Global and Planetary Change*, 125:13–35.
- Hanna, E., Fettweis, X., Mernild, S. H., Cappelen, J., Ribergaard, M. H., Shuman, C. A., Steffen, K., Wood, L., and Mote, T. L. (2014). Atmospheric and oceanic climate forcing of the exceptional greenland ice sheet surface melt in summer 2012. *International Journal of Climatology*, 34(4):1022–1037.
- Howat, I. M., Joughin, I., Tulaczyk, S., and Gogineni, S. (2005). Rapid retreat and acceleration of helheim glacier, east greenland. *Geophysical Research Letters*, 32(22).

Nick, F. M., Vieli, A., Howat, I. M., and Joughin, I. (2009). Large-scale changes in greenland outlet glacier dynamics triggered at the terminus. *Nature Geoscience*, 2(2):110–114.

Nield, G. A., Barletta, V. R., Bordoni, A., King, M. A., Whitehouse, P. L., Clarke, P. J., Domack, E., Scambos, T. A., and Berthier, E. (2014). Rapid bedrock uplift in the antarctic peninsula explained by viscoelastic response to recent ice unloading. *Earth and Planetary Science Letters*, 397:32–41.

Tedesco, M., Box, J., Cappelen, J., Fausto, R., Fettweis, X., Hansen, K., Mote, T., Smeets, C., As, D., van de Wal, R., and Wahr, J. (2015). Greenland ice sheet [in arctic report card 2015].

Appendices

Appendix A: Supplementary information for Chapter 3

Atmospheric loading correction

Variable atmospheric pressure can cause cm-scale crustal deformation (Magie, 1969; Darwin, 1882; Petrov and Boy, 2004) and has been detected in GPS time series (Vandam et al., 1994; Dong et al., 2002). Atmospheric contributions therefore need to be removed from the GPS time series in order to isolate the ice load effects. To correct for air pressure loading, we use pre-computed Atmospheric Loading Displacements (ALD) provided by the Atmospheric Pressure Loading Service (<http://gemini.gsfc.nasa.gov/aplo/>). This provides a global 3-D ALD model on a 2.5×2.5 degree grid for routine reduction of geodetic data. The procedure for computing ALD is described by Petrov and Boy (2004). Briefly, ALD is calculated by convolving Farrell's elastic Green's functions (Farrell, 1972) with modeled global pressure data (2.5×2.5 degree grid), obtained by subtracting the mean surface pressure field over a baseline period (1980 to 2002) from the NCEP Reanalysis pressure field (Kalnay et al., 1996). ALD can thus be considered a deviation from an average position. Accuracy of the ALD model is validated by comparing with VLBI observations, and the uncertainty of this model is considered to be better than 15%. However, there is no VLBI in Greenland so the model uncertainty in Greenland could be larger.

Figure A1 shows an example of GPS vertical displacement time series before and after ALD correction and time series of ALD. After the ALD correction, GPS vertical displacement (D_{cal}) caused by ice mass change is:

$$D_{\text{cal}} = D_{\text{nal}} - D_{\text{alc}} \quad (\text{A1})$$

where D is the displacement, subscript cal and nal represent values with corrected atmospheric loading and with non-corrected atmospheric loading, and D_{alc} is the atmospheric loading correction, the displacement caused by changes of surface air mass load. In the summer months (May to August) when air pressure decreases, D_{alc} may be as high as 13 mm (light blue in Figure 2). In winter months (November to January) when air pressure

increases, D_{alc} is more negative (light yellow zone in Figure 2). Similar seasonal variations are observed in most time series used in this study.

Figure A2 shows a time series before and after atmospheric pressure loading correction and the respective best fit cubic spline models. The five parameters describing seasonal uplift derived from those models show slight differences (Table A1). Analysis of all time series shows that uplift values estimated from data corrected for atmospheric loading are higher compared to values estimated without correction.

Annual uplift (U) is the difference between annual highest displacement (D_h) and lowest displacement (D_l) estimated by the spline model:

$$U = D_h - D_l \quad (\text{A2})$$

The difference ΔU between annual uplifts estimated with and without atmospheric loading correction can be expressed as:

$$\Delta U = U_{\text{cal}} - U_{\text{nal}} = (D_{h_cal} - D_{l_cal}) - (D_{h_nal} - D_{l_nal}) \quad (\text{A3})$$

Substituting equation A1 into equation A3 yields:

$$\Delta U = [(D_{h_nal} - D_{h_alc}) - (D_{l_nal} - D_{l_alc})] - (D_{h_nal} - D_{l_nal}) = -D_{h_alc} + D_{l_alc} \quad (\text{A4})$$

Uplift start time is usually between May and July when D_{l_alc} is positive and uplift end time is usually between November to January when D_{h_alc} is negative (Figure A1), thus the value of ΔU is positive.

Except for Figure A2, all the data used in this paper are corrected for atmospheric loading as described above.

Local snow load effect

All GPS stations discussed in this report are installed on the rocky coastal margin of Greenland. These stations are sensitive not only to net surface mass balance and dynamic mass changes of the nearby ice sheet and glaciers, but also to local snow load

changes. We assessed the impact of these local snow loading effects using the snow depth dataset provided by DMI. These data show that in general stations in southern Greenland tend to have high winter snow loads. We selected meteorological station WMO-ID 04272 (Table A2) in the southern Greenland coastal area as typical (Carstensen and Jørgensen, 2011). Figure A3 shows the recorded snow depth from 1961 to 2003. The deepest snow depth recorded during that time is 100 cm in 1990. Assuming that 1 cm snow is equal to 1mm water (typical values for fresh snow) gives 100 mm water load. A simple elastic model for load-related subsidence at the surface of an infinite elastic medium is:

$$dl = \sigma \cdot l_0 / E \quad (\text{A5})$$

where σ is the normal stress due to snow load (100 mm water = 100 Pa), l_0 is the thickness of the crust ($l_0 = 30$ km), and E is the Young's modulus ($E = 30$ GPa). Calculated subsidence is less than one mm. Thus, we ignored the effect of local snow load.

Uncertainty calculation

Uncertainties for the various parameter estimates were determined with a Monte Carlo simulation, as follows. Random noise was added to the GPS daily solutions, scaled by the daily uncertainties. This creates a new time series, from which the five seasonal uplift variables were re-estimated using the spline technique. The process is repeated 10,000 times, producing 10,000 estimates for each parameter, for each GPS site. A histogram of these values is shown in Figure A4, for an example time series (SENU). The distribution is approximately Gaussian, and the range of values that contains 68% of the values is used to define the one sigma confidence level, also shown in Figure A4. The uncertainty analysis shows that the spline fit, which is sensitive to seasonal variations in the time series, is not sensitive to random daily position changes in the time series. As a result, the estimated uncertainties of the five seasonal parameters are small.

Appendix B: Supplementary information for Chapter 4

Note 1: Additional information on Figure 4.4

Figure 4.4 shows the sum of freshwater flux from Greenland, the Canadian Arctic Archipelago and Arctic sea ice. Grey shading in Figure 4.4 indicates propagated uncertainty. It is computed by taking the quadratic sum of the uncertainty associated with each freshwater flux estimate (Figures A10,A13,A19), and then taking the square root of the sum.

Freshwater flux from Greenland

Freshwater flux from Greenland (FWF_{GL}) is described by Bamber et al. (2012):

$$FWF_{GL} = A_{GL} - MB_{GL} \quad (A6)$$

where $A_{GL} = A_{ice} + A_{tundra}$ and $MB_{GL} = MB_{ice} + MB_{tundra}$. A_{GL} is the total accumulation in Greenland, A_{ice} is accumulation on ice and A_{tundra} is accumulation on tundra. MB_{GL} is the total mass balance of Greenland, MB_{ice} is the ice mass balance and MB_{tundra} is the snow mass balance on tundra. Since A_{GL} can be estimated from RACMO2.3 (precipitation minus sublimation/evaporation) and MB_{GL} can be estimated from GRACE observations, we can estimate the freshwater flux from Greenland directly with equation A6. Note that the accumulation predicted by RACMO2.3 is variable from year to year. We therefore smooth the accumulation with a 5-year running average (both values are shown in Figure A10).

We then examined two components of freshwater flux from Greenland (FWF_{GL}), namely freshwater flux from ice mass loss (FWF_{ice}) and freshwater flux from snow melt on tundra (FWF_{tundra}) (Figure A18):

$$FWF_{ice} = R_{ice} + D_{ice} \quad (A7)$$

$$FWF_{tundra} = R_{tundra} \quad (A8)$$

where R_{ice} is ice runoff, D_{ice} is ice discharge and R_{tundra} is tundra runoff. FWF_{GL} is already estimated using equation A6 and R_{tundra} is given by RACMO2.3 directly. Thus, we can estimate FWF_{ice} by subtracting FWF_{tundra} from FWF_{GL} .

Freshwater flux from the Canadian Arctic Archipelago(CAA)

Like FWF_{GL} , freshwater flux from the CAA (FWF_{CAA}) is composed of freshwater flux from ice mass loss FWF_{ice} and freshwater flux from snowmelt on tundra (FWF_{tundra}) (Figure A19). Glaciers in the CAA are mainly land-terminating, so freshwater flux by ice discharge is small ($5 \pm 2 \text{ Gt yr}^{-1}/0.16 \pm 0.06 \text{ mSv}$) (Gardner et al., 2011). Thus, we only consider ice runoff (R_{ice}) and neglect ice discharge (D_{ice}) for the FWF_{ice} calculation (equation A2). FWF_{tundra} thus equals tundra runoff (R_{tundra}) (equation A8). FWF_{CAA} is then derived from runoff predicted by RACMO2.3.

Changes in freshwater flux from Arctic sea ice

Freshwater sources in the Arctic Ocean include runoff from rivers and streams, ground water discharge, the difference between precipitation and evaporation ($P - E$) and sea ice formation, which forms fresh water through fractionation. All of these sources are thought to be freshening the Arctic Ocean(Haine et al., 2015).

Freshwater is exported from the Arctic Ocean as liquid water and sea ice, mainly through Fram Strait, Nares Strait and the CAA. Freshwater fluxes from the Arctic Ocean far exceed fluxes from Greenland or melting of CAA glaciers, but are also difficult to quantify. Annual fluxes through Fram Strait are thought to be about $\sim 2800 \text{ km}^3$ and $\sim 1900 \text{ km}^3$ of liquid freshwater and sea ice respectively ($\sim 140 \text{ mSv}$ total freshwater exported to the Nordic Seas and Labrador Sea) while annual fluxes through the CAA (and subsequently Davis Strait) are $\sim 2900 \text{ km}^3$ and $\sim 320 \text{ km}^3$ of liquid freshwater and sea ice respectively ($\sim 100 \text{ mSv}$ total freshwater)(Haine et al., 2015). These recent estimates do not show significant change over the last few decades, but the uncertainties are quite large, of the order of the changes we observe for Greenland (Figure 4.4).

Arctic sea ice contributes to freshwater flux in several ways. It is useful to consider two components. The first component is associated with the annual freeze-thaw cycle that

fractionates sea water into freshwater and brine (since the freezing point of brine is lower than freshwater; see Aagaard and Carmack (1989) for a review). The solid ice remains at the surface, while the liquid brine sinks, some of which is subsequently exported from the Arctic to form a component of deep water. Most of the ice melts the following summer, contributing significant freshwater. However, some ice may remain unmelted, forming multi-year ice. A large reservoir of thick multi-year ice may eventually form. If the system is in steady state, it is mainly new ice that melts each summer and contributes to freshwater flux.

The second component represents additional ice that melts during periods of extended multi-year warming. If previously accumulated multi-year ice begins to melt, sea ice volume decreases year by year. Here, we ignore the first (larger) component, because it is difficult to calculate, and focus just on changes in freshwater flux due to accelerated melting and export of sea ice.

Another variable to consider is the partitioning between freshwater that is exported from the Arctic Ocean, and freshwater that is retained. The CCSM4 climate model suggests that increased import of freshwater into the Arctic Ocean and increased sea ice melting forces increased export of freshwater(Vavrus et al., 2012). However, decadal freshening of the Arctic has been observed since 2000, indicating that some of the increased fresh water must also be retained, at least temporarily, possibly influenced by decadal changes in wind stress(Haine et al., 2015; Proshutinsky et al., 2015). Additional studies are required to refine our picture of freshwater sinks and sources.

We use the annual minimum of Arctic sea ice volume, and its long term change, to estimate changes in the freshwater flux from Arctic sea ice. Three data sets (sea ice volume, extent and area) are used. We obtained the monthly Arctic sea ice volume time series from the Pan-Arctic Ice Ocean Modeling and Assimilation System (PIOMAS)(Zhang and Rothrock, 2003). Monthly Arctic sea ice extent and sea ice area time series are obtained from the National Snow and Ice Data Center (NSIDC)(Fetterer et al., aily). To convert extent and area to volume we assume the average thickness of Arctic sea ice is 2 m.

Many studies report a long-term decline in Arctic sea ice(Cavalieri et al., 2003; Kwok et al., 2009; Maslowski et al., 2012). The sea ice data compiled here also show a clear trend of accelerating loss, with the loss rate increasing in the 1990s (Figure A12). To determine the timing of this change more accurately, we fit all three time series with a two-slope model, where the trend change occurs at a ramp time. We conducted a one dimensional grid search from 1979 to 2013 with 1 year spacing to determine the best-fit ramp time. Our results suggest that the melting rate of Artic sea ice started to increase around 1996 (based on the ice extent and area data sets) or 1997 (based on the ice volume data set) (Figure A12a), in agreement with Comiso et al. (2008).

The two-slope model is good at detecting the onset time of accelerated melting, but poorly describes the time-varying melt rate. To better estimate this rate, we also fit the three time series with a linear state space model, described below.

A general linear state space model can be represented by an observation equation and a state evolution equation as(Durbin and Koopman, 2012):

$$\mathbf{y}_t = \mathbf{F}_t \mathbf{X}_t + \mathbf{v}_t \quad (\text{A9})$$

$$\mathbf{x}_t = \mathbf{G}_t \mathbf{X}_{t-1} + \mathbf{w}_t \quad (\text{A10})$$

where \mathbf{y}_t is the observation vector at time t ($t = 1, 2, 3, \dots, n$), \mathbf{x}_t is the state vector, \mathbf{F}_t is the measurement matrix and \mathbf{G}_t is the state transition matrix for the time step from time t to time $t + 1$. \mathbf{v}_t and \mathbf{w}_t are assumed to be Gaussian with zero mean and measurement noise covariance matrix \mathbf{V}_t and process noise covariance matrix \mathbf{W}_t . In our analysis, \mathbf{y}_t is a 1×1 matrix and equals annual minimum Arctic sea ice volume. $\mathbf{x}_t = [\mu_t \ \alpha_t]^T$, where μ_t is the initial volume state, α_t is the melting rate state. \mathbf{V}_t is a 1×1 matrix and equals the observation uncertainty (1500 km^3). We use the same strategy described in Laine et al. (2014), defining \mathbf{F}, \mathbf{G} , and \mathbf{W} to be time-invariant, so they can be represented by:

$$\mathbf{F} = \begin{bmatrix} 1 & 0 \end{bmatrix} \quad (\text{A11})$$

$$\mathbf{G} = \begin{bmatrix} 1 & 1 \\ 0 & 1 \end{bmatrix} \quad (\text{A12})$$

$$\text{diag}(\mathbf{W}) = \begin{bmatrix} 0 & \sigma_{rate}^2 \end{bmatrix} \quad (\text{A13})$$

σ_{rate} describes allowed change of sea ice volume in a year, with units of $\text{km}^3 \text{ yr}^{-1}$. Here, we assume $\sigma_{rate} = 40 \text{ km}^3 \text{ yr}^{-1}$. This value balances the trade-off between goodness of fit and smoothing. We then adopt the Kalman filtering technique to estimate the time-dependent state vectors described in the above state space model. We use the software described in Laine et al. (2014) to implement the Kalman filter.

Figure A12b shows the annual minimum sea ice volume time series and the linear state space model for the three data sets. Figure A13 shows the estimated long-term freshwater flux (mSv) from Arctic sea ice for the three data sets. Note that the freshwater flux from Arctic sea ice is calculated by multiplying the estimated melting rate ($\text{km}^3 \text{ yr}^{-1}$) and the density of sea ice (900 kg m^{-3}). Melting rate derived from the volume data set is somewhat higher compared to the other two data sets. However, all three data sets show accelerated melting beginning between 1990 and 2000.

Portion of increased freshwater flux that reaches the Labrador Sea

We estimate ~ 20 mSv of increased freshwater flux into the sub-polar North Atlantic over the last two decades, focusing on three sources that are likely to influence Labrador Sea convection and can be estimated by remote techniques: the Greenland Ice Sheet (GrIS), glaciers in the CAA and changes in Arctic sea ice. We recognize that there are additional freshwater sources such as river runoff and P – E, and that these may also have increased in the last few decades(Peterson et al., 2006) but are difficult to quantify(Bacon et al., 2015). Also, our sea ice change estimate does not capture all the freshwater flux associated with sea ice formation. Hence our estimate of changes in freshwater flux is a minimum estimate. However, it is also important to determine what fraction of our freshwater flux change estimate winds up in the Labrador Sea.

On the east side of Greenland, Arctic Ocean freshwater (liquid freshwater plus sea ice) is exported through Fram Strait. The sea ice melts in the East Greenland

Current (EGC), adding to the liquid component. Some of the Arctic freshwater is lost to the Nordic Seas, but the amounts are not well known. Limited in situ data may not capture annual or longer term variation, but do allow a crude estimate of the partitioning of freshwater flux during the sampling period through several key flux gates. Using a reference salinity of 35.20, Dickson et al. (2007) estimate that 148 mSv of freshwater (liquid freshwater plus sea ice) is exported from Fram Strait. This represents freshwater from all sources, including river runoff and $P - E$, but in the calculations below we assume that freshwater sourced just from Arctic sea ice is similarly partitioned. Note that the numbers change if a different reference salinity is used, however overall partitioning is less affected. 51 mSv of the freshwater is exported directly to the deep Atlantic in dense water overflows, leaving 97 mSv in the EGC, or about 65% of the original flux through Fram Strait. An additional 54 mSv of freshwater is added from other sources (including runoff, mass loss of GrIS and $P - E$), such that 151 mSv of freshwater is transported by the EGC through Denmark Strait. For comparison, a recent study of Våge et al. (2013) estimated the southward freshwater flux transported by the EGC through Denmark Strait is about 137 mSv, using a reference salinity of 34.80. Freshwater then continues southward in the EGC and the East Greenland Coastal Current (EGCC), an inner branch of the EGC. The EGC-EGCC system is shelf trapped with little freshwater lost offshore as it flows southwards towards Cape Farewell, and receives added freshwater from Greenland mass loss, sea ice melt and $P - E$. Sutherland and Pickart (2008) estimate 37 mSv (reference salinity is 34.80) of freshwater flux added to the EGC-EGCC system between 68 ° N and Cape Farewell near 60 ° N, based on measurements in 2004. The West Greenland Current (WGC) connects with the EGC-EGCC, transporting all of the freshwater that rounds Cape Farewell and any added freshwater from west Greenland northward, and into the Labrador Sea. Data in Myers et al. (2007, 2009) and Rykova et al. (2015) as well as modeling studies (Kawasaki and Hasumi, 2014; Saenko et al., 2014) show that virtually all of the freshwater that rounds Cape Farewell eventually ends up in the Labrador Sea. Thus, on the east side of Greenland, approximately 65% of Arctic Ocean freshwater

exported through Fram Strait, and virtually all of the freshwater from Greenland that is added to the EGC-EGCC, is focused towards the Labrador Sea.

On the west side of Greenland, freshwater export from the Arctic Ocean (liquid freshwater plus sea ice) and freshwater from CAA glaciers and GrIS (melting plus calving) enters Baffin Bay, and then exits through Davis Strait in the Baffin Island Current (Haine et al., 2015; Curry et al., 2011, 2014). This flows south into the Labrador Current, joined by freshwater outflow from Hudson Strait (Straneo and Saucier, 2008; St-Laurent et al., 2011). All of this freshwater then flows south in the Labrador Current along the Labrador shelf. Myers (2005) suggest that transport into the northern Labrador Sea interior here is relatively small, while Schmidt and Send (2007) and McGeehan and Maslowski (2011) suggest that some transport to the interior does occur here. The larger fraction of freshwater is exported farther south, around Flemish Cap and the Grand Banks (Loder et al., 1998; Fratantoni and Pickart, 2007; Fratantoni and McCartney, 2010), where much of it will be incorporated into the sub-polar gyre, eventually re-entering the EGC-EGCC and WGC, and ultimately, the Labrador Sea. Less than 25% of the freshwater passes south of the Grand Banks. Thus, at least 75% of the freshwater exported on the west side of Greenland from the three sources cited above (Arctic sea ice, GrIS and glaciers in the CAA) ultimately winds up in the Labrador Sea, either directly or indirectly through the sub-polar gyre.

With these various assumption and estimates, of the 20 mSv total increase of freshwater flux that we observe, at least 14 mSv (70%, of which 9 mSv is from GrIS and CAA and 5 mSv from Arctic sea ice), is advected into the Labrador Sea.

Since most of the 137 mSv of freshwater flux passing through Denmark Strait (Våge et al., 2013) on the east side of Greenland rounds Cape Farewell, and at least 75% of the 100 mSv of freshwater flux passing through Davis Strait (Haine et al., 2015) on the west side of Greenland eventually makes it to the Labrador Sea, total freshwater flux into the Labrador Sea likely exceeds 200 mSv. Thus, our estimate of increased freshwater flux into the Labrador Sea (14 – 20 mSv) may only represent 7 – 10% of the

total. Future observations are required to refine these estimates and characterize their temporal variability.

Our study suggests that the sub-polar gyre's coastal currents focus increased freshwater from Greenland into the Labrador Sea, suppressing winter convection. Perhaps in the future the Nordic Seas will become more important relative to the Labrador Sea in terms of producing North Atlantic Deep Water and the southward return flow of the AMOC.

Appendix C: Copyright permission

2/1/2016

RightsLink Printable License

JOHN WILEY AND SONS LICENSE TERMS AND CONDITIONS

Feb 01, 2016

This Agreement between QIAN YANG ("You") and John Wiley and Sons ("John Wiley and Sons") consists of your license details and the terms and conditions provided by John Wiley and Sons and Copyright Clearance Center.

License Number 3800280355362
License date Feb 01, 2016
Licensed Content Publisher John Wiley and Sons
Licensed Content Publication Geochemistry, Geophysics, Geosystems
Licensed Content Title Annual variation of coastal uplift in Greenland as an indicator of variable and accelerating ice mass loss
Licensed Content Author Qian Yang, Shimon Wdowinski, Timothy H. Dixon
Licensed Content Date May 20, 2013
Pages 21
Type of use Dissertation/Thesis
Requestor type Author of this Wiley article
Format Electronic
Portion Full article
Will you be translating? No
Title of your thesis / dissertation Applications of Satellite Geodesy in Environmental and Climate Change
Expected completion date May 2016
Expected size (number of pages) 210
Requestor Location QIAN YANG

TAMPA, FL 33613
United States
Attn: QIAN YANG

Billing Type Invoice
Billing Address QIAN YANG

TAMPA, FL 33613
United States
Attn: QIAN YANG

Total 0.00 USD

Terms and Conditions

TERMS AND CONDITIONS

This copyrighted material is owned by or exclusively licensed to John Wiley & Sons, Inc. or one of its group companies (each a "Wiley Company") or handled on behalf of a society with

which a Wiley Company has exclusive publishing rights in relation to a particular work (collectively "WILEY"). By clicking "accept" in connection with completing this licensing transaction, you agree that the following terms and conditions apply to this transaction (along with the billing and payment terms and conditions established by the Copyright Clearance Center Inc., ("CCC's Billing and Payment terms and conditions"), at the time that you opened your RightsLink account (these are available at any time at <http://myaccount.copyright.com>).

Terms and Conditions

- The materials you have requested permission to reproduce or reuse (the "Wiley Materials") are protected by copyright.
- You are hereby granted a personal, non-exclusive, non-sub licensable (on a stand-alone basis), non-transferable, worldwide, limited license to reproduce the Wiley Materials for the purpose specified in the licensing process. This license, **and any CONTENT (PDF or image file) purchased as part of your order**, is for a one-time use only and limited to any maximum distribution number specified in the license. The first instance of republication or reuse granted by this license must be completed within two years of the date of the grant of this license (although copies prepared before the end date may be distributed thereafter). The Wiley Materials shall not be used in any other manner or for any other purpose, beyond what is granted in the license. Permission is granted subject to an appropriate acknowledgement given to the author, title of the material/book/journal and the publisher. You shall also duplicate the copyright notice that appears in the Wiley publication in your use of the Wiley Material. Permission is also granted on the understanding that nowhere in the text is a previously published source acknowledged for all or part of this Wiley Material. Any third party content is expressly excluded from this permission.
- With respect to the Wiley Materials, all rights are reserved. Except as expressly granted by the terms of the license, no part of the Wiley Materials may be copied, modified, adapted (except for minor reformatting required by the new Publication), translated, reproduced, transferred or distributed, in any form or by any means, and no derivative works may be made based on the Wiley Materials without the prior permission of the respective copyright owner.**For STM Signatory Publishers clearing permission under the terms of the [STM Permissions Guidelines](#) only, the terms of the license are extended to include subsequent editions and for editions in other languages, provided such editions are for the work as a whole in situ and does not involve the separate exploitation of the permitted figures or extracts,** You may not alter, remove or suppress in any manner any copyright, trademark or other notices displayed by the Wiley Materials. You may not license, rent, sell, loan, lease, pledge, offer as security, transfer or assign the Wiley Materials on a stand-alone basis, or any of the rights granted to you hereunder to any other person.
- The Wiley Materials and all of the intellectual property rights therein shall at all times remain the exclusive property of John Wiley & Sons Inc, the Wiley Companies, or their respective licensors, and your interest therein is only that of having possession of and the right to reproduce the Wiley Materials pursuant to Section 2 herein during the continuance of this Agreement. You agree that you own no right, title or interest in or to the Wiley Materials or any of the intellectual property rights therein. You shall have no rights hereunder other than the license as provided for above in Section 2. No right, license or interest to any trademark, trade name, service mark or other branding ("Marks") of WILEY or its licensors is granted hereunder, and you agree that you shall not assert any such right, license or interest with respect thereto

- NEITHER WILEY NOR ITS LICENSORS MAKES ANY WARRANTY OR REPRESENTATION OF ANY KIND TO YOU OR ANY THIRD PARTY, EXPRESS, IMPLIED OR STATUTORY, WITH RESPECT TO THE MATERIALS OR THE ACCURACY OF ANY INFORMATION CONTAINED IN THE MATERIALS, INCLUDING, WITHOUT LIMITATION, ANY IMPLIED WARRANTY OF MERCHANTABILITY, ACCURACY, SATISFACTORY QUALITY, FITNESS FOR A PARTICULAR PURPOSE, USABILITY, INTEGRATION OR NON-INFRINGEMENT AND ALL SUCH WARRANTIES ARE HEREBY EXCLUDED BY WILEY AND ITS LICENSORS AND WAIVED BY YOU.
- WILEY shall have the right to terminate this Agreement immediately upon breach of this Agreement by you.
- You shall indemnify, defend and hold harmless WILEY, its Licensors and their respective directors, officers, agents and employees, from and against any actual or threatened claims, demands, causes of action or proceedings arising from any breach of this Agreement by you.
- IN NO EVENT SHALL WILEY OR ITS LICENSORS BE LIABLE TO YOU OR ANY OTHER PARTY OR ANY OTHER PERSON OR ENTITY FOR ANY SPECIAL, CONSEQUENTIAL, INCIDENTAL, INDIRECT, EXEMPLARY OR PUNITIVE DAMAGES, HOWEVER CAUSED, ARISING OUT OF OR IN CONNECTION WITH THE DOWNLOADING, PROVISIONING, VIEWING OR USE OF THE MATERIALS REGARDLESS OF THE FORM OF ACTION, WHETHER FOR BREACH OF CONTRACT, BREACH OF WARRANTY, TORT, NEGLIGENCE, INFRINGEMENT OR OTHERWISE (INCLUDING, WITHOUT LIMITATION, DAMAGES BASED ON LOSS OF PROFITS, DATA, FILES, USE, BUSINESS OPPORTUNITY OR CLAIMS OF THIRD PARTIES), AND WHETHER OR NOT THE PARTY HAS BEEN ADVISED OF THE POSSIBILITY OF SUCH DAMAGES. THIS LIMITATION SHALL APPLY NOTWITHSTANDING ANY FAILURE OF ESSENTIAL PURPOSE OF ANY LIMITED REMEDY PROVIDED HEREIN.
- Should any provision of this Agreement be held by a court of competent jurisdiction to be illegal, invalid, or unenforceable, that provision shall be deemed amended to achieve as nearly as possible the same economic effect as the original provision, and the legality, validity and enforceability of the remaining provisions of this Agreement shall not be affected or impaired thereby.
- The failure of either party to enforce any term or condition of this Agreement shall not constitute a waiver of either party's right to enforce each and every term and condition of this Agreement. No breach under this agreement shall be deemed waived or excused by either party unless such waiver or consent is in writing signed by the party granting such waiver or consent. The waiver by or consent of a party to a breach of any provision of this Agreement shall not operate or be construed as a waiver of or consent to any other or subsequent breach by such other party.
- This Agreement may not be assigned (including by operation of law or otherwise) by you without WILEY's prior written consent.
- Any fee required for this permission shall be non-refundable after thirty (30) days from receipt by the CCC.

- These terms and conditions together with CCC's Billing and Payment terms and conditions (which are incorporated herein) form the entire agreement between you and WILEY concerning this licensing transaction and (in the absence of fraud) supersedes all prior agreements and representations of the parties, oral or written. This Agreement may not be amended except in writing signed by both parties. This Agreement shall be binding upon and inure to the benefit of the parties' successors, legal representatives, and authorized assigns.
- In the event of any conflict between your obligations established by these terms and conditions and those established by CCC's Billing and Payment terms and conditions, these terms and conditions shall prevail.
- WILEY expressly reserves all rights not specifically granted in the combination of (i) the license details provided by you and accepted in the course of this licensing transaction, (ii) these terms and conditions and (iii) CCC's Billing and Payment terms and conditions.
- This Agreement will be void if the Type of Use, Format, Circulation, or Requestor Type was misrepresented during the licensing process.
- This Agreement shall be governed by and construed in accordance with the laws of the State of New York, USA, without regards to such state's conflict of law rules. Any legal action, suit or proceeding arising out of or relating to these Terms and Conditions or the breach thereof shall be instituted in a court of competent jurisdiction in New York County in the State of New York in the United States of America and each party hereby consents and submits to the personal jurisdiction of such court, waives any objection to venue in such court and consents to service of process by registered or certified mail, return receipt requested, at the last known address of such party.

WILEY OPEN ACCESS TERMS AND CONDITIONS

Wiley Publishes Open Access Articles in fully Open Access Journals and in Subscription journals offering Online Open. Although most of the fully Open Access journals publish open access articles under the terms of the Creative Commons Attribution (CC BY) License only, the subscription journals and a few of the Open Access Journals offer a choice of Creative Commons Licenses. The license type is clearly identified on the article.

The Creative Commons Attribution License

The [Creative Commons Attribution License \(CC-BY\)](#) allows users to copy, distribute and transmit an article, adapt the article and make commercial use of the article. The CC-BY license permits commercial and non-

Creative Commons Attribution Non-Commercial License

The [Creative Commons Attribution Non-Commercial \(CC-BY-NC\)License](#) permits use, distribution and reproduction in any medium, provided the original work is properly cited and is not used for commercial purposes.(see below)

Creative Commons Attribution-Non-Commercial-NoDerivs License

The [Creative Commons Attribution Non-Commercial-NoDerivs License](#) (CC-BY-NC-ND) permits use, distribution and reproduction in any medium, provided the original work is properly cited, is not used for commercial purposes and no modifications or adaptations are made. (see below)

Use by commercial "for-profit" organizations

Use of Wiley Open Access articles for commercial, promotional, or marketing purposes

requires further explicit permission from Wiley and will be subject to a fee.
Further details can be found on Wiley Online Library
<http://olabout.wiley.com/WileyCDA/Section/id-410895.html>

Other Terms and Conditions:

v1.10 Last updated September 2015

Questions? customercare@copyright.com or +1-855-239-3415 (toll free in the US) or +1-978-646-2777.

Author Requests

If you are the author of this content (or his/her designated agent) please read the following. Since 2003, ownership of copyright in original research articles remains with the Authors*, and provided that, when reproducing the Contribution or extracts from it, the Authors acknowledge first and reference publication in the Journal, the Authors retain the following non-exclusive rights:

- a. To reproduce the Contribution in whole or in part in any printed volume (book or thesis) of which they are the author(s).
- b. They and any academic institution where they work at the time may reproduce the Contribution for the purpose of course teaching.
- c. To reuse figures or tables created by them and contained in the Contribution in other works created by them.
- d. To post a copy of the Contribution as accepted for publication after peer review (in Word or Tex format) on the Author's own web site, or the Author's institutional repository, or the Author's funding body's archive, six months after publication of the printed or online edition of the Journal, provided that they also link to the Journal article on NPG's web site (eg through the DOI).

NPG encourages the self-archiving of the accepted version of your manuscript in your funding agency's or institution's repository, six months after publication. This policy complements the recently announced policies of the US National Institutes of Health, Wellcome Trust and other research funding bodies around the world. NPG recognizes the efforts of funding bodies to increase access to the research they fund, and we strongly encourage authors to participate in such efforts.

Authors wishing to use the published version of their article for promotional use or on a web site must request in the normal way.

If you require further assistance please read NPG's online author reuse guidelines.

Note: *British Journal of Cancer* maintains copyright policies of its own that are different from the general NPG policies. Please consult this journal to learn more.

* Commissioned material is still subject to copyright transfer conditions

Personal use

Authors can use their articles, in full or in part, for a wide range of scholarly, non-commercial purposes as outlined below:

- Use by an author in the author's classroom teaching (including distribution of copies, paper or electronic)
- Distribution of copies (including through e-mail) to known research colleagues for their personal use (but not for Commercial Use)
- Inclusion in a thesis or dissertation (provided that this is not to be published commercially)
- Use in a subsequent compilation of the author's works
- Extending the Article to book-length form
- Preparation of other derivative works (but not for Commercial Use)
- Otherwise using or re-using portions or excerpts in other works

These rights apply for all Elsevier authors who publish their article as either a subscription article or an open access article. In all cases we require that all Elsevier authors always include a full acknowledgement and, if appropriate, a link to the final published version hosted on Science Direct.

Appendix D: References

- Aagaard, K. and Carmack, E. C. (1989). The role of sea ice and other fresh water in the arctic circulation. *Journal of Geophysical Research: Oceans (1978–2012)*, 94(C10):14485–14498.
- Bacon, S., Aksenov, Y., Fawcett, S., and Madec, G. (2015). Arctic mass, freshwater and heat fluxes: methods and modelled seasonal variability. *Phil. Trans. R. Soc. A*, 373(2052):20140169.
- Bamber, J., den Broeke, M., Ettema, J., Lenaerts, J., and Rignot, E. (2012). Recent large increases in freshwater fluxes from greenland into the north atlantic. *Geophysical Research Letters*, 39(19).
- Box, J. E. and Colgan, W. (2013). Greenland ice sheet mass balance reconstruction. part iii: Marine ice loss and total mass balance (1840–2010). *Journal of Climate*, 26(18):6990–7002.
- Carstensen, L. and Jørgensen, B. (2011). Weather and climate data from greenland 1958-2010 danish meteorological institute. Technical report, Technical Report.
- Cavalieri, D., Parkinson, C., and Vinnikov, K. Y. (2003). 30-year satellite record reveals contrasting arctic and antarctic decadal sea ice variability. *Geophysical Research Letters*, 30(18).
- Comiso, J. C., Parkinson, C. L., Gersten, R., and Stock, L. (2008). Accelerated decline in the arctic sea ice cover. *Geophysical Research Letters*, 35(1).
- Curry, B., Lee, C., and Petrie, B. (2011). Volume, freshwater, and heat fluxes through davis strait, 2004-05*. *Journal of Physical Oceanography*, 41(3):429–436.
- Curry, B., Lee, C., Petrie, B., Moritz, R., and Kwok, R. (2014). Multiyear volume, liquid freshwater, and sea ice transports through davis strait, 2004–10*. *Journal of Physical Oceanography*, 44(4):1244–1266.

- Darwin, G. (1882). Xlvi. on variations in the vertical due to elasticity of the earth's surface. *The London, Edinburgh, and Dublin Philosophical Magazine and Journal of Science*, 14(90):409–427.
- Dickson, R., Rudels, B., Dye, S., Karcher, M., Meincke, J., and Yashayaev, I. (2007). Current estimates of freshwater flux through arctic and subarctic seas. *Progress in Oceanography*, 73(3):210–230.
- Dong, D., Fang, P., Bock, Y., Cheng, M., and Miyazaki, S. (2002). Anatomy of apparent seasonal variations from gps-derived site position time series. *Journal of Geophysical Research: Solid Earth (1978–2012)*, 107(B4):ETG–9.
- Durbin, J. and Koopman, S. J. (2012). *Time series analysis by state space methods*. Number 38. Oxford University Press.
- Enderlin, E. M., Howat, I. M., Jeong, S., Noh, M.-J., Angelen, J. H., and Broeke, M. R. (2014). An improved mass budget for the greenland ice sheet. *Geophysical Research Letters*, 41(3):866–872.
- Farrell, W. (1972). Deformation of the earth by surface loads. *Reviews of Geophysics*, 10(3):761–797.
- Fetterer, F., Knowles, K., Meier, W., and Savoie, M. (2002, updated daily). Sea ice index. pages National Snow and Ice Data Center, Boulder, Colorado.
- Fratantoni, P. S. and McCartney, M. S. (2010). Freshwater export from the labrador current to the north atlantic current at the tail of the grand banks of newfoundland. *Deep Sea Research Part I: Oceanographic Research Papers*, 57(2):258–283.
- Fratantoni, P. S. and Pickart, R. S. (2007). The western north atlantic shelfbreak current system in summer. *Journal of Physical Oceanography*, 37(10):2509–2533.
- Gardner, A. S., Moholdt, G., Wouters, B., Wolken, G. J., Burgess, D. O., Sharp, M. J., Cogley, J. G., Braun, C., and Labine, C. (2011). Sharply increased mass loss from glaciers and ice caps in the canadian arctic archipelago. *Nature*, 473(7347):357–360.

- Good, S. A., Martin, M. J., and Rayner, N. A. (2013). En4: quality controlled ocean temperature and salinity profiles and monthly objective analyses with uncertainty estimates. *Journal of Geophysical Research: Oceans*, 118(12):6704–6716.
- Haine, T. W., Curry, B., Gerdes, R., Hansen, E., Karcher, M., Lee, C., Rudels, B., Spreen, G., de Steur, L., Stewart, K. D., et al. (2015). Arctic freshwater export: Status, mechanisms, and prospects. *Global and Planetary Change*, 125:13–35.
- Kalnay, E., Kanamitsu, M., Kistler, R., Collins, W., Deaven, D., Gandin, L., Iredell, M., Saha, S., White, G., Woollen, J., et al. (1996). The ncep/ncar 40-year reanalysis project. *Bulletin of the American meteorological Society*, 77(3):437–471.
- Kawasaki, T. and Hasumi, H. (2014). Effect of freshwater from the west greenland current on the winter deep convection in the labrador sea. *Ocean Modelling*, 75:51–64.
- Kwok, R., Cunningham, G., Wensnahan, M., Rigor, I., Zwally, H., and Yi, D. (2009). Thinning and volume loss of the arctic ocean sea ice cover: 2003–2008. *Journal of Geophysical Research: Oceans (1978–2012)*, 114(C7).
- Laine, M., Latva-Pukkila, N., and Kyrölä, E. (2014). Analysing time-varying trends in stratospheric ozone time series using the state space approach. *Atmospheric Chemistry and Physics*, 14(18):9707–9725.
- Lenaerts, J., Angelen, J. H., Broeke, M. R., Gardner, A. S., Wouters, B., and Meijgaard, E. (2013). Irreversible mass loss of canadian arctic archipelago glaciers. *Geophysical Research Letters*, 40(5):870–874.
- Loder, J. W., Petrie, B., and Gawarkiewicz, G. (1998). The coastal ocean off northeastern north america: A large-scale view. *The sea*, 11:105–133.
- Magie, W. F. (1969). A source book in physics.
- Maslowski, W., Clement Kinney, J., Higgins, M., and Roberts, A. (2012). The future of arctic sea ice. *Annual Review of Earth and Planetary Sciences*, 40:625–654.

- McGeehan, T. and Maslowski, W. (2011). Impact of shelf-basin freshwater transport on deep convection in the western labrador sea. *Journal of Physical Oceanography*, 41(11):2187–2210.
- Myers, P. G. (2005). Impact of freshwater from the canadian arctic archipelago on labrador sea water formation. *Geophysical Research Letters*, 32(6).
- Myers, P. G., Donnelly, C., and Ribergaard, M. H. (2009). Structure and variability of the west greenland current in summer derived from 6 repeat standard sections. *Progress in Oceanography*, 80(1):93–112.
- Myers, P. G., Josey, S. A., Wheler, B., and Kulan, N. (2007). Interdecadal variability in labrador sea precipitation minus evaporation and salinity. *Progress in Oceanography*, 73(3):341–357.
- Peterson, B. J., McClelland, J., Curry, R., Holmes, R. M., Walsh, J. E., and Aagaard, K. (2006). Trajectory shifts in the arctic and subarctic freshwater cycle. *Science*, 313(5790):1061–1066.
- Petrov, L. and Boy, J.-P. (2004). Study of the atmospheric pressure loading signal in very long baseline interferometry observations. *Journal of Geophysical Research: Solid Earth (1978–2012)*, 109(B3).
- Proshutinsky, A., Dukhovskoy, D., Timmermans, M.-L., Krishfield, R., and Bamber, J. L. (2015). Arctic circulation regimes. *Phil. Trans. R. Soc. A*, 373(2052):20140160.
- Rykova, T., Straneo, F., and Bower, A. S. (2015). Seasonal and interannual variability of the west greenland current system in the labrador sea in 1993–2008. *Journal of Geophysical Research: Oceans*, 120(2):1318–1332.
- Saenko, O. A., Dupont, F., Yang, D., Myers, P. G., Yashayaev, I., and Smith, G. C. (2014). Role of resolved and parameterized eddies in the labrador sea balance of heat and buoyancy. *Journal of Physical Oceanography*, 44(12):3008–3032.

- Schmidt, S. and Send, U. (2007). Origin and composition of seasonal labrador sea fresh-water. *Journal of physical oceanography*, 37(6):1445–1454.
- St-Laurent, P., Straneo, F., Dumais, J.-F., and Barber, D. G. (2011). What is the fate of the river waters of hudson bay? *Journal of Marine Systems*, 88(3):352–361.
- Straneo, F. and Saucier, F. (2008). The outflow from hudson strait and its contribution to the labrador current. *Deep Sea Research Part I: Oceanographic Research Papers*, 55(8):926–946.
- Sutherland, D. A. and Pickart, R. S. (2008). The east greenland coastal current: Structure, variability, and forcing. *Progress in Oceanography*, 78(1):58–77.
- Våge, K., Pickart, R. S., Spall, M. A., Moore, G., Valdimarsson, H., Torres, D. J., Erofeeva, S. Y., and Nilsen, J. E. Ø. (2013). Revised circulation scheme north of the denmark strait. *Deep Sea Research Part I: Oceanographic Research Papers*, 79:20–39.
- Vandam, T. M., Blewitt, G., and Heflin, M. B. (1994). Atmospheric pressure loading effects on global positioning system coordinate determinations. *Journal of Geophysical Research: Solid Earth (1978–2012)*, 99(B12):23939–23950.
- Vavrus, S. J., Holland, M. M., Jahn, A., Bailey, D. A., and Blazey, B. A. (2012). Twenty-first-century arctic climate change in ccsm4. *Journal of Climate*, 25(8):2696–2710.
- Zhang, J. and Rothrock, D. (2003). Modeling global sea ice with a thickness and enthalpy distribution model in generalized curvilinear coordinates. *Monthly Weather Review*, 131(5):845–861.

Table A1: Comparison of seasonal uplift patterns parameters estimated from fitting GPS vertical time series with and without atmospheric loading correction to a cubic spline model.

	2008		2009		2010	
	No APLC	APLC	NO APLC	APLC	NO APLC	APLC
Start time (doy)	N/D	N/D	146	150	142	153
End time (doy)	320	315	323	321	327	332
Duration (days)	N/D	N/D	177	171	185	179
Uplift (mm)	N/D	N/D	9.2	11.5	16	19.3
Uplift rate(10^{-2} mm day $^{-1}$)	N/D	N/D	5.2	6.7	8.7	10.8

- NO ALC mean no atmospheric loading correction is applied; ALC means atmospheric loading correction is applied.
- Other symbols are the same as in Table 3.1.

Table A2: List of meteorological stations

WMO-ID and station name	Latitude (deg N)	Longitude (deg E)	Elevation (m.a.s)	Near GPS site	Horizontal dist (km)	Elevation Diff (m)	Distance (km)
04205 Mitt.Qaanaaq*	77.48	-69.38	16	DKSG	231.4	579	231.4
				MARG	95.7	641	95.7
				THU3	105.5	20	105.5
04208 Kitsissorsuit	74.03	-57.82	40	KULL	63.4	54	63.4
04211 Mitt.Upernivik	72.78	-56.13	126	SRMP	58.8	218	58.8
04213 Mitt.Qaarsut	70.73	-52.70	88	QAAR	0.8	35	0.8
				RINK	138.4	1252	138.4
				KAGA	49.5	120	49.5
04221 Mitt.Iiulissat	69.23	-51.07	29	KELY	10.8	194	10.8
04231 Kangerlussuaq*	67.02	-51.70	50	SENU	71.6	634	71.6
				QAQ1	1.0	78	1.0
				PLPK	123.1	56	123.1
04360 Tasiilaq*	65.60	-37.62	53	HEL2	93.1	374	93.1
				KULU	21.5	14	21.5
				KSNB	158.6	1624	158.6
04373 Ikermit	64.78	-40.30	85	HJOR	157.3	680	157.3
				LYNS	39.6	89	39.6
				TREO	76.2	38	76.2
				TIMM	268.3	230	268.3

- WMO-ID and station information are provided by Technical Report 11-10 of Danish Meteorological Institute.
- Horizontal dist: horizontal distance between GPS site and nearby MET station.
- Elevation diff: elevation difference between GPS site and nearby MET station.

Table A3: Five parameters of seasonal uplift patterns estimated from fitting GPS vertical data to a cubic spline model and parameters describing both atmospheric and oceanic condition at each GPS site.

Year	2008	2009	2010
DKSG			
Start time (doy)	136±12	233±7	197±5
End time (doy)	370±7	382±4	359±5
Duration (days)	234±12	149±7	162±6
Uplift (mm)	5.2±0.8	8.3±0.8	8.1±1.0
Uplift rate (10^{-2} mm day $^{-1}$)	2.2±0.4	5.6±0.4	5.0±0.5
AMSAT (° C)	-9.2	-9.0	-6.8
CAPDD (days)	113	107	116
AMSSWT (° C)	0.5	0.3	0.5
HEL2			
Start time (doy)	144±5	154±5	174±2
End time (doy)	348±3	350±3	361±2
Duration (days)	204±5	196±5	187±3
Uplift (mm)	12.2±0.7	9.0±0.7	19.0±0.8
Uplift rate (10^{-2} mm day $^{-1}$)	6.0±0.4	4.6±0.3	10.2±0.4
AMSAT (° C)	-0.5	-0.2	1.0
CAPDD (days)	180	183	188
AMSSWT (° C)	5.0	4.7	5.3
HJOR			
Start time (doy)	133±8	174±7	155±3
End time (doy)	336±3	344±3	346±2
Duration (days)	224±8	169±6	190±3
Uplift (mm)	12.5±0.7	7.0±0.6	18.3±0.7

Uplift rate (10^{-2} mm day $^{-1}$)	5.6 ± 0.4	4.2 ± 0.3	9.6 ± 0.4
AMSAT ($^{\circ}$ C)	-1.4	-1.0	0.5
CAPDD (days)	155	155	195
AMSSWT ($^{\circ}$ C)	5.4	5.1	5.8

KAGA

Start time (doy)	149 ± 8	186 ± 4	158 ± 3
End time (doy)	367 ± 3	362 ± 3	338 ± 2
Duration (days)	218 ± 8	177 ± 4	180 ± 3
Uplift (mm)	7.6 ± 0.7	8.2 ± 0.7	16.7 ± 0.8
Uplift rate (10^{-2} mm day $^{-1}$)	3.5 ± 0.4	4.7 ± 0.4	9.3 ± 0.4
AMSAT ($^{\circ}$ C)	-3.7	-3.2	0.0
CAPDD (days)	148	144	182
AMSSWT ($^{\circ}$ C)	2.0	1.6	2.3

KELY

Start time (doy)	153 ± 28	205 ± 74	108 ± 36
End time (doy)	356 ± 21	373 ± 54	335 ± 12
Duration (days)	203 ± 29	169 ± 75	228 ± 35
Uplift (mm)	6.4 ± 2.2	2.1 ± 2.2	14.1 ± 2.5
Uplift rate (10^{-2} mm day $^{-1}$)	3.2 ± 0.4	1.2 ± 0.5	6.2 ± 0.6
AMSAT ($^{\circ}$ C)	-4.4	-4.7	-0.2
CAPDD (days)	163	148	196
AMSSWT ($^{\circ}$ C)	2.5	2.3	3.1

KSNB

Start time (doy)	133 ± 10	221 ± 5	183 ± 4
End time (doy)	370 ± 5	366 ± 3	375 ± 4
Duration (days)	238 ± 10	145 ± 5	192 ± 5

Uplift (mm)	9.6 ± 0.8	7.6 ± 0.6	12.0 ± 0.8
Uplift rate (10^{-2} mm day $^{-1}$)	4.1 ± 0.4	5.2 ± 0.4	6.3 ± 0.4
AMSAT (° C)	-1.3	-0.6	0.5
CAPDD (days)	153	170	192
AMSSWT (° C)	5.0	4.8	5.4

KULL

Start time (doy)	247 ± 9	250 ± 4	208 ± 5
End time (doy)	393 ± 5	399 ± 5	355 ± 4
Duration (days)	146 ± 8	149 ± 5	147 ± 5
Uplift (mm)	6.0 ± 0.7	8.5 ± 0.7	6.5 ± 0.8
Uplift rate (10^{-2} mm day $^{-1}$)	4.1 ± 0.4	5.7 ± 0.4	4.4 ± 0.4
AMSAT (°C)	-7.4	-7.0	-4.7
CAPDD (days)	108	108	138
AMSSWT (°C)	1.0	0.7	1.0

KULU

Start time (doy)	318 ± 179	110 ± 36	108 ± 24
End time (doy)	116 ± 204	312 ± 22	334 ± 10
Duration (days)	-179 ± 380	207 ± 36	227 ± 24
Uplift (mm)	5.1 ± 5.1	2.9 ± 1.7	11.9 ± 2.0
Uplift rate (10^{-2} mm day $^{-1}$)	0.0 ± 1.0	1.4 ± 0.3	5.2 ± 0.4
AMSAT (°C)	-0.5	-0.2	1.0
CAPDD (days)	180	183	188
AMSSWT (°C)	5.3	4.9	5.7

LYNS

Start time (doy)	121 ± 8	259 ± 4	210 ± 6
End time (doy)	374 ± 8	401 ± 6	361 ± 4

Duration (days)	254 ± 11	142 ± 5	151 ± 6
Uplift (mm)	4.6 ± 0.8	7.2 ± 0.8	6.9 ± 0.8
Uplift rate (10^{-2} mm day $^{-1}$)	1.8 ± 0.4	5.1 ± 0.4	4.6 ± 0.5
AMSAT (°C)	-9.2	-9.0	-6.8
CAPDD (days)	113	107	116
AMSSWT (°C)	0.3	0.1	0.2

MARG

Start time (doy)	77 ± 10	193 ± 11	172 ± 3
End time (doy)	355 ± 4	369 ± 3	356 ± 2
Duration (days)	278 ± 11	176 ± 11	185 ± 3
Uplift (mm)	11.1 ± 0.7	7.2 ± 0.6	14.7 ± 0.7
Uplift rate (10^{-2} mm day $^{-1}$)	4.0 ± 0.3	4.1 ± 0.4	7.9 ± 0.4
AMSAT (°C)	-1.4	-1.0	0.5
CAPDD (days)	155	155	195
AMSSWT (°C)	5.5	5.2	5.9

PLPK

Start time (doy)	85 ± 9	186 ± 17	172 ± 4
End time (doy)	344 ± 5	352 ± 4	379 ± 10
Duration (days)	258 ± 10	165 ± 16	207 ± 10
Uplift (mm)	9.8 ± 0.8	5.8 ± 0.7	14.2 ± 1.0
Uplift rate (10^{-2} mm day $^{-1}$)	3.8 ± 0.3	3.6 ± 0.4	6.9 ± 0.4
AMSAT (°C)	-3.3	-3.1	-2.6
CAPDD (days)	125	142	146
AMSSWT (°C)	5.0	4.8	5.4

QAQ1

Start time (doy)	165 ± 37	225 ± 23	165 ± 11
------------------	--------------	--------------	--------------

End time (doy)	350 ± 19	384 ± 13	370 ± 8
Duration (days)	185 ± 36	159 ± 21	204 ± 12
Uplift (mm)	3.6 ± 1.6	5.1 ± 1.5	12.4 ± 1.7
Uplift rate (10^{-2} mm day $^{-1}$)	1.9 ± 0.4	3.2 ± 0.4	6.1 ± 0.4
AMSAT (°C)	0.5	1.4	4.6
CAPDD (days)	219	194	272
AMSSWT (°C)	4.6	4.3	4.9

RINK

Start time (doy)	168 ± 12	237 ± 6	184 ± 5
End time (doy)	376 ± 6	380 ± 3	357 ± 4
Duration (days)	208 ± 11	143 ± 6	173 ± 5
Uplift (mm)	6.9 ± 0.8	7.3 ± 0.7	10.0 ± 0.8
Uplift rate (10^{-2} mm day $^{-1}$)	3.3 ± 0.4	5.1 ± 0.4	5.6 ± 0.4
AMSAT (°C)	-4.0	-3.8	-0.6
CAPDD (days)	135	129	184
AMSSWT (°C)	1.7	1.3	1.8

SENU

Start time (doy)	N/D	151 ± 3	152 ± 2
End time (doy)	313 ± 3	322 ± 4	331 ± 2
Duration (days)	N/D	170 ± 4	179 ± 2
Uplift (mm)	N/D	11.5 ± 0.6	19.3 ± 0.7
Uplift rate (10^{-2} mm day $^{-1}$)	N/D	6.7 ± 0.3	10.8 ± 0.4
AMSAT (°C)	0.5	1.4	4.6
CAPDD (days)	219	194	270
AMSSWT (°C)	4.6	4.3	4.9

SRMP

Start time (doy)	150 ± 13	238 ± 5	174 ± 4
End time (doy)	373 ± 5	376 ± 3	350 ± 3
Duration (days)	223 ± 13	139 ± 5	176 ± 4
Uplift (mm)	6.9 ± 0.8	7.7 ± 0.7	11.6 ± 0.8
Uplift rate (10^{-2} mm day $^{-1}$)	3.1 ± 0.4	5.6 ± 0.4	6.6 ± 0.4
AMSAT (°C)	-6.0	-5.5	-3.1
CAPDD (days)	118	114	150
AMSSWT (°C)	1.1	0.8	1.1

THU3

Start time (doy)	76 ± 277	218 ± 37	211 ± 16
End time (doy)	367 ± 29	398 ± 23	350 ± 11
Duration (days)	333 ± 257	184 ± 36	139 ± 16
Uplift (mm)	3.5 ± 3.4	5.6 ± 2.0	5.7 ± 1.9
Uplift rate (10^{-2} mm day $^{-1}$)	1.2 ± 0.3	3.1 ± 0.4	4.1 ± 0.5
AMSAT (°C)	-9.2	-9.0	-6.8
CAPDD (days)	113	107	116
AMSSWT (°C)	0.3	0.1	0.2

TIMM

Start time (doy)	151 ± 7	196 ± 9	181 ± 3
End time (doy)	352 ± 3	374 ± 3	360 ± 3
Duration (days)	200 ± 7	177 ± 8	179 ± 3
Uplift (mm)	10.4 ± 0.7	8.4 ± 0.7	13.7 ± 0.7
Uplift rate (10^{-2} mm day $^{-1}$)	5.2 ± 0.4	4.7 ± 0.4	7.7 ± 0.4
AMSAT (°C)	-1.4	-1.0	0.5
CAPDD (days)	155	155	195
AMSSWT (°C)	5.4	5.1	5.8

TREO

Start time (doy)	122±6	176±6	162±4
End time (doy)	349±3	343±4	367±3
Duration (days)	227±6	167±6	205±4
Uplift (mm)	14.7±0.7	5.4±0.6	17.6±0.8
Uplift rate (10^{-2} mm day $^{-1}$)	6.5±0.4	3.3±0.4	8.6±0.4
AMSAT (°C)	-1.4	-1.0	0.5
CAPDD (days)	155	155	195
AMSSWT (°C)	5.5	5.2	5.9

- Symbols are the same as in Table 3.1.

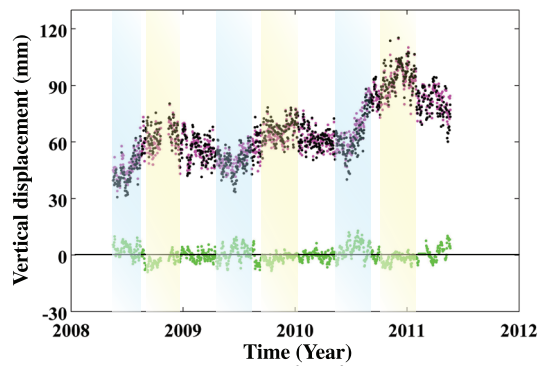


Figure A1: GPS time series from site SENU before (pink) and after (black) atmospheric pressure loading correction. Green dots are vertical displacement due to atmospheric pressure loading. Light blue vertical bands mark approximate time period when atmospheric loading displacement is mainly positive. Light yellow vertical bands mark corresponding negative displacement.

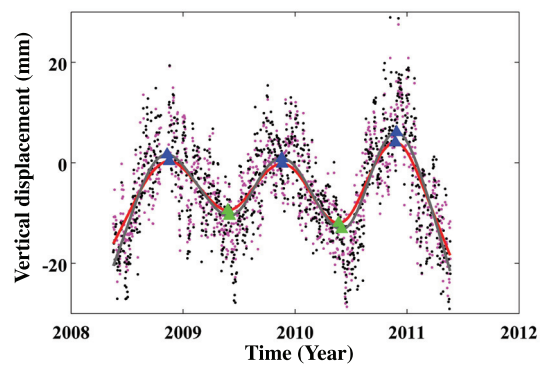


Figure A2: Example GPS time series for site SENU, de-trended and fit with annual model shown in 3.2. Pink and black dots represent daily vertical position estimates before and after atmospheric pressure loading correction respectively. Red and grey curves are respective best-fit cubic splines with smoothing parameter set to 0.91.

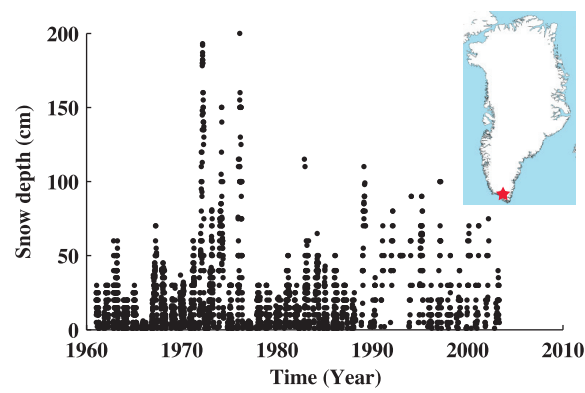


Figure A3: Snow depth recorded at a meteorological station (WMO-ID 04272, Table A2) in southern Greenland coastal area. Red star indicates location of the meteorological station.

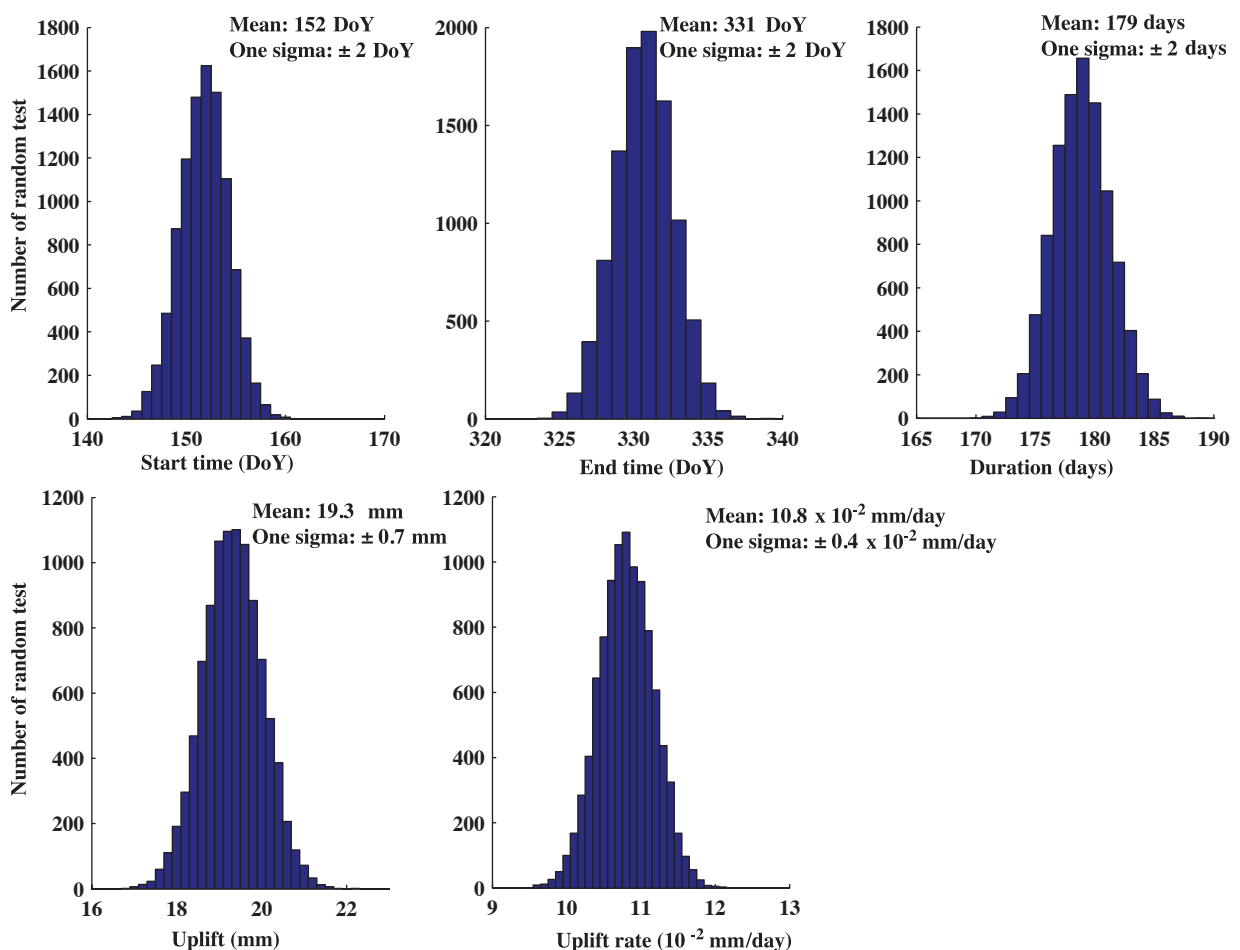
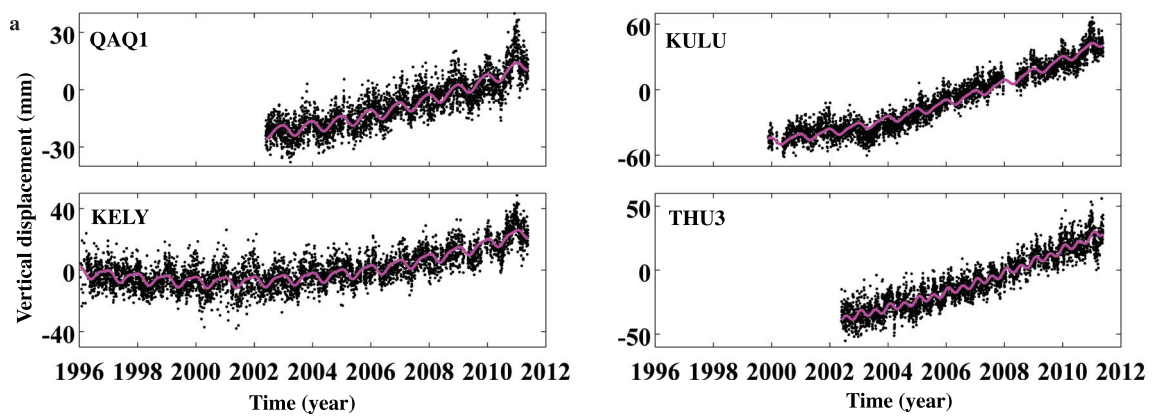


Figure A4: Histogram showing statistical result for five seasonal uplift variables at GPS station SENU. Five variables are normally distributed.



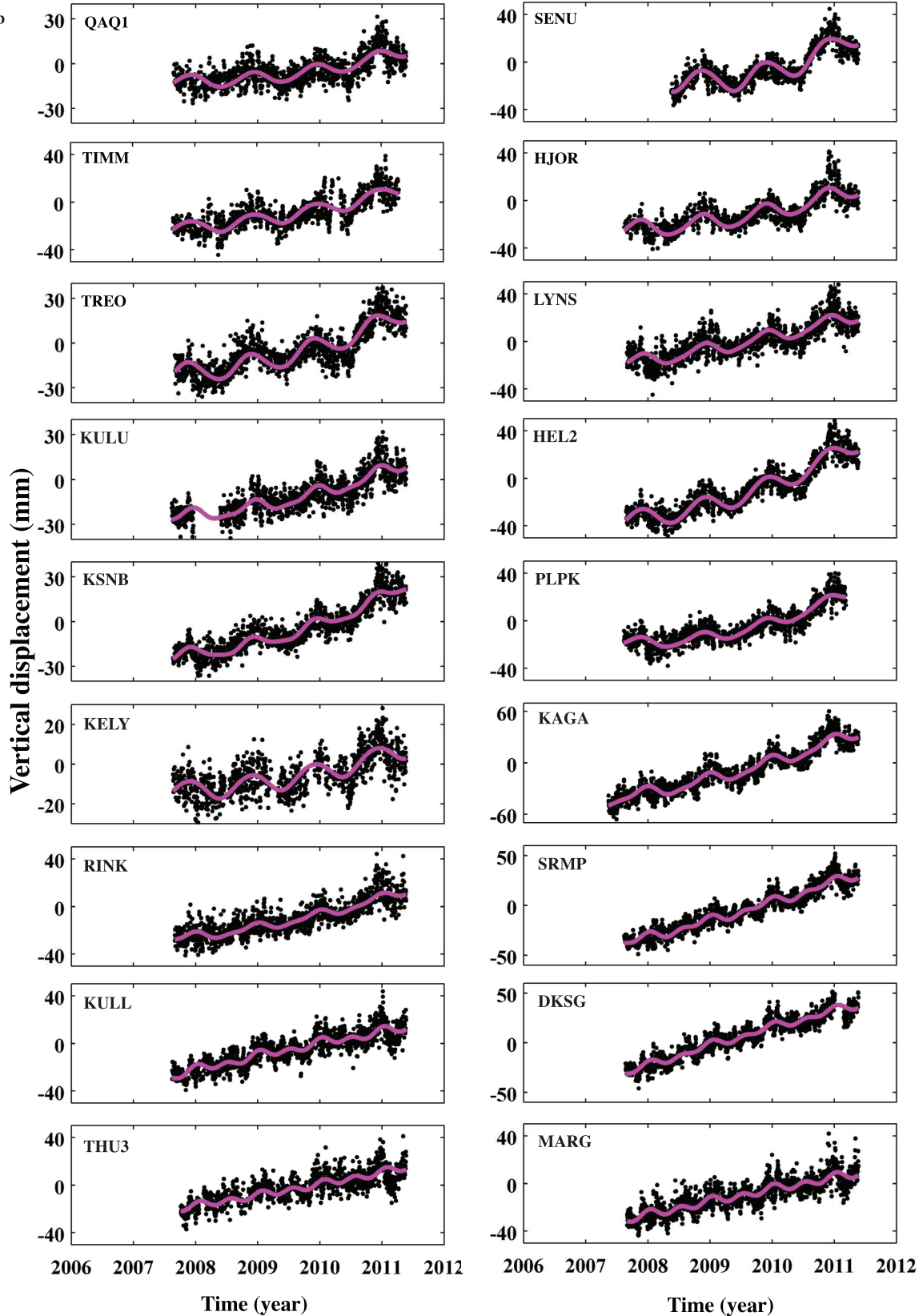
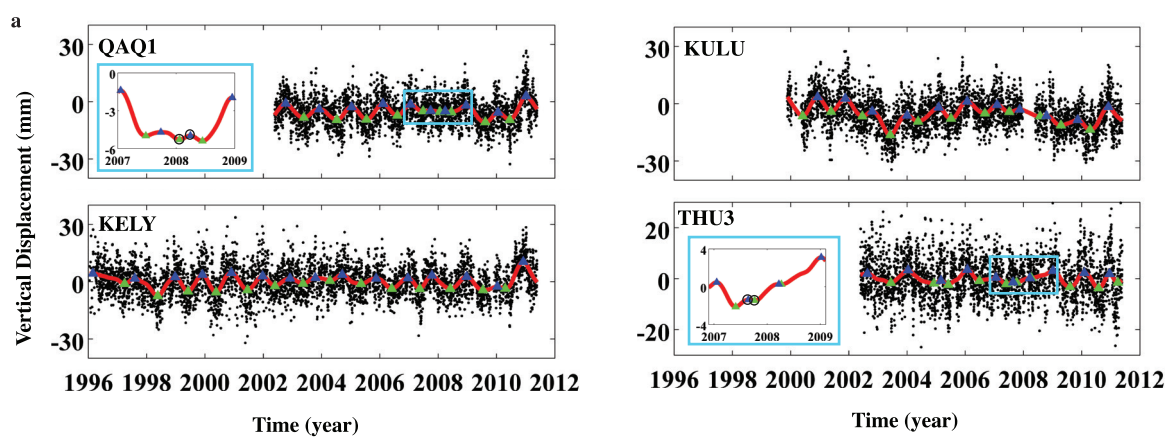


Figure A5: Time series of GPS vertical component position. (a) Time series of long-term GPS records. (b) Time series of short-term GPS records. For comparison with other sites, time series between mid-2007 and early 2011 at sites KULU, QAAQ1, KELY and KULU are also shown in (b). Vertical position is relative to arbitrary position. Pink curve shows constant acceleration model, including annual and semi-annual components. GPS stations are organized from south to north.



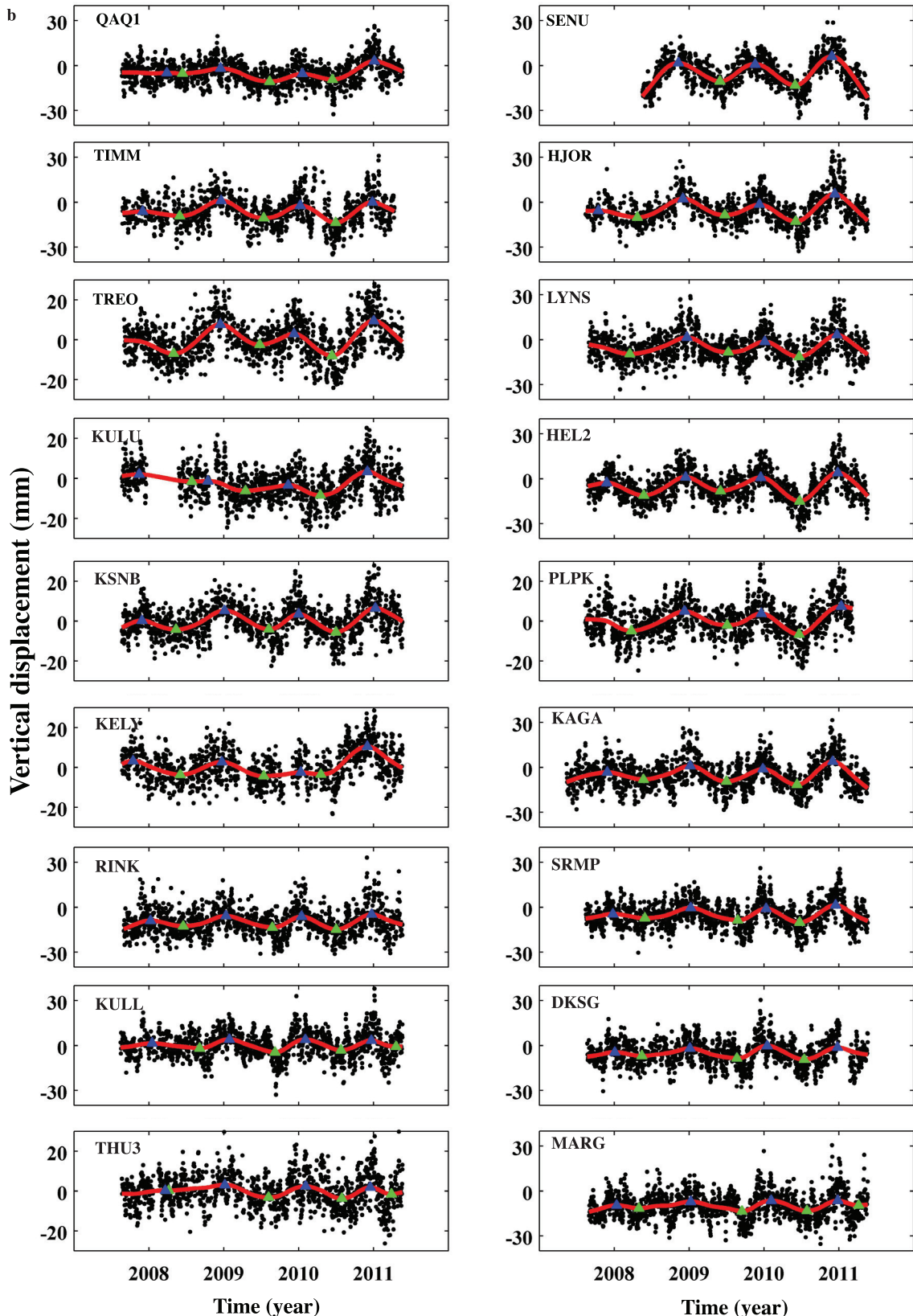


Figure A6: Time series of GPS vertical component position after removing long-term trend by low pass filter. (a) Time series of long-term GPS records. (b) Time series of short-term GPS records. In (b), we zoom in to the last 3 years of four long time series. Red curve is cubic spline best-fit model with 0.91 as smoothing parameter. Blue triangle is the maximum value per year, and green triangle is the minimum value per year.

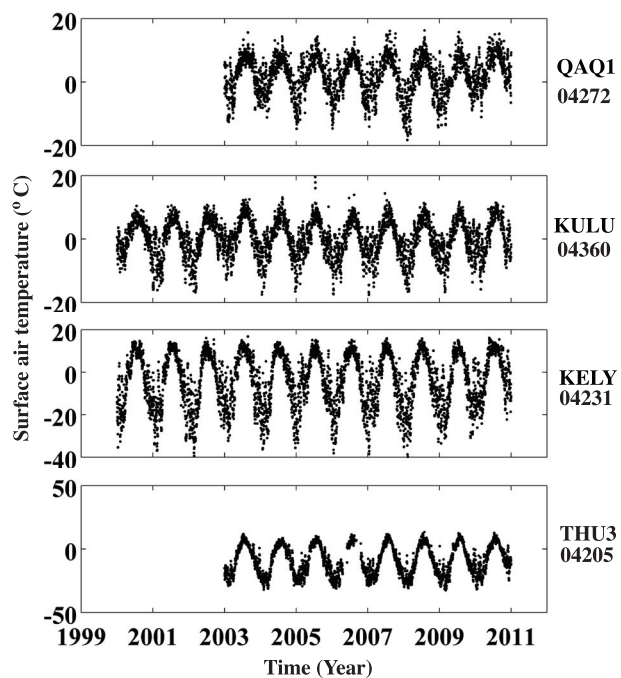


Figure A7: Time series of surface air temperature at meteorological stations near 4 GPS site. Name of nearby GPS site and WMO-ID are on the right side of each plot.

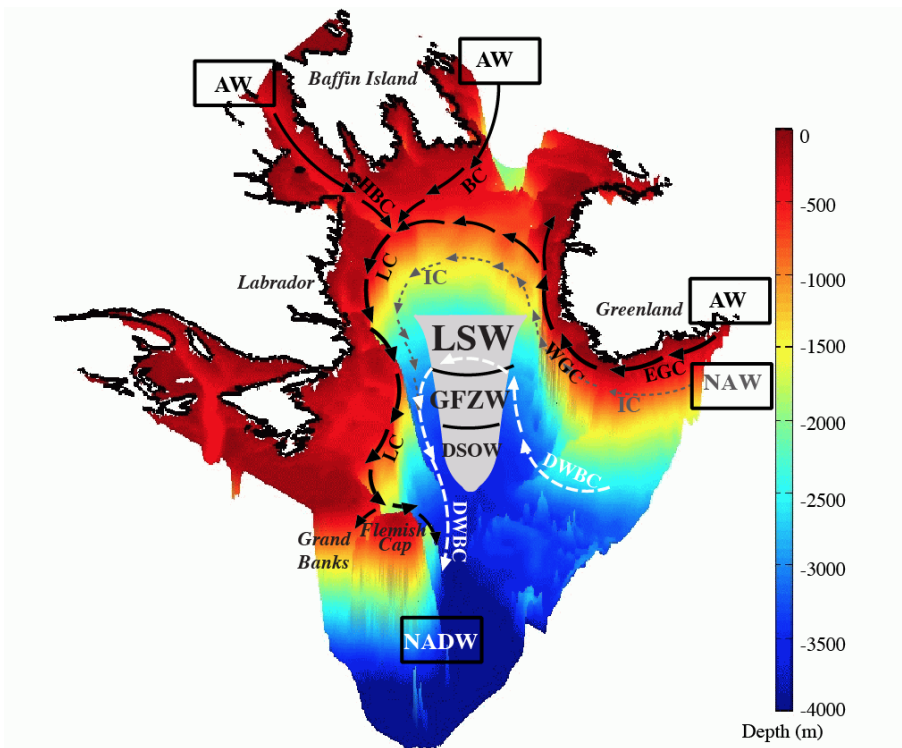


Figure A8: Simplified sketch illustrating 3-D structure of the Labrador Sea and major currents and water masses. Black boxes represent water masses input to and output from the Labrador Sea along specific currents. Arrows represent ocean currents at different depths: black solid arrows represent surface ocean currents carrying cold and fresh Arctic Water; grey dashed arrows represent subsurface ocean current carrying warm and salty North Atlantic Water; white dashed arrows represent the Deep Western Boundary Current that moves North Atlantic Deep Water southward. EGC is East Greenland Current, WGC is West Greenland Current, HBC is Hudson's Bay Current, BC is Baffin Current, LC is Labrador Current, IC is Irminger Current, DWBC is Deep Western Boundary Current. AW is Arctic Water, NAW is North Atlantic Water, LSW is Labrador Sea Water, GFZW is Gibbs Fracture Zone Water, DSOW is Denmark Strait Overflow Water, NADW is North Atlantic Deep Water. Not shown are the geographic sources of Arctic Water, which include the Greenland ice sheet, Arctic Ocean, Canadian Arctic Archipelago, and Hudson Bay, or the types of ice and water masses that contribute, which include glaciers and ice sheets, rivers, sea ice, and precipitation. Also not shown are the major time scales for significant variability, which include annual (summer ice melting, winter cooling and convection) and decadal to multi-decadal (e.g., North Atlantic Oscillation, Atlantic Multi-decadal Oscillation).

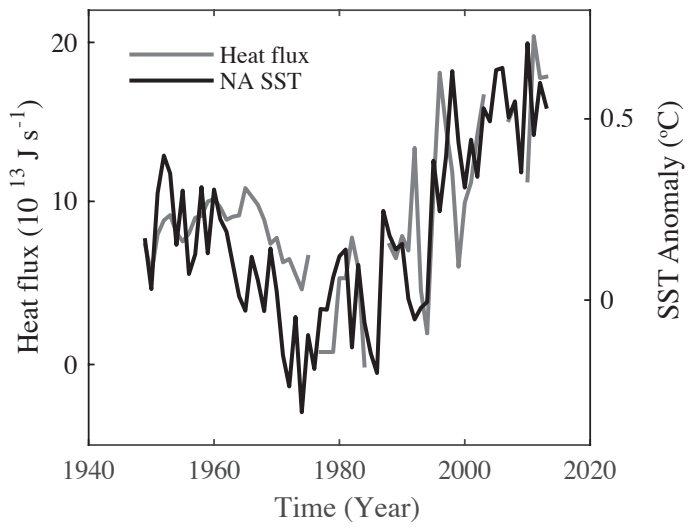


Figure A9: Comparison of Irminger Water heat flux and North Atlantic SST anomaly over the period 1949 – 2013. Grey line indicates Irminger Water heat flux, black line indicates North Atlantic SST anomaly. We use the HADISST dataset to compute SST anomaly. We compute the annual average SST anomaly over a broad area of the North Atlantic, using as boundaries 0° - 60° North latitude and 0° - 80° West longitude, relative to the average temperature for the period 1901 to 1970. Average North Atlantic SST anomaly shows a strong ($R = 0.68$) and significant ($P = 0.001$) correlation with our Irminger heat flux data for the 1949 to 2013 period, with both indices increasing strongly after 1995.

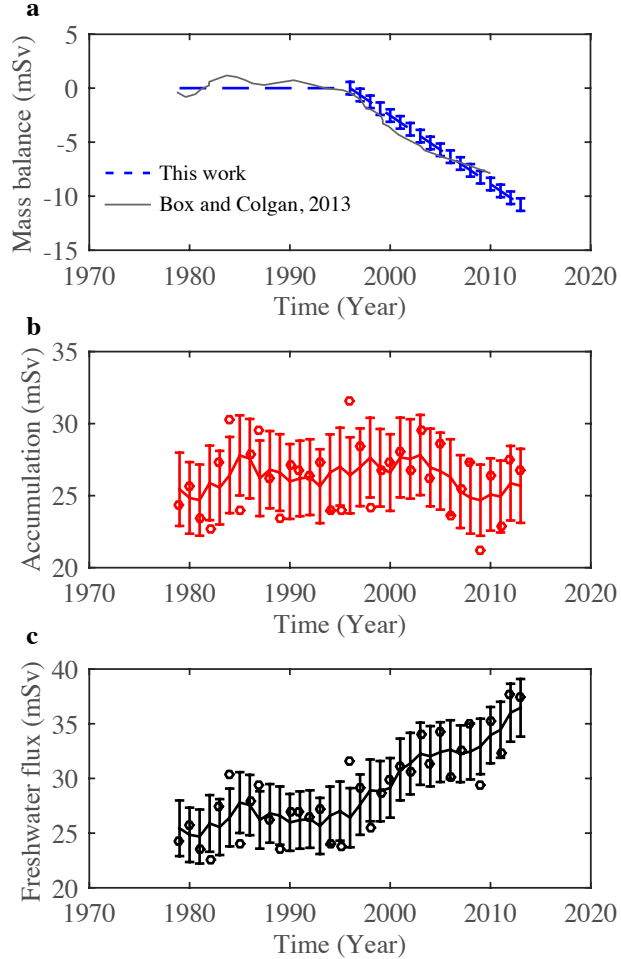


Figure A10: Freshwater flux from Greenland estimated from mass balance and accumulation. (a) Greenland mass balance. Estimate from this study (blue dashed line) is compared with estimate from Box and Colgan (2013). Blue error bars indicate uncertainty of mass balance, estimated at 95% confidence level. (b) Greenland accumulation. Red circles represent annual value. Red solid line represents 5-year running average. Red error bars indicate uncertainty of smoothed accumulation, which is approximated by uncertainty of accumulation modeled by RACMO2.3 ($\pm 9\%$). (c) Freshwater flux from Greenland. Black circles represent freshwater flux from mass balance and annual accumulation (see equation A6). Black solid line represents freshwater flux from mass balance and smoothed accumulation. Black error bars indicate propagated uncertainty.

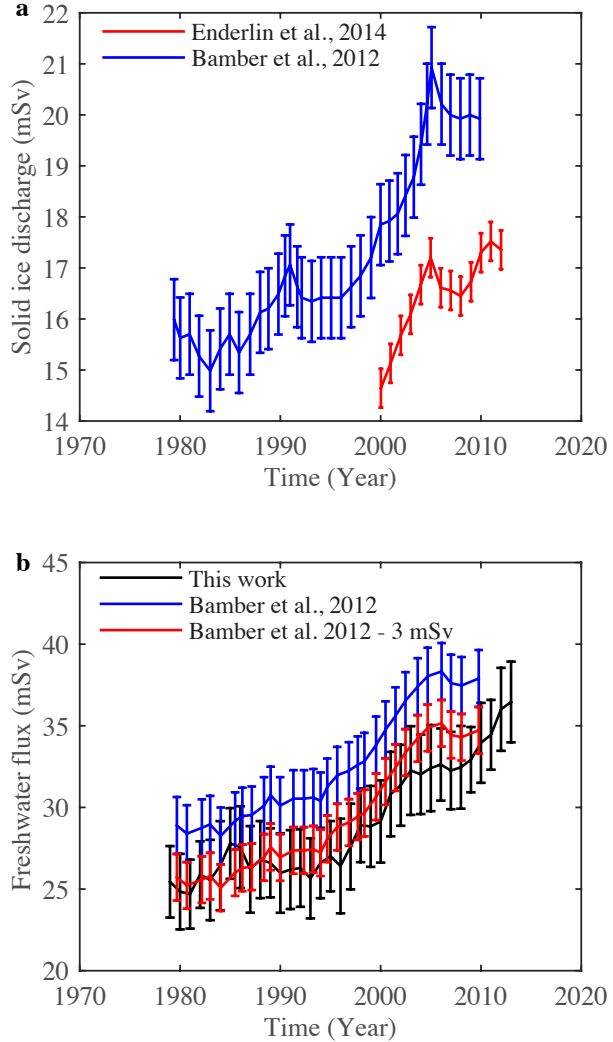


Figure A11: Comparison between estimates of freshwater flux from Greenland. (a) Comparison between two estimates of solid ice discharge from Greenland. Blue line from Bamber et al. (2012), red line from Enderlin et al. (2014). The estimate from Bamber et al. (2012) required extrapolation to cover all Greenland discharge and is ~ 3 mSv ($\sim 100 \text{ km}^3 \text{ yr}^{-1}$) larger than the more recent estimate from Enderlin et al. (2014). (b) Comparison of three estimates of freshwater flux from Greenland: black line (this study), blue line (Bamber et al. (2012)), red line (Bamber et al. (2012)) with correction following Enderlin et al. (2014).

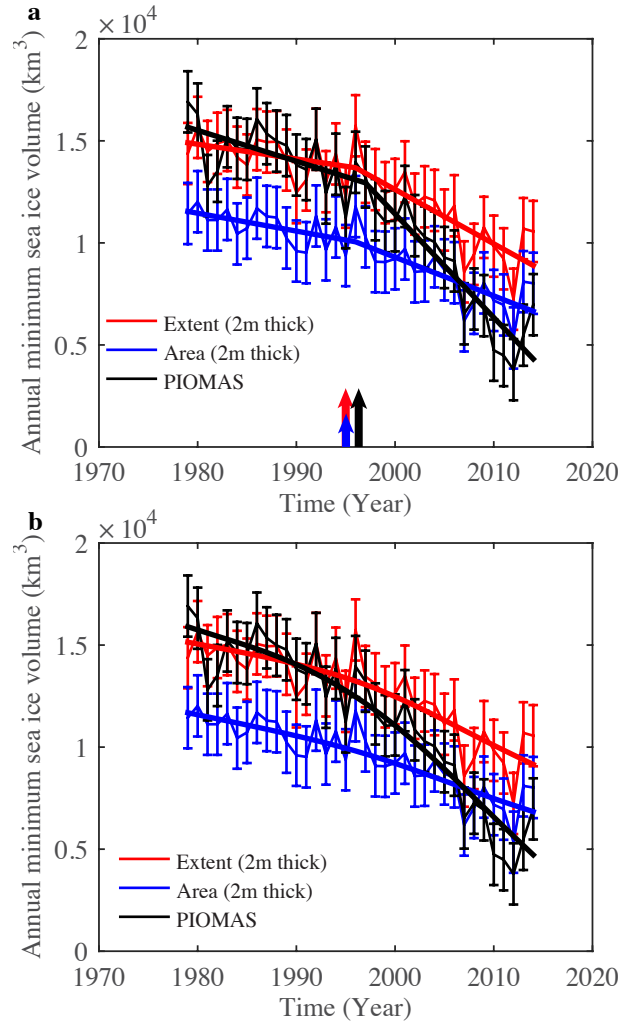


Figure A12: Three estimates of the annual minimum Arctic sea ice volume time series. Red line represents estimate based on ice extent assuming 2 m thickness. Blue line represents estimate based on ice area assuming 2 m thickness. Black line represents volume modeled by the Pan-Arctic Ice Ocean Modeling and Assimilation System (PIOMAS)(Zhang and Rothrock, 2003). Error bars represent the uncertainty of annual minimum Arctic sea ice volume (1500 km^3). (a) Three time series described above are fit with a two-slope model (thick solid line) (Supplementary methods). Arrow marks the onset time of accelerated melting derived from three data sets: 1996 for ice extent and ice area data sets, 1997 for PIOMAS data set. (b) Three time series are fit with the linear state space model (thick solid line) (see methods in Appendix A).

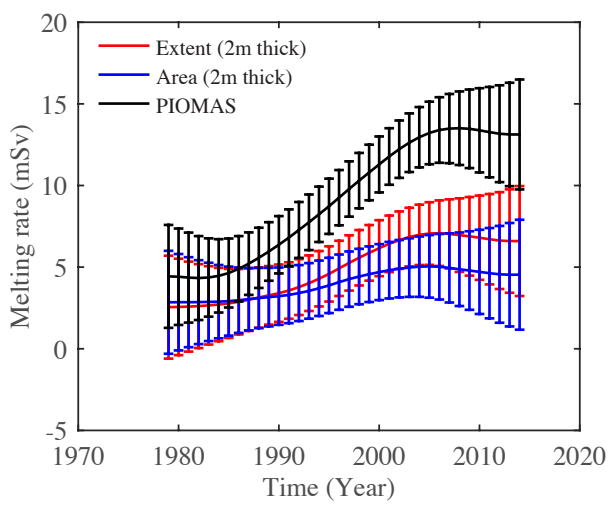


Figure A13: Long term melting rate of Arctic sea ice from three data sets. Red line represents estimate based on ice extent data set. Blue line represents estimate based on ice area data set. Black line represents estimate from the Pan-Arctic Ice Ocean Modeling and Assimilation System (PIOMAS) data set. The melting rate is estimated using the linear state space model (Figure A12b). Error bars indicate uncertainty at 95% confidence level.

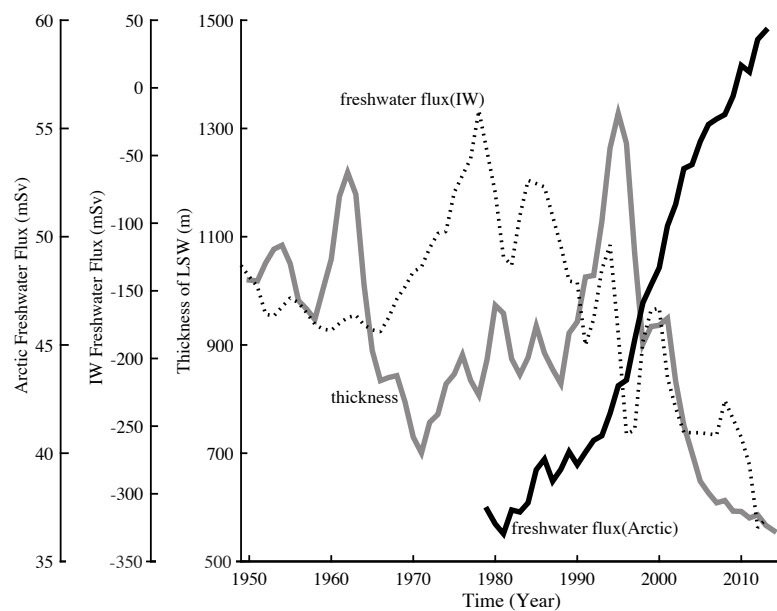


Figure A14: Similar to Figure 4.5 except salt flux of Irminger Water is expressed in terms of freshwater flux. Grey solid line represents thickness of Labrador Sea Water. Black solid line represents Arctic freshwater flux (the sum of freshwater flux from Greenland, the Canadian Arctic Archipelago and Arctic sea ice). Dotted line represents freshwater flux of Irminger Water (IW). Salt flux is converted to freshwater flux using 34.80 as a reference salinity.

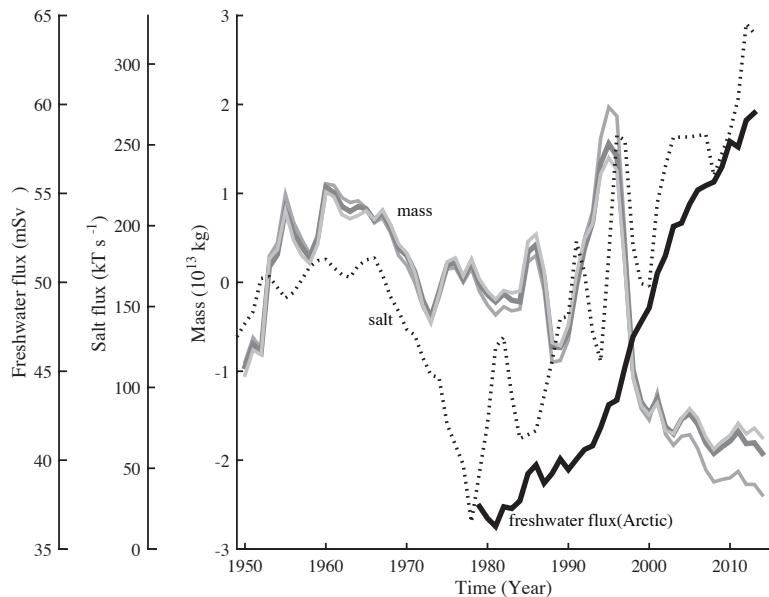


Figure A15: Similar to Figure 4.5 except grey solid line represents the mass of Labrador Sea Water. Black solid line represents Arctic freshwater flux (the sum of freshwater flux from Greenland, the Canadian Arctic Archipelago and Arctic sea ice). Density of Labrador Sea Water is obtained from the objective analyses of EN4.0.2 dataset from the UK Met Office Hadley Center(Good et al., 2013). Mass values are calculated by integrating density with volume between 50° N – 65° N, 38° W – 65° W and three depth range (900 – 2400 m, 1000 - 2500 m and 1100 – 2600 m), relative to the mean of 1950 – 2006.

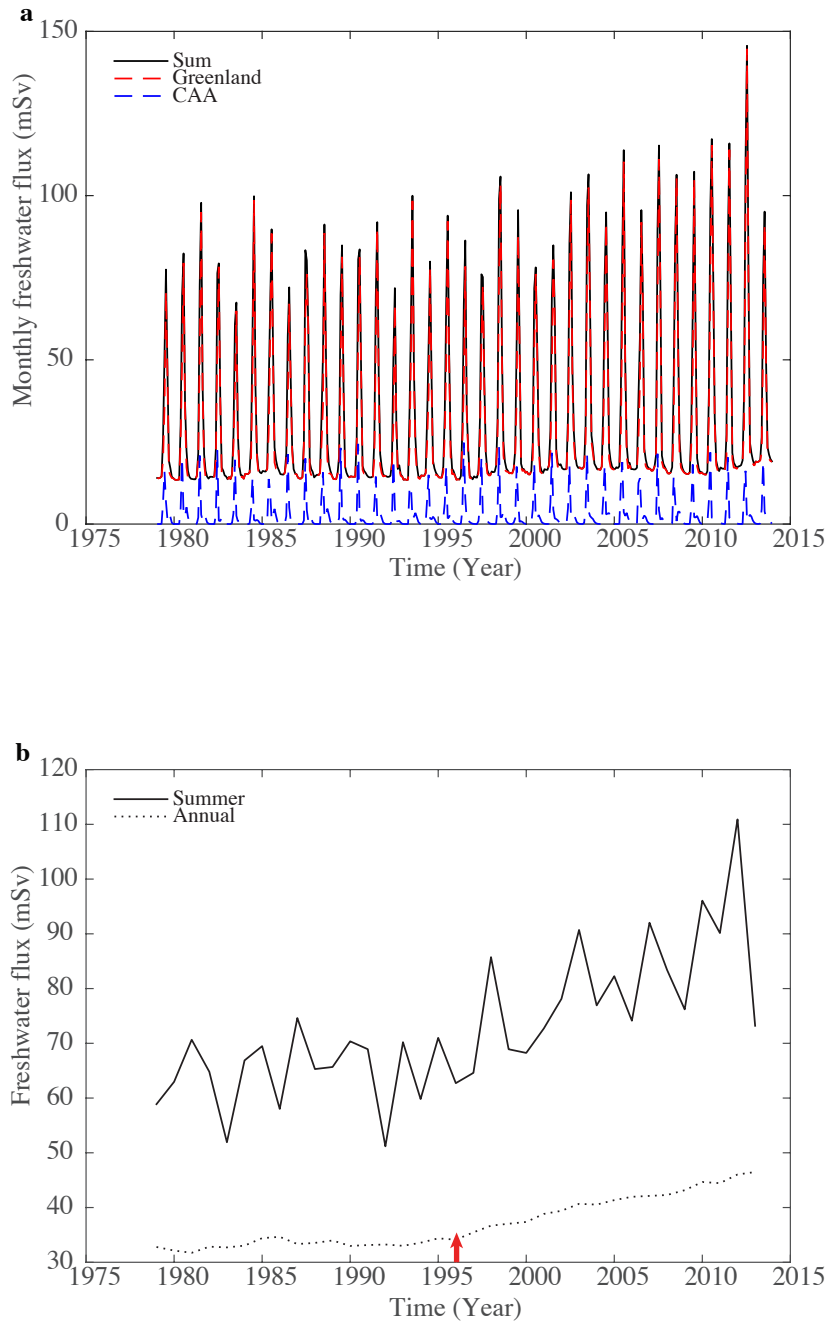


Figure A16: Seasonal variation of freshwater flux from Greenland and the Canadian Arctic Archipelago. (a) Monthly freshwater flux from Greenland (GL), Canadian Arctic Archipelago (CAA) and their total for 1979 – 2013. Freshwater flux from Greenland and CAA peaks in July. Freshwater flux since 2002 has exceeded 100 mSv for about a month a year 9 times, with 2012 having the highest value (150 mSv). (b) Total summer (June, July and August) freshwater flux (solid line) compared to long-term averaged annual freshwater flux (dashed line). Note that summer freshwater flux increased significantly about the time when GRACE data and a simple model of constant acceleration suggest that the current phase of accelerated Greenland mass loss began (red arrow) (see Figure 4.2).

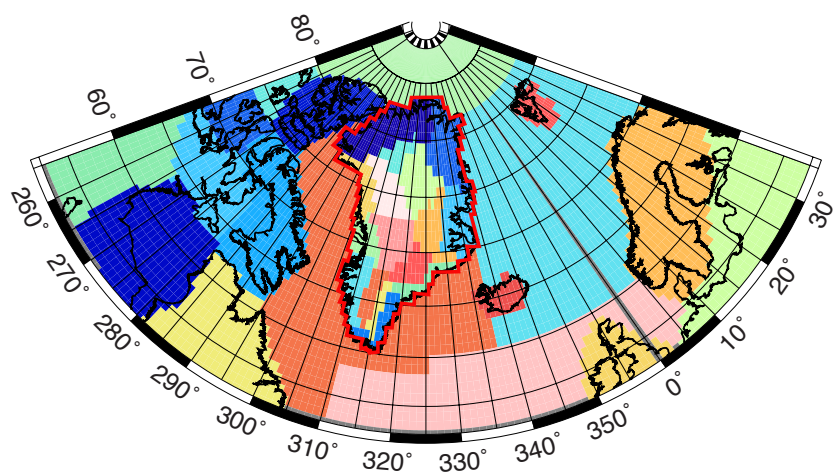


Figure A17: Predefined regions used in this paper to localize the GRACE mass change signal. Greenland is outlined with solid red line.

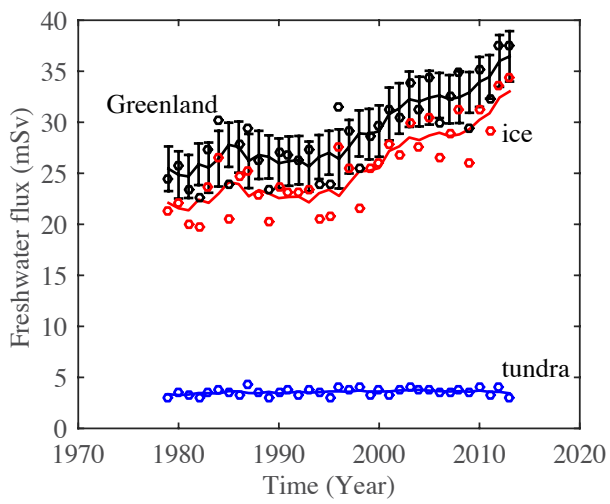


Figure A18: Freshwater flux from Greenland and its two components. Black circles and solid line represent freshwater flux from Greenland. Red circles and solid line represent freshwater flux component from ice mass loss. Blue circles and solid line represent freshwater flux component from tundra runoff. Circles represent annual value and solid line represents 5-year running average. Black error bars indicate propagated uncertainty (Figure A10).

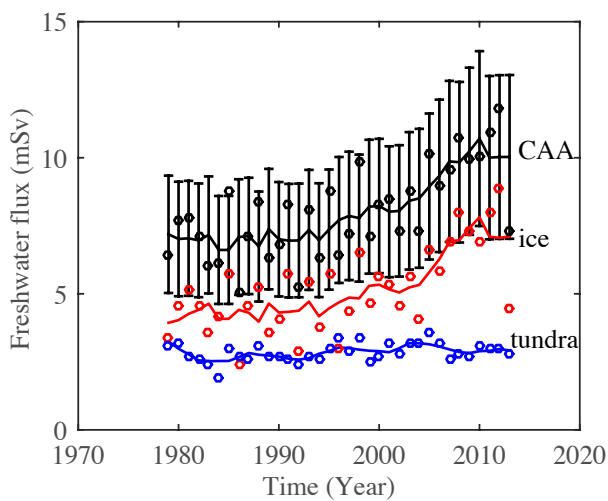


Figure A19: Freshwater flux from the Canadian Arctic Archipelago and its two components. Black circles and solid line represent freshwater flux from the Canadian Arctic Archipelago (CAA). Red circles and solid line represent freshwater flux component from ice mass loss. Blue circles and solid line represent freshwater flux component from tundra runoff. Circle represents annual value and solid line represents 5-year running average. Black error bars indicate uncertainty of smoothed freshwater flux from CAA, approximated by uncertainty of runoff modeled by RACMO2.3, believed to be accurate to $\pm 30\%$ (Lenaerts et al., 2013).